

**INTERFACE ENGINEERING IN ZEOLITE-POLYMER AND  
METAL-POLYMER HYBRID MATERIALS**

A thesis  
Presented to  
The Academic Faculty

by

Jung-Hyun Lee

In Partial Fulfillment  
of the Requirements for the Degree  
Doctor of Philosophy in the  
School of Chemical and Biomolecular Engineering

Georgia Institute of Technology  
December 2010

**COPYRIGHT 2010 BY JUNG-HYUN LEE**

# **INTERFACE ENGINEERING IN ZEOLITE-POLYMER AND METAL-POLYMER HYBRID MATERIALS**

Approved by:

Dr. J. Carson Meredith, Advisor  
School of Chemical & Biomolecular  
Engineering  
*Georgia Institute of Technology*

Dr. William J. Koros  
School of Chemical & Biomolecular  
Engineering  
*Georgia Institute of Technology*

Dr. Dennis W. Hess  
School of Chemical & Biomolecular  
Engineering  
*Georgia Institute of Technology*

Dr. Ronald R. Chance  
School of Chemical & Biomolecular  
Engineering  
*Georgia Institute of Technology*

Dr. Yulin Deng  
School of Chemical & Biomolecular  
Engineering  
*Georgia Institute of Technology*

Dr. Valerie B. Sitterle  
Information Technology &  
Telecommunications Laboratory  
*Georgia Tech Research Institute*

Date Approved: [Month dd, yyyy]

To my wife and family

## **ACKNOWLEDGEMENTS**

There are so many people who have shaped my life to this point. I would like to thank Dr. Carson Meredith for all his support and encouragement to help me reach this stage. His enthusiasm, persistent work ethic and positive spirit kept me motivated to keep striving forward toward completing of the degree. I acquired lots of knowledge as well as interpersonal relationships from him with his being a model that I strive to emulate.

I am grateful to my committee members, Dr. William Koros, Dr. Dennis Hess, Dr. Ronald Chance, Dr. Yulin Deng and Dr. Valerie Sitterle for providing thoughtful input and helping to mold my ideas. Special appreciation is extended to my collaborators, Dr. Sankar Nair, Dr. Christopher Jones, Dr. Victor Breedveld, Dr. Jeffrey Sitterle and Dr. Mahmoud Mahmoud for providing helpful ideas. I also thank the Exxonmobil company for providing financial support.

I would like to thank the members of the Meredith research group for all the friendships, discussion, and guidance. It has been a great pleasure to work with all personalities in the Meredith group. I would like to especially thank Dr. Pedro Zapata, Dr. Beng Joo Thio and Dr. Keith Reed. I am truly blessed to have so many intelligent and motivated people as my colleagues.

I thank to all ChBE Korean Association members at Georgia Tech for enjoyable gatherings and a warm friendship that we shared. We have partaken in joys and sorrows with each other, and I am truly lucky to have such dependable friends.

Above all, I cannot say enough for the role my family has played in helping me in my endeavors. I am extremely thankful to my lovely wife, Eunjung Lee, for her unconditional support and love needed for me to endure and overcome all challenges during my PhD. My parents, Eunsung Lee and Jinwoul Choi, have always kept me grounded, have prayed steadily for me, and have established themselves as role models. I would also like to thank my father and mother-in-law, Eunwha Lee and Soonjung Choi. I could never have achieved this without their encouragement and trust. My brothers and sisters, Donghyun Lee, Yunjin Choi, Sinmyung Lee and Jiyoung Lee are thanked for their consistent concerns.

Finally, I would like to thank the almighty God for guiding me to complete the degree successfully.

# TABLE OF CONTENTS

	Page
ACKNOWLEDGEMENTS.....	iv
LIST OF TABLES.....	x
LIST OF FIGURES.....	xi
SUMMARY.....	xvii
 <u>CHAPTER</u>	
1 INTRODUCTION.....	1
1.1. The Role of Interfaces in Designing Hybrid Materials.....	1
1.2. Zeolite-Polymer Interfaces in Mixed-Matrix Membranes.....	2
1.3. Thesis Overviews.....	2
1.4. References.....	3
2 BACKGROUND.....	6
2.1. Mixed-Matrix Membranes.....	6
2.1.1. Issues in Mixed-Matrix Membranes.....	7
2.1.2. Materials.....	10
2.2. Interface Characterization Technique.....	14
2.2.1. Colloidal Probe Atomic Force Microscopy (AFM) Technique.....	14
2.2.2. Characterization of Polymer Composite Properties.....	15
2.3. Research Objectives.....	16
2.4. References.....	19
3 ZEOLITE-POLYMER INTERFACIAL ADHESION MEASUREMENT....	25
3.1. Overview.....	25
3.2. Theory.....	26

3.3. Experimental.....	27
3.3.1. Materials and Procedure.....	27
3.3.2. Experimental Methods.....	32
3.4. Results and Discussion.....	35
3.4.1. Analysis of Polymer Surface Energy.....	35
3.4.2. MFI Zeolite-Polymer Adhesion Measurement in Air.....	37
3.5. Conclusions.....	44
3.6. References.....	45
4 MEASUREMENT OF INTERPARTICLE FORCES IN NMP-WATER MIXTURES: SILICA-SILICA SYMMETRIC SYSTEM.....	49
4.1. Overview.....	49
4.2. Theoretical Background.....	50
4.3. Experimental.....	53
4.3.1. Materials and Procedure.....	53
4.3.2. Experimental Methods.....	54
4.4. Results and Discussion.....	57
4.4.1. Silica-Silica versus Silica-Polymer Adhesion.....	57
4.4.2. Silica-Silica Interactions in NMP-Water Binary Mixtures...	58
4.5. Conclusions.....	74
4.6. References.....	75
5 MEASUREMENT OF INTERPARTICLE FORCES IN NMP-WATER MIXTURES: SILICA-SILANATED SILICA ASYMMETRIC SYSTEM....	80
5.1. Overview.....	80
5.2. Theoretical Background.....	81
5.3. Experimental.....	82
5.3.1. Materials and Procedure.....	82

5.3.2. Experimental Methods.....	82
5.4. Results and Discussion.....	83
5.4.1. Hydrophilic Silica-Hydrophobic Silica Interactions in Water.....	83
5.4.2. Hydrophilic Silica-Hydrophobic Silica Interactions in NMP-Water Binary Mixtures.....	89
5.5. Conclusions.....	97
5.6. References.....	98
6 CHARACTERIZATION OF ZEOLITE (MFI)/POLYMER COMPOSITE PROPERTIES.....	101
6.1. Overview.....	101
6.2. Experimental.....	102
6.2.1. Materials and Procedure.....	102
6.2.2. Experimental Methods.....	105
6.3. Results and Discussion.....	106
6.3.1. Particle Modification.....	106
6.3.2. MFI/Polymer Composites.....	108
6.4. Conclusions.....	128
6.5. References.....	129
7 CONCLUSIONS AND RECOMMENDATIONS.....	133
7.1. Summary and Conclusions.....	133
7.2. Recommendations for Future Work.....	135
7.2.1. Correlate AFM Interaction Results to the Final Membrane Morphology.....	135
7.2.2. Define Adhesion of Zeolite to Polymers.....	136
7.2.3. Relate Composite Properties to Membrane Permselectivity and Evaluate Usefulness in Predicting Membrane Performance.....	137



7.3. References.....	137
APPENDIX A: METAL-POLYMER INTERFACES IN METAL-COATED POLYMER COMPOSITE MICROSPHERES.....	138
A.1. Introduction.....	138
A.2. Overview.....	140
A.3. Experimental.....	141
A.3.1. Materials and Synthesis.....	141
A.3.2. Experimental Methods.....	143
A.4. Results and Discussion.....	143
A.4.1. CSH Mechanism.....	143
A.4.2. Optical Properties of Metal-Coated Polymer Beads.....	151
A.5. Conclusions.....	159
A.6. References.....	160

## LIST OF TABLES

	Page
Table 3.1: The values of spring constant and contact area of zeolite colloidal probes.....	32
Table 3.2: Surface tension components ( $\text{mJ/m}^2$ ) of testing liquids.....	35
Table 3.3: Contact angle ( $^\circ$ ) of polymer surfaces with testing liquids.....	35
Table 3.4: Surface tension components ( $\text{mJ/m}^2$ ) of polymer film surfaces.....	36
Table 3.5: AFM adhesion force ( $F_{ad}$ ) between a bare MFI zeolite and polymer surfaces.....	37
Table 3.6: Fitting parameters (coefficients and correlation coefficient).....	39
Table 4.1: Permittivity ( $\epsilon$ ), refractive index ( $n$ ), dynamic viscosity ( $\eta$ ) and surface tension ( $\gamma$ ) of a NMP-water mixture as a function of NMP concentration (vol.%)..	60
Table 4.2: The fitting parameters ( $t$ and $\gamma$ ) estimated from the force curves at 10 – 70 vol.% NMP.....	72
Table 5.1: Surface roughness ( $Ra$ and $Rms$ ) and water contact angles ( $\theta$ ) of OTS-coated glass surfaces silanated with various immersion times ( $t$ ), and jump distances ( $D_j$ ) of a hydrophilic silica probe onto the OTS-coated surfaces in DI water.....	88
Table 6.1: Thermal properties (the width of the glass transition, $\Delta T$ , and $T_g$ ) of pure PVAc and PVAc composites containing 10 vol.% of UN-, GT- and ST-nMFIs or $\mu$ MFIs as a function of the annealing temperature (20, 40, and 100 $^\circ\text{C}$ for 24 h, respectively).....	122

## LIST OF FIGURES

	Page
Figure 1.1: The role of interfaces in the field of materials engineering.....	1
Figure 1.2: Scheme of mixed-matrix membrane design.....	2
Figure 2.1: Upper-bound trade-off curve in transport properties for oxygen/nitrogen gas pair [12]. (□: Typical molecular sieves and ♦: Rubbery and glassy polymers).....	6
Figure 2.2: Sieve in a cage morphology and schematic gas flow through interfacial voids around the zeolite surface in zeolite-polymer mixed matrix membranes....	7
Figure 2.3: Asymmetric hollow fiber membrane.....	8
Figure 2.4: Schematic of hollow fiber spinning set-up.....	9
Figure 2.5: Ternary phase diagram of polymer, solvent and non-solvent.....	10
Figure 2.6: Chemical structures of polymer materials.....	11
Figure 2.7: Schematic of the pore structure of pure-silica MFI.....	12
Figure 2.8: SEM images of untreated and surface-treated MFI microparticlels (~ 5 μm); (a) untreated, (b) Grignard-treated and (c) Solvothermally-treated.....	13
Figure 2.9: Schematics of AFM force measurement and a typical force-distance curve.....	14
Figure 2.10: Schematics of HTMECH and a typical strain-stress curve (A: ultimate tensile strength, slope of B: initial tensile modulus and C: elongation at break).....	16
Figure 2.11: Schematics of the overall research goal.....	17
Figure 2.12: Relationship of properties, interface and performance.....	19
Figure 3.1: Schematic of zeolite colloidal probe fabrication.....	30
Figure 3.2: (Top) SEM image of a pure-silica MFI zeolite colloidal probe (top), (middle) AFM phase image of the (010) surface of zeolite microcrystal (2.5 x 2.5 μm <sup>2</sup> ), and (bottom) cross-sectional height profile.....	31
Figure 3.3: Typical force-displacement curves between the zeolite colloidal probe or bare probe and PVAc polymer surface.....	33

Figure 3.4: Fitting of a planar model of equation 3.5 to force data. Circles are above the plane, squares are below the plane and lines from data points to the plane indicate fitting errors.....	38
Figure 3.5: Carbonyl fraction of polymers versus the Lewis basicity contribution to the polymer-zeolite adhesion, $(\gamma_P^-)^{1/2}$ .....	40
Figure 3.6: Adhesion force between a bare zeolite and polymer surfaces, PVAc (●) and PS (◇), as a function of relative humidity.....	42
Figure 3.7: Adhesion force between a MFI zeolite and polymer surfaces as a function of zeolite surface chemistry.....	44
Figure 4.1: Simulated structure of surface macrocluster layer (left) and density profile of ethanol (right) on the silica surface in ethanol-cyclohexane mixture: (a) highly-ordered ethanol layer (~ 3 nm) and (b) aggregate of anisotropy ethanol cluster (~ 30 nm).....	51
Figure 4.2: Schematic of bridging mechanism of the macrocluster surface adsorption layers.....	52
Figure 4.3: SEM image of a silica colloidal probe.....	54
Figure 4.4: Raw approach force ( $F$ )-displacement curves between two silica surfaces in pure water and NMP, respectively.....	56
Figure 4.5: Silica-silica versus silica-polymer adhesion as a function of medium conditions.....	58
Figure 4.6: Force ( $F/R$ ) - separation ( $D$ ) curves between a hydrophilic silica sphere and a hydrophilic glass plate during approach and retraction in a pure liquid: (a) in DI water (The data points represent the experimental surface force and the solid line indicates the best fit to DLVO theory at constant surface potential. The fitting parameters are: Nonretarded Hamaker constant ( $H_A$ ) = $6.5 \times 10^{-21}$ J, Debye length ( $\kappa^{-1}$ ) = 35 nm and surface potential ( $\psi_0$ ) = - 76 mV) and (b) in NMP.....	59
Figure 4.7: Nonretarded Hamaker constant ( $H_A$ ) as a function of NMP concentration (vol.%) for silica and glass surfaces across a NMP-water mixture calculated from the Lifshitz theory using the medium properties given in Table 4.1 and the experimental zeta potential value ( $\zeta$ ) of the silica particle suspension in a NMP-water mixture obtained from the electrophoretic mobility measurements.....	62

Figure 4.8: (a) Force ( $F/R$ ) - separation ( $D$ ) curves between a hydrophilic silica sphere and a hydrophilic glass plate during approach in NMP-water mixtures at various NMP concentrations (vol.%). (The dashed line indicated by the arrow represents the van der Waals attraction calculated by using a nonretarded Hamaker constant of $6.5 \times 10^{-21}$ J for the silica/water/glass.) (b) Force profiles between the surfaces during approach in NMP-water mixtures at NMP concentrations of 10, 30, 50, and 70 vol.%. (data points represent the experimental surface force and solid line are curves fitted to equation 4.1.).....	63
Figure 4.9: Pull-off force ( $F_{off}/R$ ) and the range of attraction between a hydrophilic silica sphere and a hydrophilic glass plate in a NMP-water mixture at various NMP concentrations (vol.%)......	65
Figure 4.10: The contact angle ( $\theta$ ) on the hydrophilic glass plate and liquid-vapor surface tension ( $\gamma_L$ ) of a NMP-water mixture solution at various NMP concentrations (vol.%)......	67
Figure 4.11: Competitive hydrogen bonding of liquid components (NMP and water) on the silica surface (left) and hypothesized liquid structures near the silica surface.....	68
Figure 4.12: Correlation of the contact angle ( $\theta$ ) to (a) the pull-off force ( $F_{off}/R$ ) and (b) the range of attraction.....	74
Figure 5.1: (a) Force ( $F/R$ ) - separation ( $D$ ) curves between a hydrophilic silica sphere and OTS-coated glass plates having different contact angles ( $\theta = 5, 106, 111$ and $113^\circ$ ) during approach in DI water (The solid line in the inset represents the van der Waals attraction calculated by using a nonretarded Hamaker constant of $7.1 \times 10^{-21}$ J for the silica/water/OTS-coated glass). (b) Force-separation curves between a hydrophilic glass sphere and an OTS-coated glass plate ( $\theta = 113^\circ$ ) during approach and retraction in DI water. (The arrow indicates a jump at a large separation during retraction).....	83
Figure 5.2: AFM topographic images ( $5.0 \times 5.0 \mu\text{m}^2$ ) of OTS-coated glass plates silanated with various immersion times: (a) 5 min ( $\theta = 106^\circ$ ), (b) 10 min ( $\theta = 111^\circ$ ) and (c) 60 min ( $\theta = 113^\circ$ )......	87
Figure 5.3: Force ( $F/R$ ) - separation ( $D$ ) curves for a hydrophilic silica sphere and an OTS-coated glass plate (water contact angle = $113^\circ$ ) during approach in NMP-water mixtures at various NMP concentrations (vol.%)......	89
Figure 5.4: Force ( $F/R$ ) - separation ( $D$ ) curves for a hydrophilic silica sphere and an OTS-coated glass plate (water contact angle = $113^\circ$ ) during retraction in NMP-water mixtures at various NMP concentrations (vol.%). (The arrow in the inset indicates a jump at a large separation during retraction).....	90

- Figure 5.5: Pull-off force ( $F_{off}/R$ ) and the range of attraction between a hydrophilic silica sphere and an OTS-coated glass plate (water contact angle =  $113^\circ$ ) in a NMP-water mixture at various NMP concentrations (vol.%). 91
- Figure 5.6: The contact angle ( $\theta$ ) on an OTS-coated hydrophobic glass plate and liquid-vapor surface tension ( $\gamma_L$ ) of a NMP-water mixture solution at various NMP concentrations (vol.%). 92
- Figure 5.7: Correlation of the contact angle ( $\theta$ ) on the OTS-coated hydrophobic glass plate of a NMP-water mixture solution to (a) the pull-off force ( $F_{off}/R$ ) (The predicted van der Waals force ( $F_{VW}/R$ ) was calculated by using equation 5.2. Nonretarded Hamaker constants were calculated from the Lifshitz theory using the medium properties given in Chapter 4. The presence of the thin OTS layer was considered to increase the van der Waals force by about 10 %). (b) the range of attraction between a hydrophilic silica sphere and an OTS-coated glass plate in a NMP-water mixture at various NMP concentrations, respectively. 94
- Figure 6.1: SEM images of untreated and surface-treated MFI nanoparticles (nMFI); (a) untreated (UN), (b) Grignard-treated (GT, 15 wt%  $Mg(OH)_2$ ), and (c) Solvothermally-treated (ST, 20 wt%  $Mg(OH)_2$ ). 106
- Figure 6.2: SEM images of untreated and surface-treated MFI microparticlels ( $\mu$ MFI); (a) untreated (UN), (b) Grignard-treated (GT, 5 wt%  $Mg(OH)_2$ ), (c) Solvothermally-treated (ST, 5 wt%  $Mg(OH)_2$ ), (d) Solvothermally-treated (HST, 20 wt%  $Mg(OH)_2$ ). Scale bars in inset figures indicate 200 nm. 107
- Figure 6.3: SEM images of Ultem composites containing 10 vol.% of untreated (UN) and Grignard-treated (GT) nMFI, which are annealed at 150 and 230  $^\circ C$  for 24 h, respectively: UN-nMFI (a) 150  $^\circ C$  and (b) 230  $^\circ C$  and GT-nMFI (c) 150  $^\circ C$  and (d) 230  $^\circ C$ . 109
- Figure 6.4: Mechanical properties (a) tensile strength and b) elongation at break of Ultem composites containing untreated (UN) and Grignard-treated (GT) nMFI as a function of MFI loading (1 – 10 vol.%) and annealing conditions (150  $^\circ C$  (solid line) and 230  $^\circ C$  (dot line) for 24 h, respectively). 110
- Figure 6.5: SEM images of PVAc composites containing 10 vol.% of untreated (UN) and surface-treated (GT and ST) nMFI, which are annealed at 20 and 100  $^\circ C$  for 24 h, respectively: UN (a) 20  $^\circ C$  and (b) 100  $^\circ C$ , GT (c) 20  $^\circ C$  and (d) 100  $^\circ C$ , and ST (e) 20  $^\circ C$  and (f) 100  $^\circ C$ . 111
- Figure 6.6: SEM images of PVAc composites containing 10 vol.% of untreated (UN) and surface-treated (GT and ST)  $\mu$ MFI, which are annealed at 20 and 100  $^\circ C$  for 24 h, respectively: UN (a) 20  $^\circ C$  and (b) 100  $^\circ C$ , GT (c) 20  $^\circ C$  and (d) 100  $^\circ C$ , ST (e) 20  $^\circ C$  and (f) 100  $^\circ C$ , and HST (g) 20  $^\circ C$  and (h) 100  $^\circ C$ . 112

- Figure 6.7: Stress-strain curves for pure PVAc and PVAc composites containing 10 vol.% of UN- $\mu$ MFI, annealed at 20, 40 and 100 °C for 24 h, respectively.. 115
- Figure 6.8: Tensile strength of PVAc composites containing UN-, GT- and ST-nMFIs or  $\mu$ MFIs as a function of MFI loading (1 – 10 vol.%) and annealing conditions ((a) 20 °C (solid line) and (b) 100 °C (dot line) for 24 h, respectively)..... 116
- Figure 6.9: Elongation at break of PVAc composites containing UN-, GT- and ST-nMFIs or  $\mu$ MFIs as a function of MFI loading (1 – 10 vol.%) and annealing conditions ((a) 20 °C (solid line) and (b) 100 °C (dot line) for 24 h, respectively)..... 117
- Figure 6.10: Mechanical properties (a) tensile strength and b) elongation at break) of pure PVAc and PVAc composites containing 10 vol.% of UN-, GT-, and ST-nMFIs or  $\mu$ MFIs as a function of the annealing temperature (20, 40, and 100 °C for 24 h, respectively). (HST denotes ST- $\mu$ MFIs with a higher content of Mg(OH)<sub>2</sub> (20 wt%))..... 119
- Figure 6.11: (a) DSC curves (b) width of the glass transition ( $\Delta T$ ) of pure PVAc and PVAc composites containing 10 vol% of UN-, GT and ST-nMFIs as a function of the annealing temperature (20, 40, and 100 °C for 24 h, respectively)... 122
- Figure 6.12: DSC curves of pure PVAc and PVAc composites containing 10 vol% of UN-, GT- and ST- $\mu$ MFIs, which are annealed at 20 °C for 24 h..... 123
- Figure 6.13: XRD patterns of (a) pure PVAc and PVAc composite films containing UN- $\mu$ MFI, which are annealed at 20 and 100 °C for 24 h, respectively, (b) pure PVAc and PVAc composite films composed of UN-, GT- and ST-MFI  $\mu$ MFIs after annealing at 100 °C for 24 h, respectively..... 127
- Figure A.1: (a and b) TEM images of AuNPs: a) 30 nm and b) 80 nm, and (c) SEM image of 60 nm AgNCs..... 142
- Figure A.2: Proposed combined swelling-heteroaggregation (CSH) process..... 144
- Figure A.3: Optical microscopy images of PS beads in a) DI water, b) 50 vol.% THF-water solution, and c) DI water after washing THF..... 144
- Figure A.4: UV-Vis spectra of 30 nm AuNPs in THF-water solutions at various times: (A) 50 vol.% THF-water solution in the absence of PS beads, (B) 50 vol.% THF-water solution in the presence of PS beads, (C) 70 vol.% THF-water solution in the absence of PS beads..... 146
- Figure A.5: SEM images of 30 nm AuNP-coated PS beads obtained from (A) 50 vol.% THF-water solution ( $n$  = the ratio of the number of metal NPs to PS particles =  $1.3 \times 10^5$ ), (B) 70 vol.% THF-water solution ( $n = 1.3 \times 10^5$ ), (C) 50 vol.% THF-water solution ( $n = 1.0 \times 10^5$ )..... 147

- Figure A.6: (A and B) UV-Vis spectra of 80 nm AuNPs in 50 vol.% THF-water solutions at various times: (A) in the absence of PS beads, (B) in the presence of PS beads. (C) UV-vis spectra of AuNP-coated PS beads with different levels of metal coverage dispersed in DI water: (a) 30 nm AuNPs ( $n = \text{the ratio of the number of metal NPs to PS particles} = 1.3 \times 10^5$ ), (b) 30 nm AuNPs ( $n = 9.8 \times 10^5$ ), (c) 80 nm AuNPs ( $n = 1.0 \times 10^5$ ), (d) 80 nm AuNPs ( $n = 4.0 \times 10^5$ ) (The spectra measured from metal-coated PS beads were referenced to that of a plain PS bead.)..... 149
- Figure A.7: SEM and dark field images (a-c) and Surface-enhanced Raman spectra (d) and the corresponding UV-vis spectra (d, inset) of 10  $\mu\text{m}$  PS beads coated by 30 nm AuNPs with different levels of metal coverage: (a)  $n = \text{the ratio of the number of metal NPs to PS particles} = 1.3 \times 10^5$ , (b)  $n = 2.5 \times 10^5$ , (c)  $n = 9.8 \times 10^5$  ..... 151
- Figure A.8: AFM surface images (top) of a PS bead covered by 30 nm AuNPs (corresponding Figure A.7c) and line profiles along the line (bottom) on the AFM images: (a) a single bead ( $10 \times 10 \mu\text{m}^2$ ), (b) center area of a single bead ( $2 \times 2 \mu\text{m}^2$ )..... 151
- Figure A.9: SEM and dark field images (a-c) and Surface-enhanced Raman spectra (d) and the corresponding UV-vis spectra (d, inset) of 10  $\mu\text{m}$  PS beads coated by 80 nm AuNPs with different levels of metal coverage: (a)  $n = 1.0 \times 10^5$ , (b)  $n = 2.0 \times 10^5$ , (c)  $n = 4.0 \times 10^5$  ..... 154
- Figure A.10: SEM and dark field images (a-c) and Surface-enhanced Raman spectra (d) and the corresponding UV-vis spectra (d, inset) of 10  $\mu\text{m}$  PS beads coated by 60 nm AgNCs with different levels of metal coverage: (a)  $n = 1.0 \times 10^9$ , (b)  $n = 2.0 \times 10^9$ , (c)  $n = 3.5 \times 10^9$  ..... 157



## SUMMARY

Inorganic/polymer hybrid materials have a high potential to enable major advances in material performance in a wide range of applications. This research focuses on characterizing and tailoring the physics and chemistry of inorganic-polymer interfaces in fabricating high-performance zeolite-polymer mixed-matrix membranes for energy-efficient gas separations. In addition, the topic of novel metal nanoparticle-coated polymer microspheres for optical applications is treated in the Appendix.

In zeolite/polymer mixed-matrix membranes, interfacial adhesion and interactions between dope components (zeolite, polymer and solution) play a crucial role in determining interfacial morphology and particle dispersion. The overarching goal is to develop accurate and robust tools for evaluating adhesion and interactions at zeolite-polymer and zeolite-zeolite interfaces in mixed-matrix membrane systems. This knowledge will be used ultimately for selecting proper materials and predicting their performance. This project has two specific goals: (1) development of an AFM methodology for characterizing interfacial interactions and (2) characterization of the mechanical, thermal, and structural properties of zeolite-polymer composites and their correlation to the zeolite-polymer interface and membrane performance. The research successfully developed an AFM methodology to determine interfacial interactions, and these were shown to correlate well with polymer composite properties. The medium effect on interactions between components was studied. We found that the interactions between two hydrophilic silica surfaces in pure liquid (water or NMP) were described qualitatively by the DLVO theory. However, the interactions in NMP-water mixtures

were shown to involve non-DLVO forces arising from bridging of NMP macroclusters on the hydrophilic silica surfaces. The mechanism by which nanostructured zeolite surfaces enhanced in zeolite-polymer interfacial adhesion was demonstrated to be reduced entropy penalties for polymer adsorption and increased contact area.

Metal nanoparticle (NP)-coated polymer microspheres have attracted intense interest due to diverse applications in medical imaging and biomolecular sensing. The goal of this project is to develop a facile preparation method of metal-coated polymer beads by controlling metal-polymer interactions. We developed and optimized a novel solvent-controlled, combined swelling-heteroaggregation (CSH) technique. The mechanism governing metal-polymer interaction in the fabrication was determined to be solvent-controlled heteroaggregation and entanglement of NPs with polymer, and the optical properties of the metal/polymer composite beads were shown to make them useful for scattering contrast agent for biomedical imaging and SERS (Surface-Enhanced Raman Scattering) substrates.

# CHAPTER 1

## INTRODUCTION

### 1.1. THE ROLE OF INTERFACES IN DESIGNING HYBRID MATERIALS

Interfaces between components play a crucial role in designing high-performing, multifunctional materials such as optical and photonic devices, functional film surfaces, colloids and hybrid composite materials [1-7]. In particular, research in inorganic-polymer composite materials has involved extensive efforts to tailor and enhance interfacial adhesion between the inorganic and polymer species, in order to maximize the performance of composites in terms of mechanical, electrical, and thermal properties [8-15]. Knowledge of the adhesion and interaction between dissimilar inorganic and organic phases can lead to an understanding of the underlying interfacial physics and chemistry. Based on this knowledge, interfaces may be designed and tailored for fabricating novel and high-performance hybrid materials.

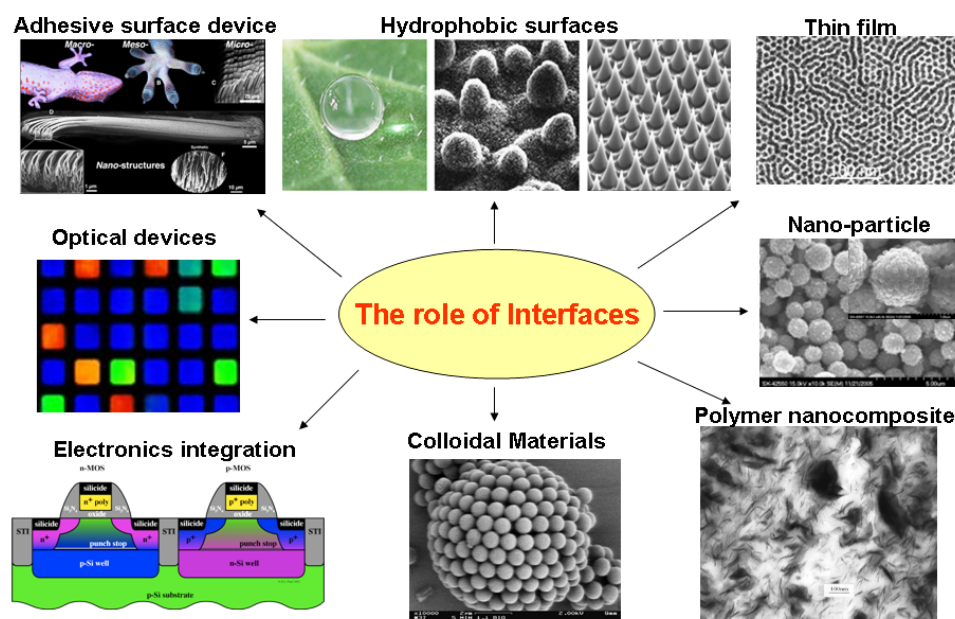


Figure 1.1: The role of interfaces in the field of materials engineering.

## 1.2. ZEOLITE-POLYMER INTERFACES IN MIXED-MATRIX MEMBRANES

Mixed-matrix membranes are hybrid composite materials composed of a polymer, a molecular sieve, and possibly other phases, depending on the nature of their applications [16-24]. Zeolites (silicates and aluminosilicates) have been widely used as inorganic molecular sieves [17, 18, 21-25]. In particular, the interfacial adhesion between the inorganic zeolite and the polymer component is considered critical for making defect-free, and thus highly-performing membranes [11, 17, 25-29]. Furthermore, inorganic particle-particle interaction can have a significant influence on particle-polymer interfacial morphology and particle dispersion in composite materials, which is directly related to membrane performance [17, 25]. Hence, it is desirable to develop accurate and robust tools for evaluating zeolite-polymer interfacial adhesion and zeolite particle-particle interaction in mixed-matrix membranes, and ultimately, to use them for selecting proper materials and predicting their performance.



Figure 1.2: Scheme of mixed-matrix membrane design.

## 1.3. THESIS OVERVIEW

In this thesis, the role of the adhesion and interaction at inorganic-polymer and inorganic-inorganic interfaces was investigated in fabricating high-performance zeolite-polymer composites for use as mixed-matrix membranes for energy-efficient gas separations. A methodology for evaluating the adhesion and interaction between components in mixed-matrix membranes was developed by using the colloidal probe AFM (Atomic Force Microscopy) technique. These results were related to the mechanical, structural and thermal properties of composites.

Chapter 2 presents research background and objectives associated with issues in fabricating zeolite-polymer mixed-matrix membranes for gas separations. Additionally, the AFM technique for measuring interfacial forces between two surfaces and the high-throughput mechanical characterization (HTMECH) tool for measuring mechanical properties of composite films are introduced. The novel zeolite colloidal probe AFM technique for measuring zeolite-polymer adhesions in air is covered in Chapter 3. Chapter 4 describes the silica colloidal probe method for evaluating adhesion and interactions at inorganic silica-polymer and silica-silica interfaces in different mediums. The role of non-DLVO forces in interactions between inorganic silica surfaces in solution is investigated in this chapter. For comparison, the interaction between asymmetric silica surfaces in solution is examined in Chapter 5. Chapter 6 presents characterization of the mechanical, structural and thermal properties of zeolite-polymer composite films, and their correlation to the AFM interfacial studies. The effect of zeolite surface modification on the interfacial morphology and macroscopic properties of polymer composites is studied in this chapter. Conclusions and recommendations for future work are provided in Chapter 7.

#### **1.4. REFERENCES**

1. Armstrong, N.R., C. Carter, C. Donley, A. Simmonds, P. Lee, M. Brumbach, B. Kippelen, B. Domercq, and S.Y. Yoo, *Thin Solid Films*, 2003. **445**(2): p. 342-352.
2. Capasso, F., *MRS Bull.*, 1991. **16**(6): p. 23-29.
3. Capasso, F., *Thin Solid Films*, 1992. **216**(1): p. 59-67.
4. Caruso, F., R.A. Caruso, and H. Mohwald, *Science*, 1998. **282**(5391): p. 1111-1114.
5. KlembergSapieha, J.E., D. Poitras, L. Martinu, N.L.S. Yamasaki, and C.W. Lantman, *J. Vac. Sci. Technol. A*, 1997. **15**(3): p. 985-991.

6. Lee, J.H., M.A. Mahmoud, V. Sitterle, J. Sitterle, and J.C. Meredith, *J. Am. Chem. Soc.*, 2009. **131**(14): p. 5048-5049.
7. Watkins, N.J., L. Yan, and Y.L. Gao, *Appl. Phys. Lett.*, 2002. **80**(23): p. 4384-4386.
8. Eitan, A., K.Y. Jiang, D. Dukes, R. Andrews, and L.S. Schadler, *Chem. Mater.*, 2003. **15**(16): p. 3198-3201.
9. Leu, C.M., Z.W. Wu, and K.H. Wei, *Chem. Mater.*, 2002. **14**(7): p. 3016-3021.
10. Alves, N.M., J.F. Mano, E. Balaguer, J.M.M. Duenas, and J.L.G. Ribelles, *Polymer*, 2002. **43**(15): p. 4111-4122.
11. Amanuel, S., A.N. Gaudette, and S.S. Sternstein, *J. Polym. Sci., Part B: Polym. Phys.*, 2008. **46**(24): p. 2733-2740.
12. Ash, B.J., D.F. Rogers, C.J. Wiegand, L.S. Schadler, R.W. Siegel, B.C. Benicewicz, and T. Apple, *Polym. Compos.*, 2002. **23**(6): p. 1014-1025.
13. Demir, H., D. Balkose, and S. Ulku, *Polym. Degrad. Stabil.*, 2006. **91**(5): p. 1079-1085.
14. Libby, B., W.H. Smyrl, and E.L. Cussler, *AIChE J.*, 2003. **49**(4): p. 991-1001.
15. Metin, D., F. Tihminhoglu, D. Balkose, and S. Ulku, *Composites Part A*, 2004. **35**(1): p. 23-32.
16. Anson, M., J. Marchese, E. Garis, N. Ochoa, and C. Pagliero, *J. Membr. Sci.*, 2004. **243**(1-2): p. 19-28.
17. Chung, T.S., L.Y. Jiang, Y. Li, and S. Kulprathipanja, *Prog. Polym. Sci.*, 2007. **32**(4): p. 483-507.
18. Yong, H.H., N.C. Park, Y.S. Kang, J. Won, and W.N. Kim, *J. Membr. Sci.*, 2001. **188**(2): p. 151-163.

19. Cornelius, C.J. and E. Marand, *Polymer*, 2002. **43**(8): p. 2385-2400.
20. Cornelius, C.J. and E. Marand, *J. Membr. Sci.*, 2002. **202**(1-2): p. 97-118.
21. Jiang, L.Y., T.S. Chung, and S. Kulprathipanja, *AIChE J.*, 2006. **52**(8): p. 2898-2908.
22. Mahajan, R., R. Burns, M. Schaeffer, and W.J. Koros, *J. Appl. Polym. Sci.*, 2002. **86**(4): p. 881-890.
23. Mahajan, R. and W.J. Koros, *Polym. Eng. Sci.*, 2002. **42**(7): p. 1420-1431.
24. Mahajan, R. and W.J. Koros, *Polym. Eng. Sci.*, 2002. **42**(7): p. 1432-1441.
25. Husain, S. and W.J. Koros, *J. Membr. Sci.*, 2007. **288**(1-2): p. 195-207.
26. Lee, J.H., B.J.R. Thio, T.H. Bae, and J.C. Meredith, *Langmuir*, 2009. **25**(16): p. 9101-9107.
27. Li, Y., H.M. Guan, T.S. Chung, and S. Kulprathipanja, *J. Membr. Sci.*, 2006. **275**(1-2): p. 17-28.
28. Shu, S., S. Husain, and W.J. Koros, *J. Phys. Chem. C*, 2007. **111**(2): p. 652-657.
29. Vankelecom, I.F.J., S. VandenBroeck, E. Merckx, H. Geerts, P. Grobet, and J.B. Uytterhoeven, *J. Phys. Chem.*, 1996. **100**(9): p. 3753-3758.

## CHAPTER 2

### BACKGROUND

#### 2.1. MIXED-MATRIX MEMBRANES

Gas separation by membranes is a dynamic and rapidly growing field. Current applications of membrane-based gas separation include oxygen and nitrogen enrichment, hydrogen recovery, natural gas separation and the removal of volatile organic compounds from effluent streams [1-5]. A number of advantages, including low capital and operating costs, low energy requirements and easy of operation are offered by membrane separation, compared to other competitive technologies such as adsorption and distillation [1-3]. In particular, polymeric membranes have the advantages of desirable mechanical properties and economical processing capabilities. Imide-type polymers are commonly used as membrane matrices due to their high thermal and chemical stability and favorable transport properties [6-11].

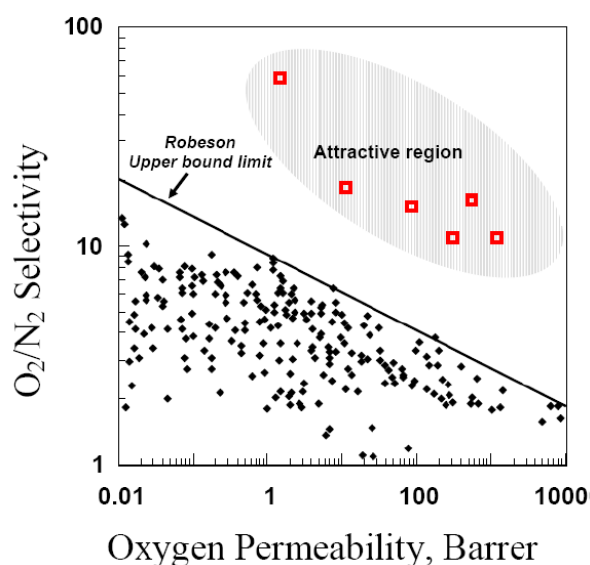


Figure 2.1: Upper-bound trade-off curve in transport properties for oxygen/nitrogen gas pair [12]. (□: Typical molecular sieves and ◆: Rubbery and glassy polymer)



Unfortunately, a general trade-off exists between permeability and selectivity for polymer-only membranes, as proposed by Robeson (Figure 2.1) [12]. This trade-off leads to an “upper bound” on membrane performance that limits applications of these materials to displace conventional, energy-intensive separation. To create new materials that move beyond this limitation, mixed-matrix membranes that incorporate size-discriminating inorganic materials, such as zeolites and other molecular sieves, have been investigated vigorously in recent years [2, 9, 13-23].

### 2.1.1. Issues in Mixed-Matrix Membranes

#### 2.1.1.1. Zeolite-Polymer Interfaces

In zeolite-polymer mixed-matrix membranes, however, interfacial voids often exist between the zeolite and the polymer matrix, as illustrated in Figure 2.2 [2, 9, 17, 18, 20, 23]. These defects cause nonselective leakage of penetrants through the interfacial voids. It is thought that these defects form in part due to poor adhesion between the polymer and zeolite matrix [2, 9, 17, 18, 20, 23].

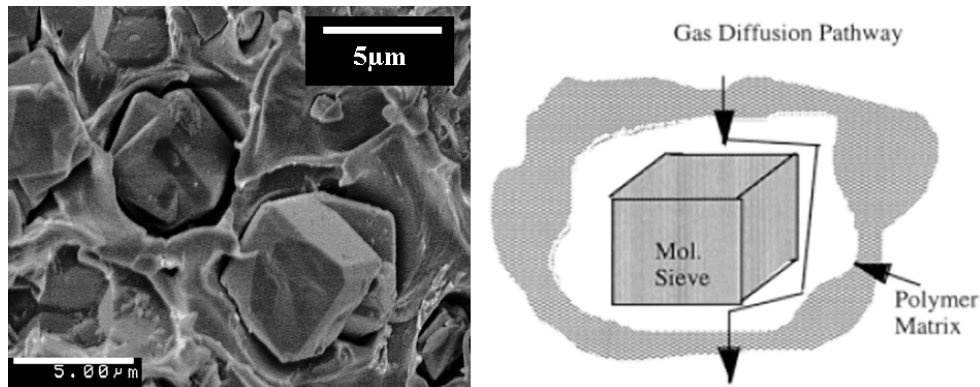


Figure 2.2: Sieve in a cage morphology and schematic gas flow through interfacial voids around the zeolite surface in zeolite-polymer mixed matrix membranes.

Even though intensive research to enhance adhesion between the polymer and zeolite materials has been carried out using silane coupling agents, integral chain linkers, and polymer adducts on the molecular sieves, fabrication of defect-free mixed-matrix

membranes remains a significant challenge [2, 20, 24, 25]. Knowledge of the mechanism of adhesion between polymer and zeolite materials would support the design of defect-free, and thus highly permselective, composite membranes. Above all, accurate and direct tools for characterizing the physical chemistry of interfaces are desirable for understanding the role of interfacial adhesion in mixed-matrix membranes. It is recognized, however, that a full consideration of defect formation must involve an understanding of the effects of other factors, including the solvent-dependent adhesion forces, residual stresses, and film formation conditions [20, 24].

#### ***2.1.1.2. Phase Separation Kinetics***

Research on membrane materials is carried out mostly using dense films made by the gradual removal of the solvent. However, practical membranes used for separations have asymmetric structures such as hollow fibers where a thin skin layer performs the actual separation and the porous layer underneath acts as a support to the skin, as shown in Figure 2.3 [2, 20, 22].

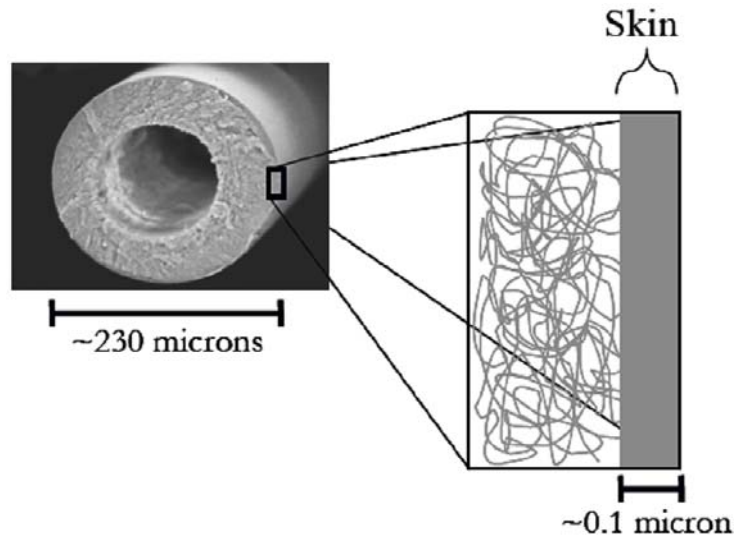


Figure 2.3: Asymmetric hollow fiber membrane.

Asymmetric membranes are typically formed in a single step via a dry jet-wet quench spinning process where the polymer dope solution contacts with a non-solvent in the quench bath, as shown in Figure 2.4 [2, 20, 22]. The industrial preference for the non-solvent for the quench bath is water due to safety and environmental reasons. *N*-methyl-2-pyrrolidone (NMP) is typically used as a solvent for imide-type polymers due to its relatively benign nature [20].

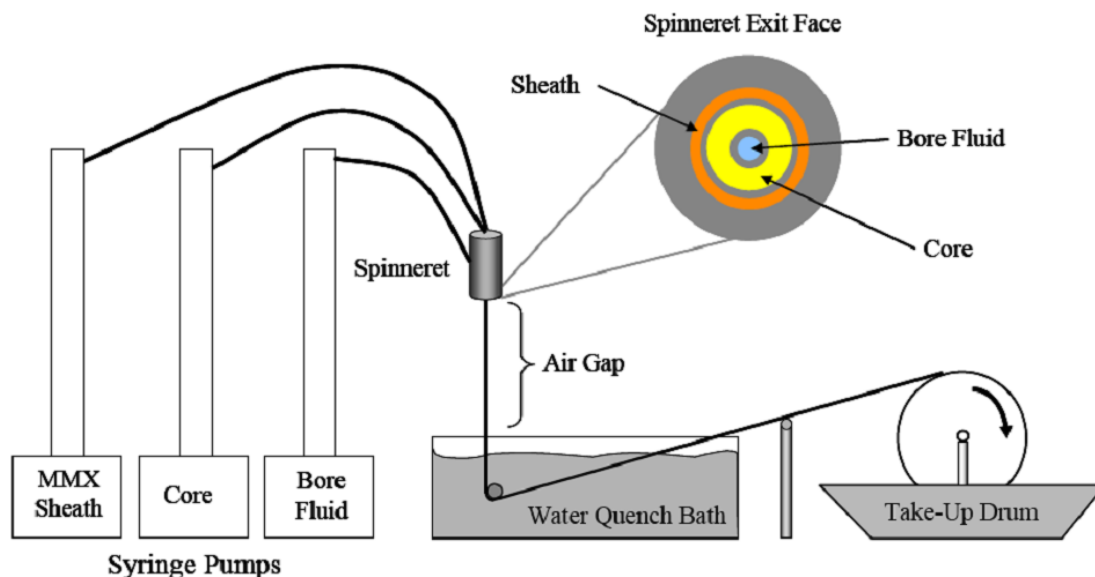


Figure 2.4: Schematic of hollow fiber spinning set-up [20].

In this spinning process, the non-solvent (water) penetrates the membrane and the solvent (NMP) diffuses out into the quench bath, resulting in the phase separation of the membrane, as illustrated in Figure 2.5. Hence, the final morphology of the asymmetric membrane is controlled by phase separation kinetics [20].

For mixed-matrix membranes, the presence of zeolites in the spinning dope is known to affect long term dope stability, phase separation kinetics and hence the morphology of the membranes [2, 9, 17, 20]. The stability of the dope refers to the characteristic of the zeolite particles to remain homogeneously suspended in the spinning dope, and it depends on the interactions of the zeolite surface with the remaining

components of the dope [17, 20]. Furthermore, it is believed that the formation of defects (sieve-in-cage) in asymmetric mixed-matrix membranes is attributed to phase separation occurring at zeolite-polymer interfaces [9, 17, 20]. An understanding of the zeolite-zeolite and zeolite-polymer interactions in different media (air or solvent (NMP)/non-solvent (water) mixtures) enables insight into membrane morphology, particle stability and dispersion in the solution.

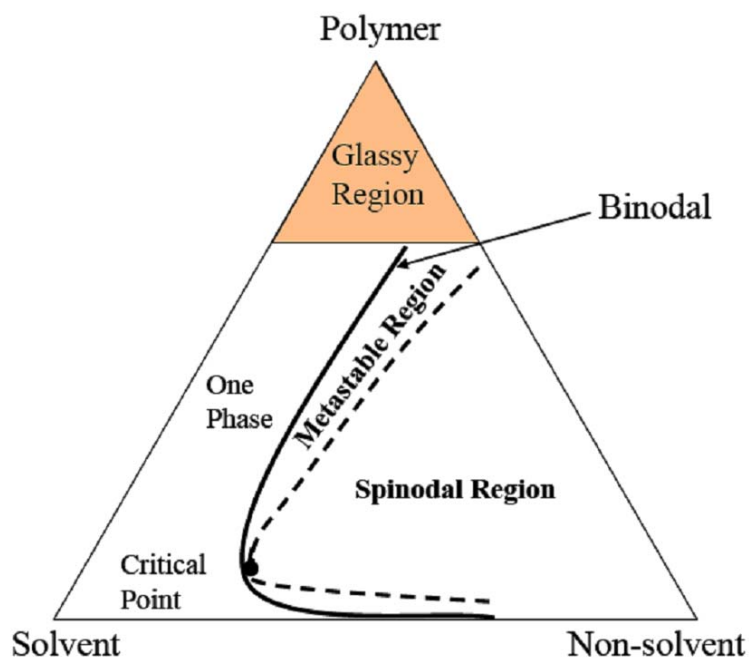


Figure 2.5: Ternary phase diagram of polymer, solvent and non-solvent.

## 2.1.2. Materials

### 2.1.2.1. Polymers

Glassy polymers (polyimides and polyetherimides) and a rubbery polymer (polyvinyl acetate, PVAc) have been used widely for gas separation membranes. Matrimid<sup>®</sup> 5218 (polyimide) and Ultem<sup>®</sup> 1000 (polyetherimide) are commercially available polymers. In addition, 6FDA (2,2-bis(3,4-carboxyphenyl)hexafluoropropane dianhydride)-based copolyimides have been studied intensively as a result of their high

efficiency as gas separation membranes. The diamines used to form 6FDA based copolyimides were (4,4'-hexafluoroisopropylidene)diamine (6FpDA) and diaminomesitylene (DAM) [6-8]. One of the 6FDA based copolyimides is formed by replacing a portion of the diamine of 6FDA-DAM with 3,5-diaminobenzoic acid (DABA). Chemical structures of polymer materials are shown in Figure 2.6.

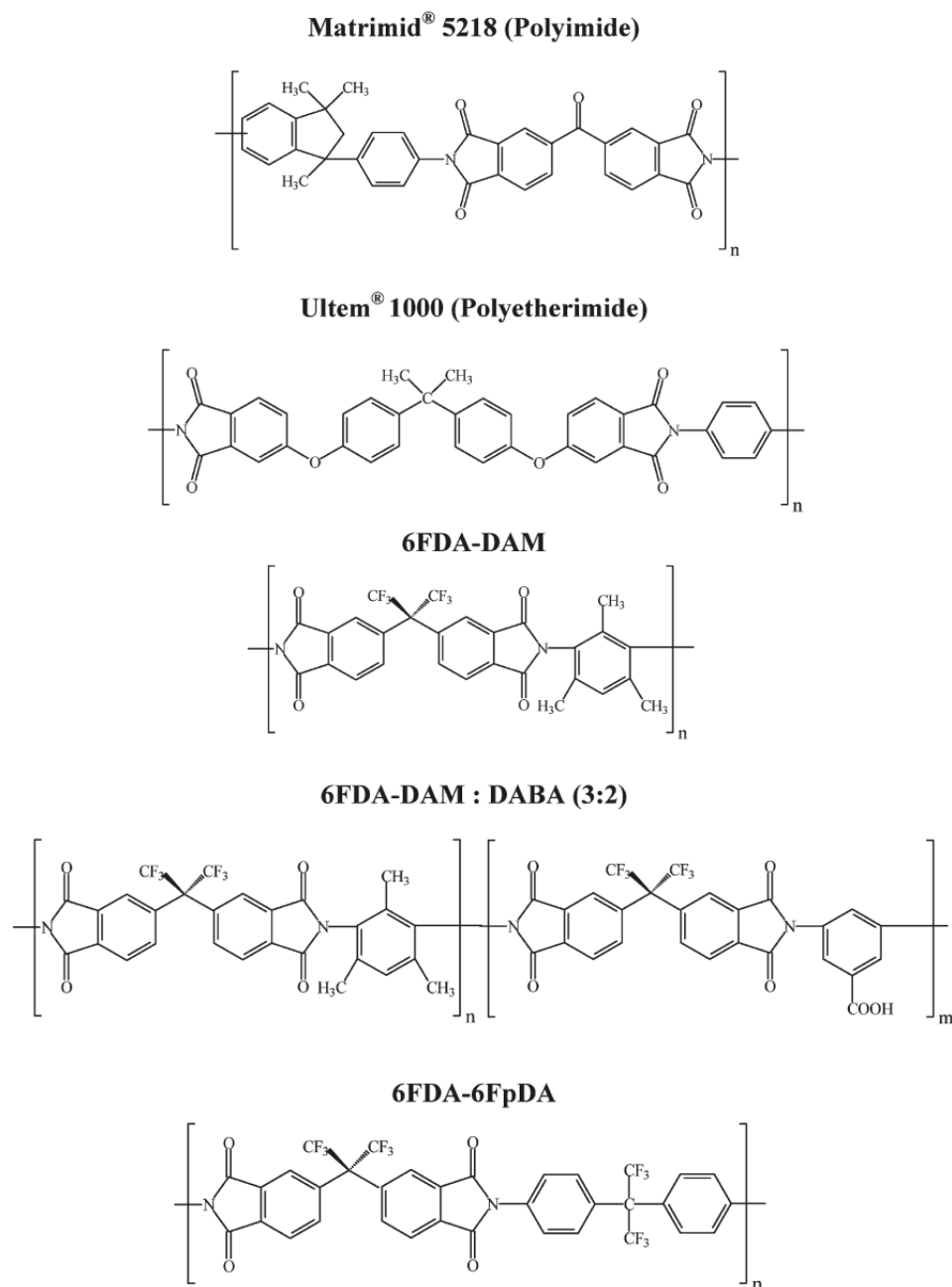


Figure 2.6: Chemical structures of polymer materials.

### 2.1.2.2. Zeolites

#### 2.1.2.2.1. Pure-Silica MFI (ZSM-5: Zeolite Socony Mobil-Five)

Zeolites have attracted significant attention recently in separation processes and shape-selective catalysis due to their intrinsic molecular-sieving properties [26, 27]. In particular, a pure-silica MFI zeolite has been intensively investigated for applications in gas separation and catalysis [13-15]. Chemically, MFI hydrophilicity can be effectively tuned by its Si/Al ratio. Pure-silica MFI is widely regarded as the most hydrophobic among other types of aluminosilicate zeolites, so that it has a very low water adsorption and very high preference for the adsorption of organic molecules [28-30].

MFI zeolite is composed of  $\text{SiO}_2$  tetrahedra having pore sizes between 5.1 and 5.6 Å. The structure of MFI is a combination of two interconnected channel systems that consist of sinusoidal 10-membered-rings along the a-axis, (100) surface, a straight channel along the b-axis, (010) surface, and a tortuous pore channel along the c-axis, (001) surface, as shown in Figure 2.7 [31]. The molecular size-selection characteristics of zeolites with well-defined pore structures can improve gas separation efficiency of mixed-matrix membranes. Pure-silica MFI crystals are synthesized hydrothermally from TEOS/TPA-OH or -Br/water solutions. The size of crystals can be controlled by adjusting the reactant composition, and reaction time and temperature [19, 32].

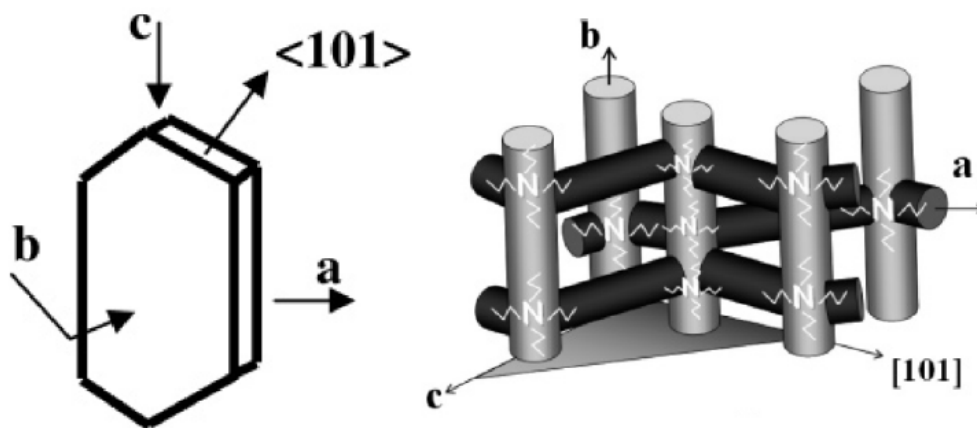


Figure 2.7: Schematic of the pore structure of pure-silica MFI [31].

#### 2.1.2.2.2. Surface Modification of Pure-Silica MFI

Many studies of zeolite modification to promote adhesion between the inorganic and polymer species have focused primarily on organic functionalization using silane coupling agents, integral chain linkers, and polymer coatings [15, 16, 25, 33]. In particular, aminosilane treatments using APDMES ( $\gamma$ -aminopropyltrimethylethoxy silane) or APTS (aminopropyltriethoxy silane) have been commonly used for chemically modifying zeolite surfaces [20, 25, 34]. Unfortunately, although these organic functionalization routes reduce interfacial voids, they are not able to eliminate defects completely. In addition, use of coupling agents is usually limited to a specific polymer-filler pair depending on the chemistry of the polymeric materials.

Recently, highly roughened zeolite surfaces were proposed to enhance adhesion at the polymer-particle interface and yield defect-free composite membranes with enhanced gas separation efficiency [18, 19, 23]. For a better understanding of the roughening effect, Grignard or solvothermal treatment were employed to create  $\text{Mg}(\text{OH})_2$  inorganic whisker or asperity nanostructures on the MFI zeolite surface, as shown in Figure 2.8. It is thought that whiskers lower the entropy penalty for polymer adsorption and increase contact area, thereby enhancing polymer-zeolite adhesion.

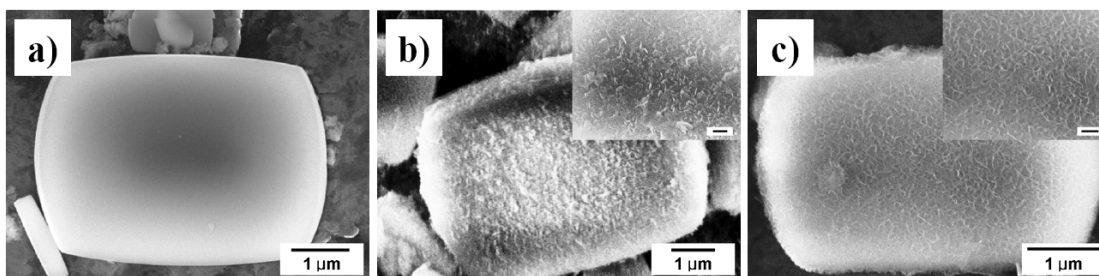


Figure 2.8: SEM images of untreated and surface-treated MFI microparticles ( $\sim 5 \mu\text{m}$ ); (a) untreated, (b) Grignard-treated and (c) Solvothermally-treated.

## 2.2. INTERFACE CHARACTERIZATION TECHNIQUE

### 2.2.1. Colloidal Probe Atomic Force Microscopy (AFM) Technique

AFM can characterize solid surface properties at the microscopic and submicroscopic scales, and it has contributed considerably to our understanding of interactions acting between surfaces [35-45]. Since commercial AFM tips are usually silicon or silicon-nitride, the tips are chemically modified or replaced with particles to study other materials. The tip material may be modified by coating a thin film of metal or polymer, or by depositing self-assembled monolayers of organic silanes or thiols with a desirable functionality [46-49]. However, due to the difficulty in uniformly modifying and characterizing the tips, usefulness of these approaches is limited. The colloidal probe technique, where a particle with a diameter of 2-20  $\mu\text{m}$  can be attached to regular or tipless cantilevers, broadens the spectrum of materials that can be used in surface force measurements [24, 41-45, 50-54]. Schematics of AFM surface force measurement and typical force-distance curves obtained during approach and retraction are shown in Figure 2.9.

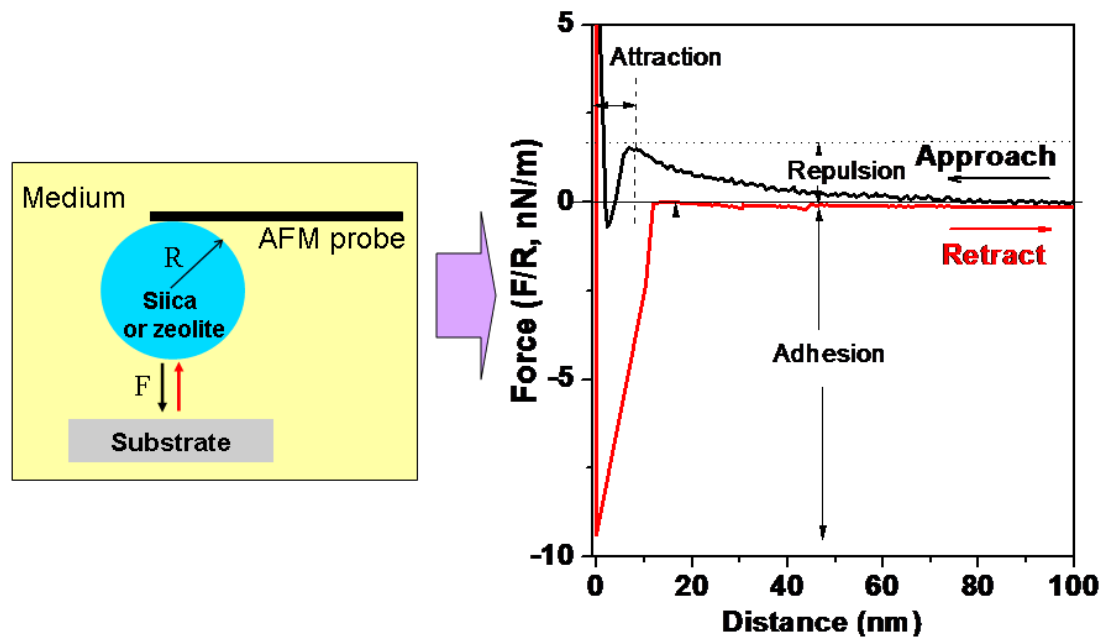


Figure 2.9: Schematics of AFM force measurement and a typical force-distance curve.



Repulsive and attractive forces can be measured from approach force curves, while adhesive forces are determined from the average well depth of the retraction portion of force curves. A single inorganic particle (zeolite or silica) can be attached onto the cantilever. Hence, It is possible to measure adhesion and interaction at inorganic-polymer and inorganic-inorganic interfaces in various mediums by adjusting parameters such as probes, substrates (inorganic or polymer) and mediums (air or liquids).

### **2.2.2. Characterization of Polymer Composite Properties**

The inorganic filler-polymer interaction is known to strongly influence the macroscopic properties, such as mechanical, thermal and structural properties of polymer composites [55-65]. Hence, the use of such composite property measurements to gain insight into interfacial adhesion between the hybrid inorganic-organic phases can be a great tool for interface study. Ultimately, it can guide us to the appropriate selection of materials and the design of composite materials.

#### ***2.2.2.1. High-Throughput Mechanical Characterization (HTMECH)***

Given the time and effort involved in careful AFM force-distance measurements, a mechanical property measurement is desirable to have a relatively fast and simple tool that provides a quantitative measure of the interfacial adhesion. In previous years, the Meredith group developed a HTMECH apparatus that was integrated into combinatorial polymer development strategies, as shown in Figure 2.10 [66-69].

HTMECH uses a smooth-tipped ‘needle’ to deform a membrane sample that is mounted between two steel plates. For sufficiently-thin membranes (usually less than 200 microns), the material is stretched biaxially in tension, and accurate measurements of tensile properties are possible. This includes tensile strength, elongation at break and tensile modulus that correlate strongly with more conventional uniaxial assays, e.g., the Instron™ instruments. The high-throughput nature of HTMECH derives from the use of

a sample grid holding up to 100 samples simultaneously, and the automated control of the indenter that allows a range of strain rates ( $< 1 \text{ mm/s}$  to  $2000 \text{ mm/s}$ ) to be rapidly screened.

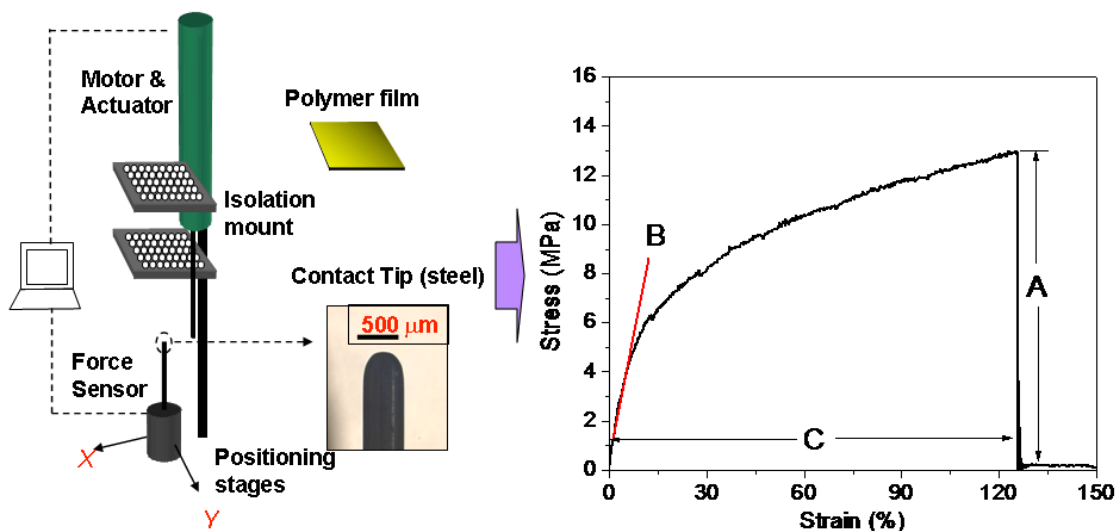


Figure 2.10: Schematics of HTMECH and a typical strain-stress curve (A: ultimate tensile strength, slope of B: initial tensile modulus and C: elongation at break).

#### 2.2.2.2. Thermal and Structural Characterization

Differential scanning calorimetry (DSC) can be employed to characterize the thermal properties of the composites. For amorphous polymers, the glass transition behavior of the polymer composite is characterized by determining glass transition temperature ( $T_g$ ) and the width of the glass transition ( $\Delta T$ ) from DSC heating curves. X-ray diffraction (XRD) is used to examine the structural properties of the composite films. The interfacial morphology of polymer composites can be investigated by examining scanning electron microscopy (SEM) images of fracture surfaces of the composites.

### 2.3. RESEARCH OBJECTIVES

The research objectives are to develop accurate and robust tools for evaluating adhesion and interactions at zeolite-polymer and zeolite-zeolite interfaces in mixed-

matrix membrane systems. It is envisioned that this knowledge will be used ultimately for selecting proper materials and predicting their performance, as shown in Figure 2.11.

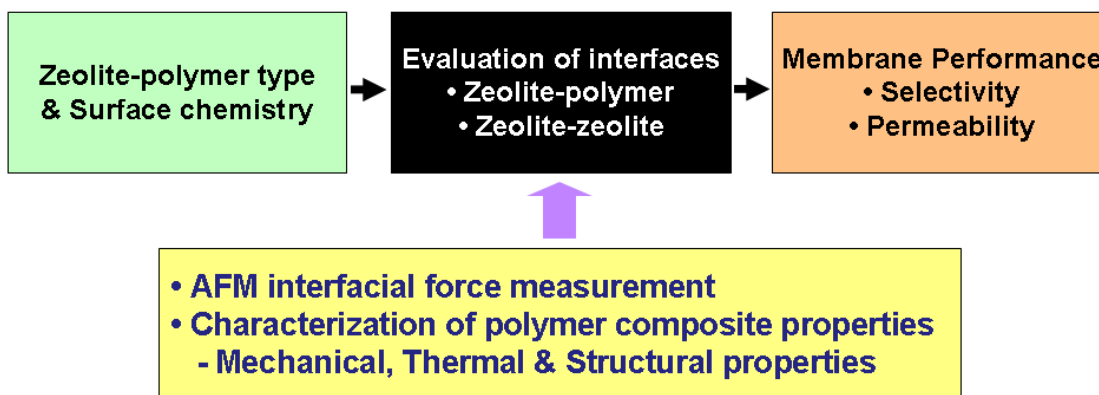


Figure 2.11: Schematics of the overall research goal.

The specific goals are as follows:

### 1. Develop an AFM methodology for characterizing interfacial interactions

This research aims to develop an AFM technique to measure inorganic-polymer adhesion and inorganic-inorganic interactions in various media. This method will allow us to identify the mechanisms governing interactions between components and, ultimately, connect these mechanisms to the mixed-matrix membrane morphology. However, it is important to note that the interfacial forces measured by the AFM technique may differ from the actual interactions between components during membrane fabrication. The motion of the particle used in the AFM experiment is confined to one degree of freedom and subject to shear and torsion motions after contact with the surface, compared to that of free particles having three degree of freedom [37]. Furthermore, a complex change in interactions between components in dope solution takes place in a dynamic environment where medium conditions change by solvent exchange, polymer phase separation and evaporation, simultaneously, while the AFM technique provides us with the equilibrium interaction behavior between two surfaces in a certain medium.

Here, we strive to understand driving forces acting during the dynamic membrane fabrication process by characterizing the equilibrium interactions between components.

a. Inorganic materials:

- Zeolite: bare MFI and surface-modified MFI with aminosilane (APDMES) or Grignard treatments.
- Amorphous Silica

b. Polymers:

- Polyimide (Matrimid<sup>®</sup> 5218 and 6FDA-based copolyimides)
- Polyetherimide (Ultem<sup>®</sup> 1000)
- Polyvinyl acetate (PVAc)
- Polystyrene (PS)

c. Measurement conditions:

- In air (20 °C/ relative humidity  $RH = 20, 35$  and  $75\%$ )
- In NMP-water mixtures

## **2. Characterize and correlate polymer composites properties**

A second major goal is to characterize the properties of zeolite-polymer composites, and correlate them to the zeolite-polymer interface and membrane performance. The composite properties include mechanical, thermal and structural properties.

a. Investigation of the effects of MFI zeolite on the properties of composite films.

- Zeolite loading:  $1 \sim 10$  vol. %
- Zeolite size:  $\sim 300$  nm and  $\sim 5$   $\mu$ m
- Zeolite chemistry: bare, and Grignard and solvothermally treated

b. Investigation of the effects of polymer characteristics and film annealing conditions on the properties of composite films.

- Polymer: glassy (Ultem<sup>®</sup> 1000) and rubbery (PVAc) polymer
- Annealing temperatures: sub-, around- and above- $T_g$ .

c. Correlating the properties to the interface and performance of mixed-matrix membrane.

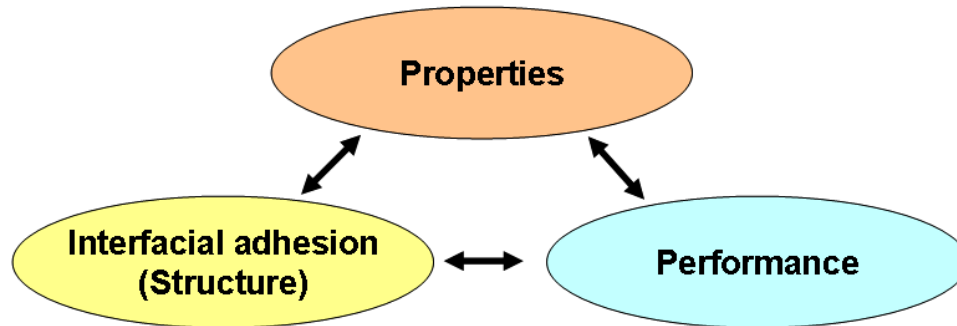


Figure 2.12: Relationship of properties, interface and performance.

## 2.4. REFERENCES

1. Berry, R.I., Chem. Eng., 1981. **88**: p. 63-67.
2. Chung, T.S., L.Y. Jiang, Y. Li, and S. Kulprathipanja, Prog. Polym. Sci., 2007. **32**(4): p. 483-507.
3. Strathman, H., J. Membr. Sci., 1981. **9**: p. 121-189.
4. Ho, W.S.W. and K.K. Sirkar, *Membrane handbook*. 1992, New York: Van Nostrand Reinhold.
5. Kesting, R.E. and F. A.K., *Polymeric gas separation*. 1993, New York: Wiley.
6. Cornelius, C.J. and E. Marand, Polymer, 2002. **43**(8): p. 2385-2400.
7. Cornelius, C.J. and E. Marand, J. Membr. Sci., 2002. **202**(1-2): p. 97-118.

8. Kim, J.H., W.J. Koros, and D.R. Paul, *Polymer*, 2006. **47**(9): p. 3094-3103.
9. Mahajan, R., R. Burns, M. Schaeffer, and W.J. Koros, *J. Appl. Polym. Sci.*, 2002. **86**(4): p. 881-890.
10. Mahajan, R. and W.J. Koros, *Polym. Eng. Sci.*, 2002. **42**(7): p. 1420-1431.
11. Mahajan, R. and W.J. Koros, *Polym. Eng. Sci.*, 2002. **42**(7): p. 1432-1441.
12. Robeson, L.M., *J. Membr. Sci.*, 1991. **62**(2): p. 165-185.
13. Anson, M., J. Marchese, E. Garis, N. Ochoa, and C. Pagliero, *J. Membr. Sci.*, 2004. **243**(1-2): p. 19-28.
14. Tin, P.S., T.S. Chung, L.Y. Jiang, and S. Kulprathipanja, *Carbon*, 2005. **43**(9): p. 2025-2027.
15. Yong, H.H., N.C. Park, Y.S. Kang, J. Won, and W.N. Kim, *J. Membr. Sci.*, 2001. **188**(2): p. 151-163.
16. Pechar, T.W., M. Tsapatsis, E. Marand, and R. Davis, *Desalination*, 2002. **146**(1-3): p. 3-9.
17. Mahajan, R. and W.J. Koros, *Ind. Eng. Chem. Res.*, 2000. **39**(8): p. 2692-2696.
18. Liu, J.Q., T.H. Bae, W.L. Qiu, S. Husain, S. Nair, C.W. Jones, R.R. Chance, and W.J. Koros, *J. Membr. Sci.*, 2009. **343**(1-2): p. 157-163.
19. Bae, T.H., J.Q. Liu, J.S. Lee, W.J. Koros, C.W. Jones, and S. Nair, *J. Am. Chem. Soc.*, 2009. **131**(41): p. 14662-14663.
20. Husain, S. and W.J. Koros, *J. Membr. Sci.*, 2007. **288**(1-2): p. 195-207.
21. Jiang, L.Y., T.S. Chung, C. Cao, Z. Huang, and S. Kulprathipanja, *J. Membr. Sci.*, 2005. **252**(1-2): p. 89-100.

22. Jiang, L.Y., T.S. Chung, and S. Kulprathipanja, *AIChE J.*, 2006. **52**(8): p. 2898-2908.
23. Shu, S., S. Husain, and W.J. Koros, *J. Phys. Chem. C*, 2007. **111**(2): p. 652-657.
24. Lee, J.H., B.J.R. Thio, T.H. Bae, and J.C. Meredith, *Langmuir*, 2009. **25**(16): p. 9101-9107.
25. Vankelecom, I.F.J., S. VandenBroeck, E. Merckx, H. Geerts, P. Grobet, and J.B. Uytterhoeven, *J. Phys. Chem.*, 1996. **100**(9): p. 3753-3758.
26. Diaz, U., J.A. Vidal-Moya, and A. Corma, *Microporous Mesoporous Mater.*, 2006. **93**(1-3): p. 180-189.
27. Jones, C.W., K. Tsuji, and M.E. Davis, *Nature*, 1998. **393**(6680): p. 52-54.
28. Feldman, K., T. Tervoort, P. Smith, and N.D. Spencer, *Langmuir*, 1998. **14**(2): p. 372-378.
29. Eroshenko, V., R.C. Regis, M. Soulard, and J. Patarin, *J. Am. Chem. Soc.*, 2001. **123**(33): p. 8129-8130.
30. Desbiens, N., I. Demachy, A.H. Fuchs, H. Kirsch-Rodeschini, M. Soulard, and J. Patarin, *Angew. Chem. Int. Ed.*, 2005. **44**(33): p. 5310-5313.
31. Diaz, I., E. Kokkoli, O. Terasaki, and M. Tsapatsis, *Chem. Mater.*, 2004. **16**(25): p. 5226-5232.
32. Agger, J.R., N. Hanif, C.S. Cundy, A.P. Wade, S. Dennison, P.A. Rawlinson, and M.W. Anderson, *J. Am. Chem. Soc.*, 2003. **125**(3): p. 830-839.
33. Singh, A. and W.J. Koros, *Ind. Eng. Chem. Res.*, 1996. **35**(4): p. 1231-1234.
34. Li, Y., H.M. Guan, T.S. Chung, and S. Kulprathipanja, *J. Membr. Sci.*, 2006. **275**(1-2): p. 17-28.
35. Butt, H.H. and R. Stark, *Colloids Surf. A*, 2005. **252**(2-3): p. 165-168.

36. Cappella, B. and G. Dietler, *Surf. Sci. Rep.*, 1999. **34**(1-3): p. 1-104.
37. Ducker, W.A., T.J. Senden, and R.M. Pashley, *Langmuir*, 1992. **8**(7): p. 1831-1836.
38. Ducker, W.A., Z.G. Xu, and J.N. Israelachvili, *Langmuir*, 1994. **10**(9): p. 3279-3289.
39. Parker, J.L. and P.M. Claesson, *Langmuir*, 1994. **10**(3): p. 635-639.
40. Rabinovich, Y.I., B.V. Derjaguin, and N.V. Churaev, *Adv. Colloid Interface Sci.*, 1982. **16**(Jul): p. 63-78.
41. Meyer, E.E., Q. Lin, T. Hassenkam, E. Oroudjev, and J.N. Israelachvili, *Proc. Natl. Acad. Sci. USA*, 2005. **102**(19): p. 6839-6842.
42. Meyer, E.E., K.J. Rosenberg, and J. Israelachvili, *Proc. Natl. Acad. Sci. USA*, 2006. **103**(43): p. 15739-15746.
43. Mizukami, M., M. Moteki, and K. Kurihara, *J. Am. Chem. Soc.*, 2002. **124**(43): p. 12889-12897.
44. Mizukami, M., Y. Nakagawa, and K. Kurihara, *Langmuir*, 2005. **21**(21): p. 9402-9405.
45. Nguyen, A.V., J. Nalaskowski, J.D. Miller, and H.J. Butt, *Int. J. Mineral Proc.*, 2003. **72**(1-4): p. 215-225.
46. Thio, B.J.R. and J.C. Meredith, *J. Colloid Interface Sci.*, 2007. **314**(1): p. 52-62.
47. Brewer, N.J. and G.J. Leggett, *Langmuir*, 2004. **20**(10): p. 4109-4115.
48. Headrick, J.E. and C.L. Berrie, *Langmuir*, 2004. **20**(10): p. 4124-4131.
49. Ito, T., M. Namba, P. Buhlmann, and Y. Umezawa, *Langmuir*, 1997. **13**(16): p. 4323-4332.



50. Drelich, J., G.W. Tormoen, and E.R. Beach, J. Colloid Interface Sci., 2004. **280**(2): p. 484-497.
51. Nalaskowski, J., J. Drelich, J. Hupka, and J.D. Miller, Langmuir, 2003. **19**(13): p. 5311-5317.
52. Nalaskowski, J., S. Veeramasuneni, J. Hupka, and J.D. Miller, J. Adhes. Sci. Technol., 1999. **13**(12): p. 1519-1533.
53. Thio, B.J.R., J.H. Lee, and J.C. Meredith, Environ. Sci. Technol., 2009. **43**(12): p. 4308-4313.
54. Toikka, G., R.A. Hayes, and J. Ralston, J. Colloid Interface Sci., 1996. **180**(2): p. 329-338.
55. Amanuel, S., A.N. Gaudette, and S.S. Sternstein, J. Polym. Sci., Part B: Polym. Phys., 2008. **46**(24): p. 2733-2740.
56. Arrighi, V., I.J. McEwen, H. Qian, and M.B.S. Prieto, Polymer, 2003. **44**(20): p. 6259-6266.
57. Ash, B.J., D.F. Rogers, C.J. Wiegand, L.S. Schadler, R.W. Siegel, B.C. Benicewicz, and T. Apple, Polym. Compos., 2002. **23**(6): p. 1014-1025.
58. Ash, B.J., R.W. Siegel, and L.S. Schadler, J. Polym. Sci., Part B: Polym. Phys., 2004. **42**(23): p. 4371-4383.
59. Fu, S.Y., X.Q. Feng, B. Lauke, and Y.W. Mai, Composites Part B, 2008. **39**(6): p. 933-961.
60. Metin, D., F. Tihminhoglu, D. Balkose, and S. Ulku, Composites Part A, 2004. **35**(1): p. 23-32.
61. Musto, P., G. Ragosta, G. Scarinzi, and L. Mascia, Polymer, 2004. **45**(5): p. 1697-1706.
62. Xie, X.L., C.Y. Tang, X.P. Zhou, R.K.Y. Li, Z.Z. Yu, Q.X. Zhang, and Y.W. Mai, Chem. Mater., 2004. **16**(1): p. 133-138.

- 63. Salehi-Khojin, A., S. Jana, and W.H.K. Zhong, J. Mater. Sci., 2007. **42**(15): p. 6093-6101.
- 64. Tsagaropoulos, G. and A. Eisenberg, Macromolecules, 1995. **28**(1): p. 396-398.
- 65. Zidan, H.M., J. Polym. Sci., Part B: Polym. Phys., 2003. **41**(1): p. 112-119.
- 66. Sormana, J.L., S. Chattopadhyay, and J.C. Meredith, J. Nanomater., 2008. **2008**(1): p. 1-9.
- 67. Sormana, J.L. and J.C. Meredith, Macromol. Rapid Commun., 2003. **24**(1): p. 118-122.
- 68. Sormana, J.L. and J.C. Meredith, Mater. Res. Innov., 2003. **7**(5): p. 295-301.
- 69. Sormana, J.L. and J.C. Meredith, Macromolecules, 2004. **37**(6): p. 2186-2195.

# CHAPTER 3

## ZEOLITE-POLYMER INTERFACIAL ADHESION

### MEASUREMENT

#### 3.1. OVERVIEW

Adhesion between zeolites and polymers is a central factor in achieving defect-free mixed-matrix membranes for energy-efficient gas separations [1-5]. In this chapter, atomic force microscopy (AFM) was used to measure adhesion forces between a pure-silica MFI zeolite microcrystal (010) surface (bare, and silanated and Grignard treated) and a series of polyimide (Matrimid<sup>®</sup> 5218, 6FDA-DAM, 6FDA-6FpDA, and 6FDA-DAM:DABA (3:2)), polyetherimide (Ultem 1000), and polyvinyl acetate (PVAc) polymers in air. To our knowledge, measurements of adhesion force between a non-spherical zeolite particle and polymers using the colloidal probe method have not been reported prior to this work.

We also measured contact angles of three diverse liquids on the polymers and used these to calculate surface energy with van Oss and Good's Lifshitz van der Waals acid-base theory. Combined with measurements of surface energy of the polymer surfaces, the dependence of adhesion on polymer structure was determined. Adhesion force of the bare MFI particle to polymer surfaces was strongly dependent on the Lewis basicity component of polymer surface energy and was less dependent on van der Waals components, by a factor of about 6. Hydrogen bonding likely occurs between the acidic (electron acceptor) component of the zeolite surface (silanols or adsorbed water) and the basic (electron donor) component of the polymer surface. Adhesion forces between the bare MFI surface and the polymer surfaces were strongly correlated with the mole fraction of carbonyls per monomer. It was concluded that differences in adhesion as a

function of polymer structure were primarily controlled by the polymer's Lewis basicity, contributed primarily by carbonyl groups.

Surface modification on the MFI zeolite by ether silanation or Grignard treatment increased adhesion force of the zeolite with polymers. In particular, adhesive force of Grignard treated MFI to the polymers was higher than that of bare MFI around by twice.

### 3.2. THEORY

The work of adhesion ( $W_{SL}$ ) for a liquid and a solid in contact is defined by the negative of the Gibbs free energy change per unit area ( $\Delta G$ ) of interfaces, and it expressed by the Young-Dupré equation.

$$W_{SL} = -\Delta G = \gamma_L + \gamma_S - \gamma_{SL} \quad (3.1)$$

Where  $\gamma_L$ ,  $\gamma_S$ , and  $\gamma_{SL}$  describe the surface tensions of liquid, solid, and liquid-solid interface, respectively. To analyze the surface energy of polymer surfaces, van Oss and Good's Lifshitz-van der Waals Acid-Base theory (three-liquid acid-base method) is used [6]. According to this theory, together with van der Waals ( $\gamma^{vW}$ ) contribution, an acid ( $\gamma^+$ , electron acceptor)-base ( $\gamma^-$ , electron donor) contribution is involved in the work of adhesion, which is associated with the transfer of electron density between an electron donor and an electron acceptor, e.g., hydrogen bonding. If both terms, donor and acceptor, are negligible, the material is considered apolar; if only one of the components is negligible, the substance is monopolar and it is bipolar if both components have to be considered. For the total work of adhesion at the solid (S)-liquid (L) interface, the sum of the van der Waals and the acid-base contributions is given by

$$W_{SL} = 2(\gamma_S^{vW} \cdot \gamma_L^{vW})^{1/2} + 2(\gamma_S^+ \cdot \gamma_L^-)^{1/2} + 2(\gamma_S^- \cdot \gamma_L^+)^{1/2} \quad (3.2)$$

Using this definition for the work of adhesion in the Young-Dupré equation and combining with Young's equation, we obtain

$$\gamma_L(1 + \cos \theta) = 2(\gamma_S^{vW} \cdot \gamma_L^{vW})^{1/2} + 2(\gamma_S^+ \cdot \gamma_L^-)^{1/2} + 2(\gamma_S^- \cdot \gamma_L^+)^{1/2} \quad (3.3)$$

where  $\theta$  is the contact angle. Equation 3.3 allows the determination of the van der Waals and acid-base components of the surface energy of a solid surface from contact angle measurements with three testing liquids with known values of the surface tension components. The three testing liquids for determining surface tension components from contact angle data followed these criteria: one of the liquids was apolar (diiodomethane) van der Waals type, and two others were bipolar (deionized water and glycerol) [7]. The liquids used in the present work are a generally accepted combination [7-9].

### 3.3. EXPERIMENTAL

#### 3.3.1. Materials and Procedure

##### 3.3.1.1. Materials

##### 3.3.1.1.1. Polymers

Polystyrene (PS, 100,000 g/mol, Avocado Research Chemicals, England), PVAc (500,000 g/mol, Aldrich), Matrimid<sup>®</sup> 5218 (Vantico), and Ultem<sup>®</sup> 1000 (GE Plastics) were used as received. 2,2-bis(3,4-carboxyphenyl)hexafluoropropane dianhydride (6FDA, Lancaster) based copolyimides were prepared by two-step polycondensation of an equimolar mixture of this dianhydride and a diamine followed by a cyclodehydration reaction [10-12]. The diamines (Aldrich) used to form 6FDA based copolyimides were (4,4'-hexafluoroisopropylidene)diamine (6FpDA), and diaminomesitylene (DAM) respectively. One of the 6FDA based copolyimides was formed by replacing a portion of the diamine of 6FDA-DAM with 3,5-diaminobenzoic acid (DABA), following the procedure described in the literature [10-12].

### 3.3.1.1.2. Zeolites (MFI)

**Bare MFI:** The procedure published by Agger et al.[13] was used to synthesize pure-silica MFI particles. 41 g of tetraethylorthosilicate (TEOS, Acros 98%) was added to a solution of 5.42 g of tetrapropylammonium (TPA) bromide (Aldrich, 98%) and 0.8 g of sodium hydroxide (Aldrich, 97+%) in 354 g of deionized water in a polypropylene container. The mixture was stirred vigorously at room temperature for 24 h until it became completely transparent. The molar ratio of the resulting mixture was 1 TEOS:0.1 TPABr:0.1 NaOH:98 H<sub>2</sub>O. The mixture was then aged in an oven at 50 °C for 7 days and then transferred to a 700 mL autoclave reactor (HR-700, Berghof, Inc.) to perform the hydrothermal reaction at 120 °C. After a 48 h synthesis, the resulting suspension was centrifuged at 1000 rpm for 10 min and the supernatant was discarded. The solid was redispersed into deionized water by sonication and was centrifuged afterward. This centrifugation-sonication cycle was repeated 5 times. After the purification step, MFI particles were dried at room temperature and then calcinated at 550 °C for 8 h.

**APDEMS treatment:** MFI zeolites were chemically modified by APDMES ( $\gamma$ -aminopropyldimethylethoxy silane) treatment [5]. 10 g of zeolites were dried overnight in a vacuum oven at 120 °C. The dried zeolites were added to 200 ml of a 95:5 vol.% solution of 2-propanol and deionized water. The mixture was sonicated at 50 kHz for 30 min to disperse the zeolite to disperse the zeolites. After adding 5.0 ml of fresh APDMES, the mixture was sonicated at 42 kHz for 30 min, and stirred by a rotating shaker for 12 h. The resulting suspension was washed with 2-propanol by at least 5 cycles of centrifugation. After the purification step, the silanated MFI particles were dried in a vacuum oven at 140 °C for 12 h.

**Grignard treatment:** Grignard treatment was performed after seeding the zeolite surfaces with NaCl. 0.5 g of MFI particles was dispersed in 3 M aqueous NaCl solution [14]. The suspension was filtered using a microfiltration membrane with 0.1  $\mu$ m pores. The

collected particles were then dried at 80 °C for 12 h to remove some of the residual water. The NaCl seeded particles were placed in round bottom flask, followed by the addition of 8 ml of toluene. After purging the flask with nitrogen 1.5 ml of 3 M CH<sub>3</sub>MgBr in ether was added using transfer needles. The suspension was sonicated at 20 kHz for 4 h and then stirred at room temperature under nitrogen for 12 h. 2-propanol was added dropwise to quench the Grignard reagent and the mixture was centrifuged to collect the particles. To remove residual solvents, the particles were washed with 2-propanol several times. After that, 40 ml of DI water was added to the particles and the mixture was sonicated at 20 kHz for 2 h. The particles were washed with DI water via several cycles of centrifugation and dispersion, followed by drying at 80 °C.

### ***3.2.1.2. Sample Preparation***

#### ***3.3.1.2.1. Substrates***

A series of thin polymer films was prepared on Piranha-etched (20/80 vol.% H<sub>2</sub>O<sub>2</sub>/H<sub>2</sub>SO<sub>4</sub> at 80 °C for 1 h) silicon substrate. The Ultem<sup>®</sup> 1000 solution was prepared by dissolving 6 % by mass in dichloromethane, while 5 % by mass PS, PVAc, Matrimid<sup>®</sup> 5218, 6FDA-DAM, 6FDA-6FpDA, and 6FDA-DAM:DABA (3:2) solutions were prepared in tetrahydrofuran. Polymer films were made by a knife-edge coating method, described in detail elsewhere [15-17]. Polymer films were dried at room temperature for 24 h after coating and then dried again under vacuum for at least 12 h (PVAc at 20 °C for 48 h and other polymers at 60 °C for 12 h) to remove the residual solvent. After that, they were transferred to a desiccator and stored prior to measurements. The root-mean-square surface roughness (*rms*) for the polymer films was  $1.20 \pm 0.26$  nm, obtained from topography of 10 x 10 μm<sup>2</sup> areas using a scanning probe microscope (PicoScan 5, Molecular Imaging). Film thickness was measured from scanning electron microscopy (SEM) cross-sectional images. Thicknesses of the polymers ranged from 10 to 24 μm, which far exceed the range of van der Waals interactions (~ 20 nm) of the substrate.

### 3.3.1.2.2. Zeolite Colloidal Probes

The zeolite colloidal probe was prepared by attaching a single zeolite microcrystal (bare, aminosilane and Grignard treated) to the apex of a tipless cantilever (ACL-TL, Applied NanoStructures, Inc.) using epoxy glue. To control the amount of glue and avoid contaminating the front face of the zeolite crystal, the amount of glue was minimized by repeatedly blotting the cantilever (under closed-loop AFM control) on a silicon wafer. The glue-coated probe was moved onto the zeolite microcrystal only after the amount of glue was estimated small enough to avoid contamination of the microcrystal (later verified by Scanning electron microscopy (SEM) inspection). In order to minimize orientation problems, the position of the zeolite microcrystal on a cantilever was observed under optical microscopy. A schematic of colloidal probe fabrication is shown in Figure 3.1.

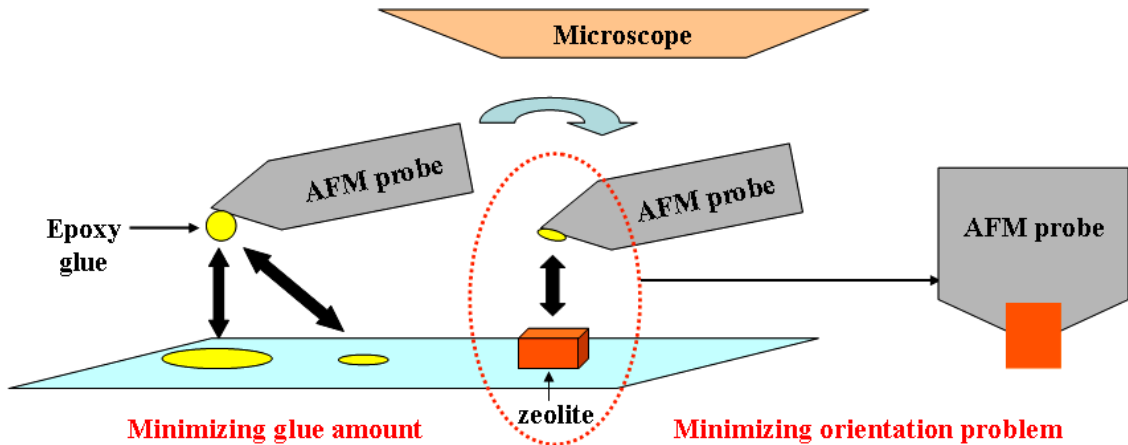


Figure 3.1: Schematic of zeolite colloidal probe fabrication.

The gluing was completed by curing and drying at room temperature for 24 h. After all adhesion pull-off measurements were finished, the zeolite probe's surface morphology was inspected by AFM, operated in tapping mode with a sharp tip (ACTA, Applied NanoStructures, Inc.). The surface roughness (*rms*) and arithmetic average height, evaluated on areas of  $2.5 \times 2.5 \mu\text{m}^2$  from bare zeolite microcrystal (010) surface,



were  $\sim 7.3$  nm and  $\sim 5.9$  nm, respectively. The bare MFI (010) surface has the typical terrace structure with step height  $\sim 1$  nm [13, 18], shown in Figure 3.2.

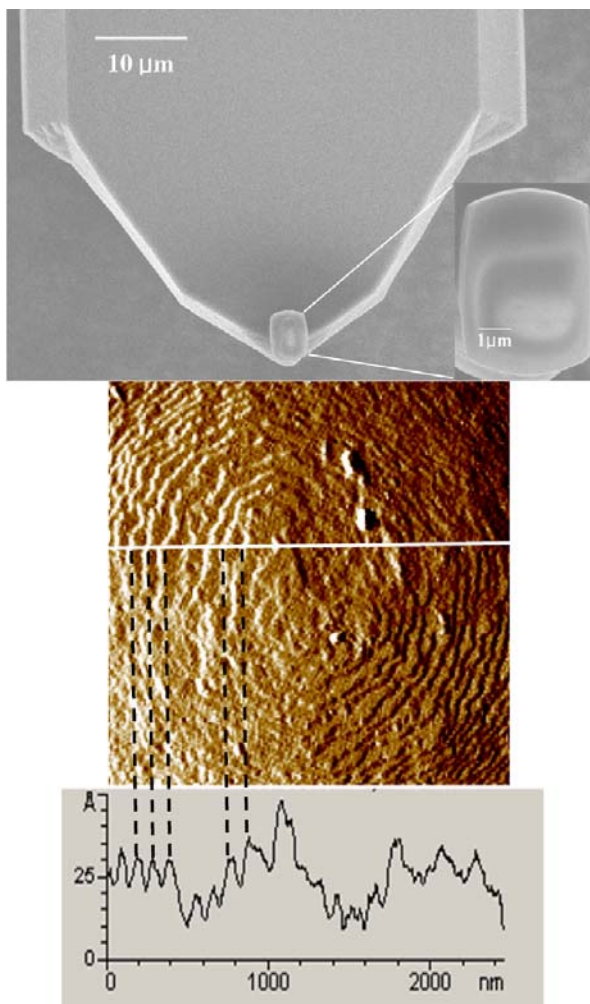


Figure 3.2: (Top) SEM image of a pure-silica MFI zeolite colloidal probe (top), (middle) AFM phase image of the (010) surface of zeolite microcrystal ( $2.5 \times 2.5 \mu\text{m}^2$ ), and (bottom) cross-sectional height profile.

The cantilever spring constant was measured by using the technique of Cleveland et al. [19], and the contact area of the zeolite microcrystal was estimated from SEM image. The values of spring constant and zeolite contact area of each probe (bare, APDMES and Grignard treated) are summarized in Table 3.1.

Table 3.1: The values of spring constant and contact area of zeolite colloidal probes.

Zeolite	Spring constant (N/m)	Contact area ( $\mu\text{m}^2$ )
Bare	68.57	20.37
APDMES	64.56	20.23
Grignard	75.96	17.25

### 3.3.2. Experimental Methods

#### 3.3.2.1. AFM Force Measurements

AFM force-distance measurements between the zeolite colloidal probe and diverse polymer surfaces were performed using a scanning probe microscope (PicoScan 5, Molecular Imaging) at 20 °C in a glove box chamber with room condition humidity (relative humidity,  $RH$ ,  $\sim 35\%$ ). This  $RH$  was chosen because zeolite-filled membranes are prepared in the open laboratory usually, and because  $RH$  control experiments (discussed in Results and Discussion section) indicated the absence of capillary condensation. To investigate the effects of humidity, hydrophilic PVAc and hydrophobic PS were used as controls and their adhesion forces with MFI zeolite were measured at different humidity conditions ( $RH = 20\%$ ,  $35\%$ , and  $75\%$ ).

Prior to the measurements, each zeolite colloidal probe was successively washed with ethanol, acetone, and deionized water, and then used to measure adhesion forces with a given polymer series. Forces applied to a probe during the measurement were kept constant at  $5.7 \times 10^3$  nN. For each set of zeolite-polymer measurements, cantilever deflection due to zeolite-polymer adhesion was determined from the average well depth of at least 30 force-displacement curves (retraction portion) at randomly chosen points within  $100 \times 100 \mu\text{m}^2$  areas on each polymer film surface. Error bars and uncertainties were calculated as 99% confidence intervals. The deflection values were converted to forces by multiplying by the spring constant of the cantilever. Typical force-

displacement curves of one bare probe and one zeolite colloidal probe are shown in Figure 3.3.

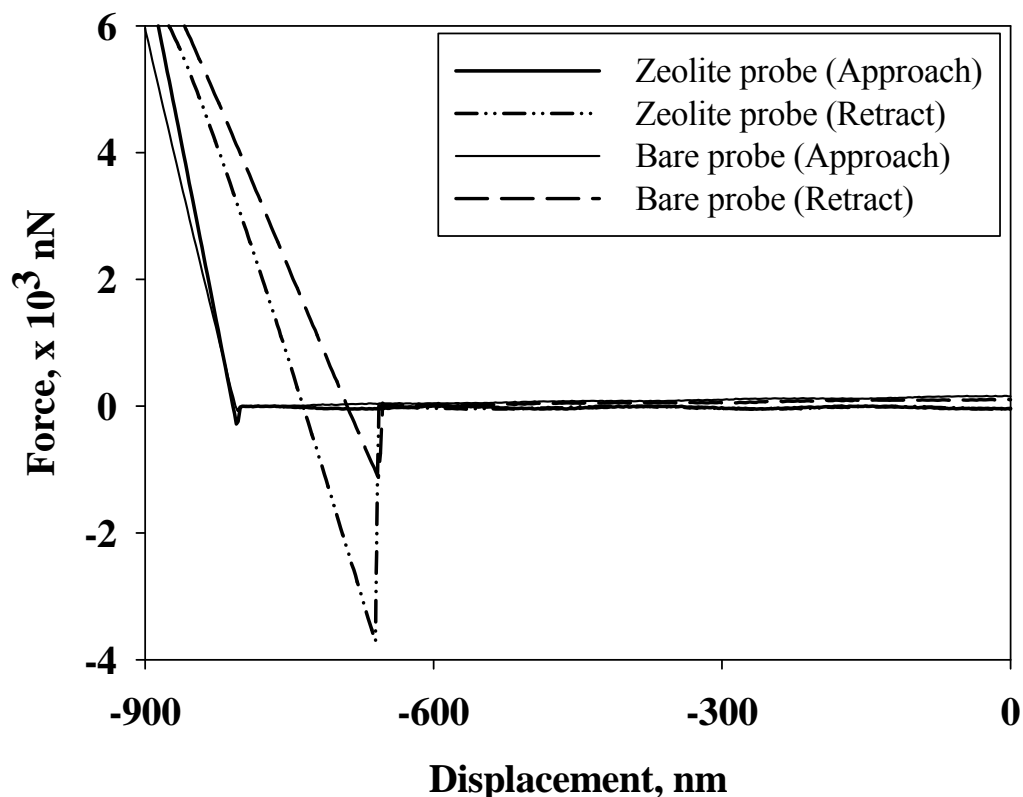


Figure 3.3: Typical force-displacement curves between the zeolite colloidal probe or bare probe and PVAc polymer surface.

Contact area during force measurements should be considered carefully because the cantilever is held at an angle of  $9^\circ$  relative to the sample surface. For a concentrated load ( $F$ ) exerted on the end of the rectangular cantilever with length  $L$ , width  $W$ , thickness  $t$ , and Young's modulus  $E$ , the maximum deflection angle ( $\theta_F$ ) at the free end of the cantilever [20] is given by

$$\theta_F = \frac{6FL^2}{EWt^3} \quad (3.4)$$

Using the cantilever geometry given by the manufacturer, and assuming its Young's modulus is that of bulk Si,  $\sim 195$  GPa [21], the cantilever deflection angle of

0.034° was estimated. This means that full contact of the attached zeolite with the surfaces cannot be achieved. However, measured adhesion values can be used for relative comparisons, because all force measurement were carried out under constant load.

In studies of soft materials, one should be aware of the potential for differences in sample deformation during loading, which could introduce differences in contact area. All polymers in this study are very glassy and rigid except PVAc. The elastic moduli of the glassy polymers are similar: PS (3000 - 3600 MPa), polyimides (3200 MPa), and polyetherimide (Ultem, 3275 MPa). The PVAc elastic modulus is lower, 1100 - 1600 MPa. We do not expect any significant difference in contact area in the case of glassy polymers, but contact area with PVAc could be different from that with the glassy polymers. This fact will be considered in our interpretation of force data below. To check directly for sample compliance effects on the pull-off force, load dependent experiments were carried out in range of  $1.0 - 9.0 \times 10^3$  nN for the polymer in this study. No significant load dependence (within 3 – 5 % from median) was observed over the investigated range.

### ***3.3.2.2. Contact Angle Measurements***

The contact angles of polymer surfaces with diverse testing liquids were measured at 20 °C by the sessile drop method using a video capture apparatus (VCA2500XE, AST Products, Inc.). Deionized water, glycerol (Alfa Aesar > 99%), and diiodomethane (Alfa Aesar > 99%) were chosen as the testing liquids. At least five droplets at different regions of the same piece of film were dispensed for contact angle measurements, and at least two pieces of film were used to get reliable contact angle data. Thus, the contact angle values are averages of results obtained from a set of at least 10 experiments.

### 3.4. RESULTS AND DISCUSSION

#### 3.4.1. Analysis of Polymer Surface Energy

The surface tensions of the testing liquids [22, 23] and their contact angles with a series of polymer surfaces are given in Table 3.2 and Table 3.3, respectively.

Table 3.2: Surface tension components (mJ/m<sup>2</sup>) of testing liquids [22, 23].

Surface tension component	Water	Glycerol	Diiodomethane
$\gamma^+$	25.5	3.92	0.0
$\gamma^-$	25.5	57.4	0.0
$\gamma^{vW}$	21.8	34.0	50.8
$\Gamma$	72.8	64.0	50.8

Where,  $\gamma = \gamma^{vW} + (\gamma^- \cdot \gamma^+)^{1/2}$

Table 3.3: Contact angle (°) of polymer surfaces with testing liquids.

Polymer	DI water	Glycerol	Diiodomethane
PVAc	59.3 ± 0.3	70.2 ± 0.5	38.7 ± 0.3
Matrimid <sup>®</sup> 5218	72.5 ± 0.3	67.3 ± 0.8	24.0 ± 0.3
6FDA-DAM:DABA (3:2)	73.8 ± 0.4	73.1 ± 0.2	41.1 ± 1.0
6FDA-DAM	76.5 ± 0.2	69.2 ± 0.6	37.0 ± 0.5
6FDA-6FpDA	86.9 ± 1.1	76.5 ± 0.2	46.8 ± 0.8
Ultem <sup>®</sup> 1000	88.4 ± 0.3	74.2 ± 0.6	20.7 ± 1.1
PS	98.5 ± 1.5	83.4 ± 0.4	33.1 ± 0.3

*Note.* Uncertainty is ± 99% confidence interval.

Table 3.4 shows the calculated surface energy components of the polymer films using the three-equation method. The term  $\gamma^{wW}$  indicates the van der Waals (VDW) component, while  $\gamma^+$  and  $\gamma^-$  refer to the acid and base components, respectively.

Table 3.4: Surface tension components (mJ/m<sup>2</sup>) of polymer film surfaces.

Polymer	$\gamma^-$	$\gamma^+$	$\gamma^{wW}$	$\gamma$
PVAc	33.1	0.54	40.3	48.7
Matrimid <sup>®</sup> 5218	11.1	0.07	46.5	48.3
6FDA-DAM:DABA (3:2)	14.4	0.12	39.1	41.7
6FDA-DAM	8.66	0.00	41.1	41.1
6FDA-6FpDA	3.90	0.01	36.0	36.4
Ultem <sup>®</sup> 1000	1.71	0.08	47.6	48.3
PS	0.33	0.23	42.9	43.4

From Table 3.4, it can be concluded that PVAc has a large Lewis basic component, while the other polymer films have smaller electron donor-acceptor terms. In addition, PS is essentially apolar, while polyimide (Matrimid<sup>®</sup> 5218 and 6FDA based copolyimides), polyetherimide (Ultem<sup>®</sup> 1000), and PVAc have monopolar Lewis base (electron donor) characteristics, because their  $\gamma^+$  values are negligible. (PS is included because it contains aromatic groups and is glassy, but lacks the carbonyl moieties present in the polyimides.) This result is consistent with their molecular structure: lone electron pairs are provided by carbonyl, ether, and/or carboxyl groups in the polyimide, polyetherimide, and PVAc. Comparing our results to data in the literature we find that the experimental surface tension and VDW component values are within 10 and 5 %, respectively: (PS [24]:  $\gamma^{wW} = 42.0$ ,  $\gamma^+ = \sim 0$ ,  $\gamma^- = 1.1$ , and  $\gamma = 42.66$ ; PVAc [25]:  $\gamma^{wW} = 42.6$ ,  $\gamma^+ = \sim 0.041$ ,  $\gamma^- = 22.3$ , and  $\gamma = 44.5$ , Ultem [26]:  $\gamma^d = 46.7$ ,  $\gamma^p = 0.15$ , and  $\gamma = 46.85$ )

Experimental and literature values are also qualitatively consistent: basicity of PVAc is much higher than acidity, PS has very weak basicity, and Ultem has a small polar component.

### 3.4.2 MFI Zeolite-Polymer Adhesion Measurement in Air

#### 3.4.2.1. Bare MFI-Polymer Adhesion in Air

Table 3.5 shows the adhesion forces between pure-silica MFI zeolite and the diverse polymer surfaces. PS, the most apolar in the series, showed the lowest adhesive force value, while PVAc, 6FDA-DAM-DABA, Matrimid<sup>®</sup> 5218, with higher Lewis basic components, had higher adhesion forces. This observation suggests that Lewis basic components of the polymer surfaces play the dominant role in adhesion with the MFI zeolite surface.

Table 3.5: AFM adhesion force ( $F_{ad}$ ) between a bare MFI zeolite and polymer surfaces.

Polymer	$F_{ad}$ (x $10^3$ nN)
PVAc	$4.28 \pm 0.14$
Matrimid <sup>®</sup> 5218	$4.38 \pm 0.11$
6FDA-DAM:DABA (3:2)	$4.00 \pm 0.10$
6FDA-DAM	$3.92 \pm 0.11$
6FDA-6FpDA	$3.64 \pm 0.08$
Ultem <sup>®</sup> 1000	$3.35 \pm 0.10$
PS	$2.97 \pm 0.06$

*Note.* Uncertainty is  $\pm$  99% confidence interval.

AFM adhesion forces were correlated with the surface energies and molecular structures of the polymers. The work of adhesion ( $W_{ZP}$ ) based on van Oss and Good's Lifshitz-van der Waals acid-base theory is assumed to be applicable to the solid (zeolite

surface, z)-solid (a polymer surface, p) interface. The adhesion force between pure-silica MFI and polymer surfaces ( $F_{ZP}$ ) is proportional to  $W_{ZP}$  and can be expressed by terms to contain only van der Waals and acidic (zeolite,  $\gamma_Z^+$ )-basic (polymer,  $\gamma_P^-$ ):

$$F_{ZP} \propto W_{ZP} = 2(\gamma_Z^{vw} \cdot \gamma_P^{vw})^{1/2} + 2(\gamma_Z^+ \cdot \gamma_P^-)^{1/2} \quad (3.5)$$

The surface energy components of the zeolite surface can be considered constant, as a single zeolite colloidal probe was used for measuring all adhesion forces between the zeolite and polymer surfaces. Since the  $\gamma_P^+$  values of the polymer films used in this study are negligible, the adhesive forces therefore depend on the van der Waals ( $\gamma_P^{vw}$ ) and Lewis basicity ( $\gamma_P^-$ ) contribution of the polymer surfaces. We fitted to the equation  $F = a^-(\gamma^-)^{1/2} + a^{vw}(\gamma^{vw})^{1/2}$ , which is a plane, and this planar fit is plotted along with the adhesion forces ( $F_{ZP}$ ) in Figure 3.4.

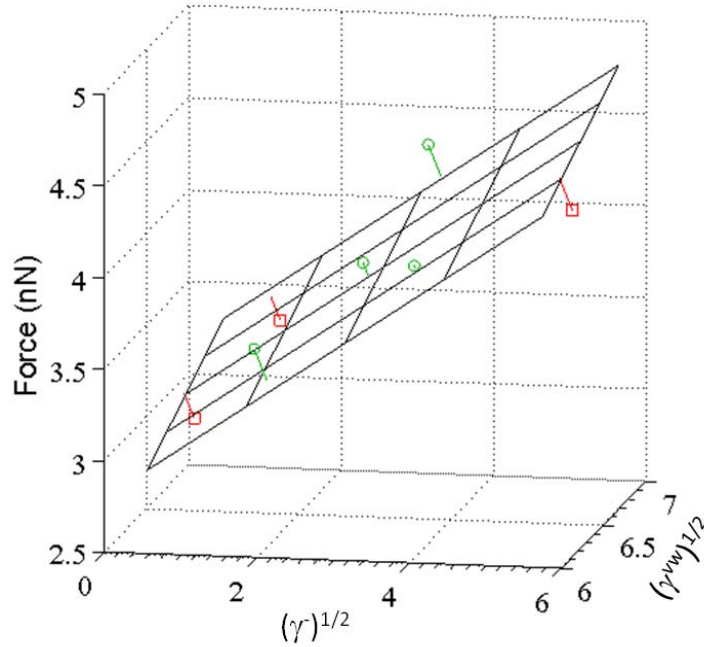


Figure 3.4: Fitting of a planar model of equation 3.5 to force data. Circles are above the plane, squares are below the plane and lines from data points to the plane indicate fitting errors.



Table 3.6 provides the coefficients and correlation coefficient ( $r^2$ ) resulting from fitting to the planar model. Fitting all seven polymers lead to a low correlation coefficient  $r^2$  (bottom row of table), and PVAc was found to result in the largest fitting error. Because there are other reasons to suspect PVAc values, namely the lack of aromatic groups and its low glass transition temperature, we omitted PVAc for subsequent fitting. Fitting the raw data values (dimensional) lead to a good fit ( $r^2 = 0.88$ ) and suggested the effects of basicity and VDW components were equal,  $\bar{a}/a^{vw} = 0.94$ . However, the VDW components are largest but do not vary over a wide range ( $6 < (\gamma^{vw})^{1/2} < 6.9$ ) while the basicity components are smaller but vary over a large range ( $0.57 < (\gamma^-)^{1/2} < 5.75$ ). To gauge the contributions of each component the range and magnitude effects should be removed. This is often accomplished in linear modeling by rescaling the data from -1 to 1 where -1 represents the minimum value and +1 represents the maximum value. In the scaled case, as shown in Table 3.6, the basicity coefficient is significantly larger than the VDW component,  $\bar{a}/a^{vw} = 6.2$ . Furthermore, when PVAc is added back in, this ratio does not change, even though the regression error increases ( $r^2$  drops to 0.6). Therefore, it can be concluded that the basicity of the polymer surfaces determines the change in adhesion force as a function of the polymer.

Table 3.6: Fitting parameters (coefficients and correlation coefficient).

Data Fitted	$\bar{a}$	$a^{vw}$	$r^2$	$\bar{a}/a^{vw}$
raw (minus PVAc)	0.40	0.43	0.88	0.94
scaled -1:1 (minus PVAc)	0.88	0.14	0.89	6.1
scaled -1:1 (all data)	0.89	0.14	0.6	6.2

Carbonyl groups in the polymers act as the major electron-donor component and are able to form hydrogen bonds with native silanols or adsorbed water on the zeolite

[27]. Figure 3.5 supports this idea by plotting the carbonyl group mole fraction (the ratio of the number of carbonyls to total carbon atoms in each monomer) versus  $(\gamma_P^-)^{1/2}$ . The square root of  $\gamma_P^-$  is plotted as it is proportional to the adhesion force in the model adopted in equation 3.5. As Figure 3.5 shows, the polymer's basicity is strongly correlated with its carbonyl group mole fraction. Silanol groups on the zeolite surface likely form hydrogen bonds with lone pairs from oxygen atoms on the polymers (except for PS) [28-31]. As hydrogen bonding energies are (10 - 40 KJ mol<sup>-1</sup>) much stronger than van der Waals interaction energies ( $\sim 1$  KJ mol<sup>-1</sup>) [32], even a low density of hydrogen bonding between the zeolite and polymer surfaces can have a dominant effect on adhesion forces.

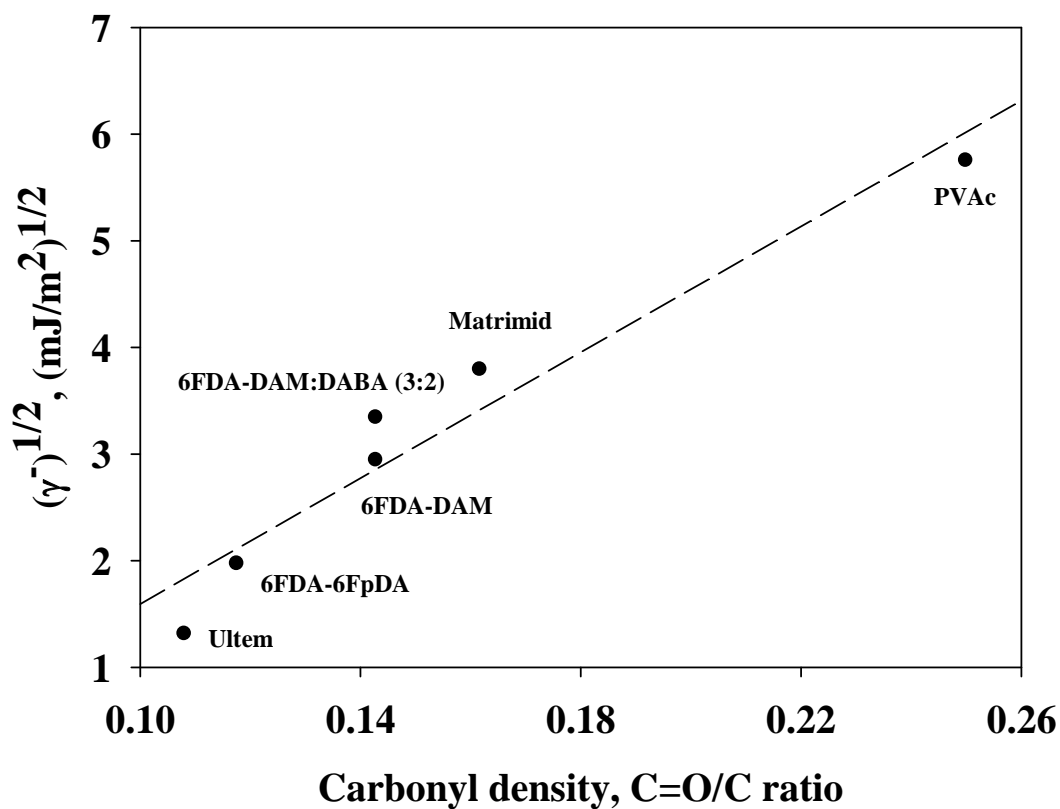


Figure 3.5: Carbonyl fraction of polymers versus the Lewis basicity contribution to the polymer-zeolite adhesion,  $(\gamma_P^-)^{1/2}$ .

As this study was carried out in air, the effects of physically-adsorbed water should be considered. Although pure-silica MFI is widely regarded as hydrophobic, a small amount of water ( $\sim 0.03 \text{ cm}^3\text{g}^{-1}$ ) can be absorbed on the silanol groups that are associated with hydrophilic defects [33, 34]. According to Grivtsov et al., adsorption of water molecules onto the silanol groups may happen in two different modes: (1) hydrogen bonding between a silanol O-atom and a water H-atom, which orients the water O-atom outwards and makes the surface more basic, or (2) hydrogen bonding between a silanol H-atom and a water O-atom, which makes surface more acidic [35]. Therefore, depending on the mode of water adsorption onto silanol groups, a pure-silica MFI surface can become either more acidic or basic by water adsorption [36, 37].

Water molecules are likely to also be absorbed on the polymer surfaces via acidic-basic interactions, and water molecules absorbed on either polymer or zeolite surface can increase the polymer-zeolite adhesion force by enhancing the capability of hydrogen bonding [35]. Even though the model used here doesn't explicitly include the water effect, the experimental values may represent in part the effects of absorbed water that mediate the adhesion process.

Another potential artifact of water is the formation of bridges between tip and surface via condensed water. Capillary forces are regarded as significant in AFM measurements when *RH* is above 60 % [38, 39]. To check for potential capillary condensation, we carried out AFM adhesion measurements at *RH* values of 20 %, 35 %, and 75 % for a zeolite probe with two sample surfaces, one hydrophilic (PVAc) and one hydrophobic (PS), shown in Figure 3.6. For the PS surface, the adhesion force is essentially independent of humidity, suggesting that no water meniscus was formed between the zeolite and the hydrophobic PS surface, even at high *RH* of 75 %. For the PVAc polymer surface, adhesion force is differs little between 20 % and 35 % *RH*, but increases dramatically between 35 % and 75 % *RH*.

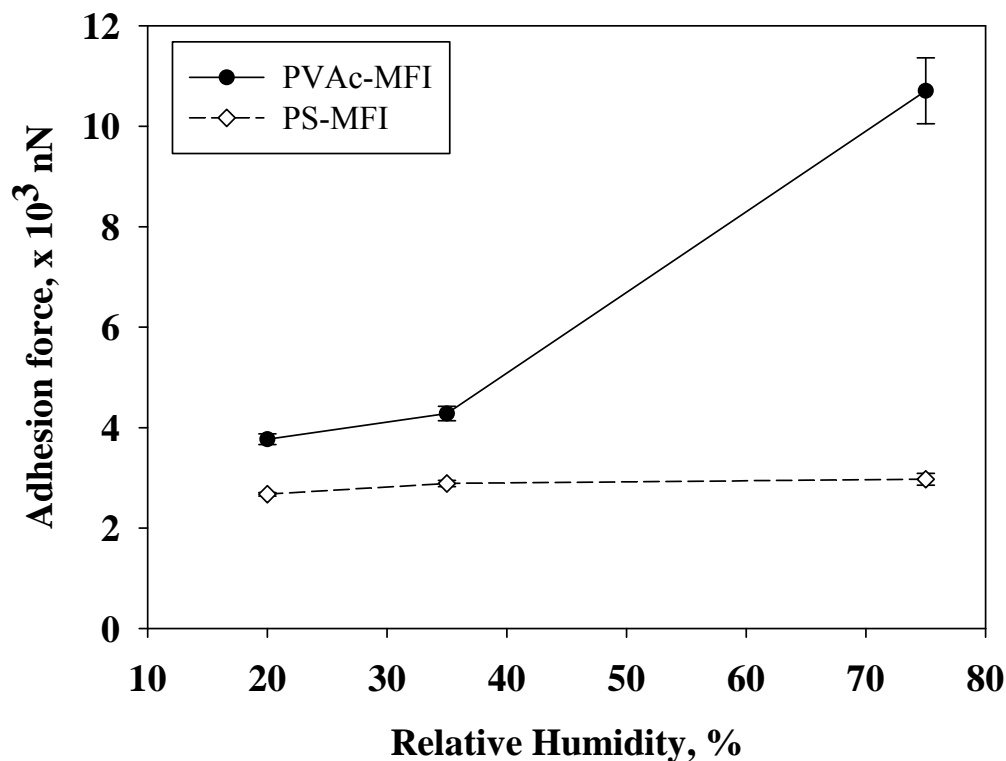


Figure 3.6: Adhesion force between a bare zeolite and polymer surfaces, PVAc (●) and PS (◇), as a function of relative humidity.

This large rise in adhesive force is consistent with the formation of capillary bridges. We can rationalize these results by using the Kelvin equation ( $r_c = 2\gamma V / (RT \ln(p/p^*))$ ) to predict the radius of curvature,  $r_c$ , at which water condensation can occur for a given  $RH$  value. Using a simple geometrical analysis, one can relate  $r_c$  to the depth of wetted meniscus ( $h$ ) on a terrace or crevice of angle  $\theta$ :  $r_c / (r_c + h) = \sin(\theta/2)$ . The depth,  $d$ , of these crevices or terrace steps ( $d^2 = (r_c + h)^2 - r_c^2$ ) can then be compared to the measured topography of the MFI crystal surface (Figure 3.2) to determine the likelihood of condensation. The Kelvin equation predicts  $r_c \approx 1$  nm for condensation at 35 %  $RH$ . For a perfect 90° terrace step, the step height  $d$  would have to be equal or less than  $r_c$  to support condensation. However, the AFM images (Figures 3.2), indicate no perfect terrace steps of this size. Rather, the terraces are usually sloping down at about 1 nm depth over 5 to 50 nm width. This leads to an oblique angle between steps that cannot

support condensation of drops with  $r_c = 1$  nm. In contrast, at  $RH = 75$  %,  $r_c = 3.6$  nm from the Kelvin equation, which predicts condensation on any step smaller than 3.6 nm, and there is evidence of condensation from the forces in Figure 6. The force difference between  $RH = 75$  % and 35 % is about 6 nN, which is in the expected range for capillary condensation. In contrast, at  $RH = 20$  %,  $r_c = 0.65$  nm, definitely smaller than anything observed on our surface. Thus capillary condensation is unlikely at 20 %  $RH$ . Very little change was observed in the force from 20 % to 35 %  $RH$ , suggesting that at 35 %  $RH$  we are not observing significant condensation. The small increase in PVAc adhesion, (4.28  $\mu$ N) at 35  $RH$  % comparing to that (3.8  $\mu$ N) at 20  $RH$  %, might be ascribed to an increased amount of adsorbed water on the PVAc surface [36, 37].

#### ***3.4.2.2. Surface-Modified MFI-Polymer Adhesion in Air***

We also measured adhesion forces between the surface-modified MFI (APDMES or Grignard treatment) and polymer surfaces using the zeolite colloidal probe method, and compared them to the results for the bare MFI zeolite. For comparison, measured adhesion forces were normalized by the value of zeolite surface area given in Table 3.1.

Figure 3.7 presents adhesion forces between MFI zeolite and polymers as a function of zeolite surface modification. Although surface modification of MFI zeolite with both aminosilane and Grignard treatment increased adhesion to all polymers, the degree of enhancement in adhesion by Grignard treatment was much higher than silane modification. The highly-roughened surface morphology resulting from Grignard treatment presumably enhances zeolite-polymer interfacial adhesion by increasing contact area and lowering the entropy penalty for polymer adsorption, as proposed by Shu et al. [14, 40, 41]. They found that the nanowhisker structures on LTA particle surfaces enhanced LTA-Ultem polymer interfacial adhesion, and thus improve mechanical and transport properties of resultant composites [41]. Later, we will present evidence that zeolite surface roughness enhances filler-polymer interfacial adhesion

during mixed-matrix membrane fabrication by characterizing mechanical, morphological, and thermal properties of polymer composites containing whisker-structured MFI zeolite in Chapter 6.

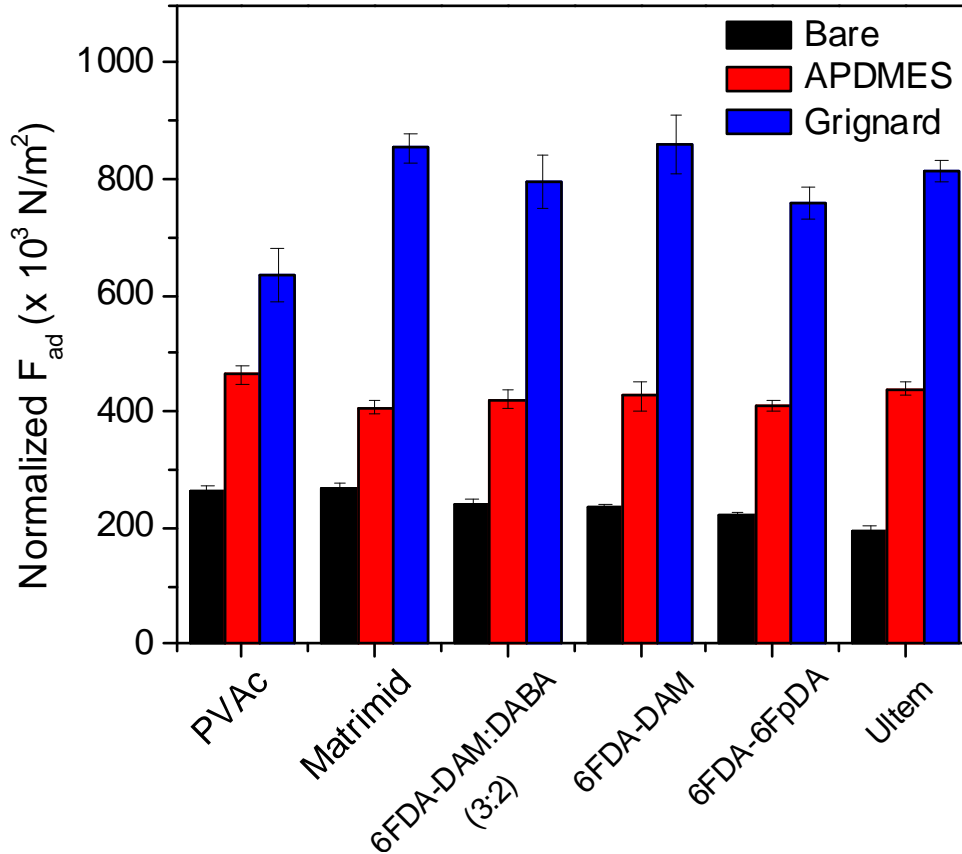


Figure 3.7: Adhesion force between a MFI zeolite and polymer surfaces as a function of zeolite surface chemistry.

### 3.5. CONCLUSIONS

In this chapter, AFM adhesion forces between a pure-silica MFI zeolite (010) surface (bare, silanated, and Grignard treated) and a series of polyimide and polyetherimide polymer surfaces were measured in air using a zeolite colloidal probe. For the bare MFI zeolite, adhesion forces between the zeolite and polymer surfaces were more strongly dependent on the Lewis basicity than on the VDW component of polymer surface energy. In fact, a change in the Lewis basicity component of surface energy had

6 times more influence on the adhesion than a change in the VDW component. We conclude that differences in adhesion as a function of polymer structure were primarily controlled by acid-base interactions (hydrogen bonding) between the basic components of the polymer and acidic components on the pure-silica MFI zeolite.

Physisorbed water may also play a role in mediating these interactions, however, capillary condensation of water has been excluded as a contributor to the adhesion at the humidity ( $RH = 35\%$ ) used herein. These results suggest that avenues to improve adhesion in mixed-matrix membranes could focus on enhancing the Lewis-acid-base interactions, either by modifications to the zeolite or polymer. In addition, we suggest that the density of carbonyl groups (or other Lewis basic group, depending on the polymer) is a useful metric for ranking relative adhesion values and could be of use in estimating the adhesion strength of new membrane polymers.

Surface modification on the zeolite, in particular by Grignard treatment, enhanced the zeolite-polymer interfacial adhesion significantly. This suggests that physical modification by increasing surface roughness could be a useful alternative to chemical modification for improving zeolite-polymer adhesive forces for fabricating defect-free membranes.

### 3.6. REFERENCES

1. Yong, H.H., N.C. Park, Y.S. Kang, J. Won, and W.N. Kim, J. Membr. Sci., 2001. **188**(2): p. 151-163.
2. Singh, A. and W.J. Koros, Ind. Eng. Chem. Res., 1996. **35**(4): p. 1231-1234.
3. Vankelecom, I.F.J., S. VandenBroeck, E. Merckx, H. Geerts, P. Grobet, and J.B. Uytterhoeven, J. Phys. Chem., 1996. **100**(9): p. 3753-3758.
4. Chung, T.S., L.Y. Jiang, Y. Li, and S. Kulprathipanja, Prog. Polym. Sci., 2007. **32**(4): p. 483-507.

5. Husain, S. and W.J. Koros, J. Membr. Sci., 2007. **288**(1-2): p. 195-207.
6. Good, R.J. and C.J. van Oss, *Modern Approach of Wettability: Theory and Applications*. 1991, New York: Plenum Press.
7. Hollander, A., J. Colloid Interface Sci., 1995. **169**(2): p. 493-496.
8. Correia, N.T., J.J.M. Ramos, B.J.V. Saramago, and J.C.G. Calado, J. Colloid Interface Sci., 1997. **189**(2): p. 361-369.
9. Janczuk, B., E. Chibowski, J.M. Bruque, M.L. Kerkeb, and F.G. Caballero, J. Colloid Interface Sci., 1993. **159**(2): p. 421-428.
10. Cornelius, C.J. and E. Marand, Polymer, 2002. **43**(8): p. 2385-2400.
11. Cornelius, C.J. and E. Marand, J. Membr. Sci., 2002. **202**(1-2): p. 97-118.
12. Kim, J.H., W.J. Koros, and D.R. Paul, Polymer, 2006. **47**(9): p. 3094-3103.
13. Agger, J.R., N. Hanif, C.S. Cundy, A.P. Wade, S. Dennison, P.A. Rawlinson, and M.W. Anderson, J. Am. Chem. Soc., 2003. **125**(3): p. 830-839.
14. Bae, T.H., J.Q. Liu, J.S. Lee, W.J. Koros, C.W. Jones, and S. Nair, J. Am. Chem. Soc., 2009. **131**(41): p. 14662-14663.
15. Stafford, C.M., K.E. Roskov, T.H. Epps, and M.J. Fasolka, Rev. Sci. Instrum., 2006. **77**(2): p. 023908.
16. Meredith, J.C., A. Karim, and E.J. Amis, Macromolecules, 2000. **33**(16): p. 5760-5762.
17. Meredith, J.C., A.P. Smith, A. Karim, and E.J. Amis, Macromolecules, 2000. **33**(26): p. 9747-9756.
18. Diaz, I., E. Kokkoli, O. Terasaki, and M. Tsapatsis, Chem. Mater., 2004. **16**(25): p. 5226-5232.



19. Cleveland, J.P., S. Manne, D. Bocek, and P.K. Hansma, *Rev. Sci. Instrum.*, 1993. **64**(2): p. 403-405.
20. Miyatani, T. and M. Fujihira, *J. Appl. Phys.*, 1997. **81**(11): p. 7099-7115.
21. Rurali, R. and N. Lorente, *Phys. Rev. Lett.*, 2005. **94**(2): p. 026805.
22. Busscher, H.J. and J. Arends, *J. Colloid Interface Sci.*, 1981. **81**(1): p. 75-79.
23. Ma, K.X., T.S. Chung, and R.J. Good, *J. Polym. Sci., Part B: Polym. Phys.*, 1998. **36**(13): p. 2327-2337.
24. Van Oss, C.J., *Interfacial forces in aqueous media*. 1994, New York: M. Dekker.
25. McCafferty, E. and J.P.J. Wightman, *J. Adhes. Sci. Technol.*, 1999. **13**(12): p. 1415-1436.
26. Geckeler, K.E., *Advanced macromolecular and supramolecular materials and processes*. 2003, Berlin: Springer.
27. Chan, C.K., S.L. Peng, I.M. Chu, and S.C. Ni, *Polymer*, 2001. **42**(9): p. 4189-4196.
28. Snyder, L.R., *Principle of Adsorption Chromatography*. 1968, New York: Marcel Dekker.
29. Unger, K.K., *Porous Silica*. 1979, Amsterdam: Elsevier.
30. Curthoys, G., V.Y. Davydov, A.V. Kiselev, S.A. Kiselev, and Kuznetso.Bv, *J. Colloid Interface Sci.*, 1974. **48**(1): p. 58-72.
31. Rochester, C.H. and A. Strachan, *J. Colloid Interface Sci.*, 1996. **177**(2): p. 456-462.
32. Joesten, M.D. and L.J. Schaad, *Hydrogen Bonding*. 1974, New York: Marcel Dekker.

33. Ramachandran, C.E., S. Chempath, L.J. Broadbelt, and R.Q. Snurr, *Microporous Mesoporous Mater.*, 2006. **90**(1-3): p. 293-298.
34. Flanigen, E.M., J.M. Bennett, R.W. Grose, J.P. Cohen, R.L. Patton, R.M. Kirchner, and J.V. Smith, *Nature*, 1978. **271**(5645): p. 512-516.
35. Grivtsov, A.G., L.T. Zhuravlev, G.A. Gerasimova, and L.G. Khazin, *J. Colloid Interface Sci.*, 1988. **126**(2): p. 397-407.
36. Holysz, L., *Colloids Surf. A*, 1998. **134**(3): p. 321-329.
37. Chakoumakos, B.C. and G.V. Gibbs, *J. Phys. Chem.*, 1986. **90**(6): p. 996-998.
38. Mcfarlane, J.S. and D. Tabor, *Proceedings of the Royal Society of London Series a-Mathematical and Physical Sciences*, 1950. **202**(1069): p. 224-243.
39. Fuji, M., K. Machida, T. Takei, T. Watanabe, and M. Chikazawa, *J. Phys. Chem. B*, 1998. **102**(44): p. 8782-8787.
40. Liu, J.Q., T.H. Bae, W.L. Qiu, S. Husain, S. Nair, C.W. Jones, R.R. Chance, and W.J. Koros, *J. Membr. Sci.*, 2009. **343**(1-2): p. 157-163.
41. Shu, S., S. Husain, and W.J. Koros, *J. Phys. Chem. C*, 2007. **111**(2): p. 652-657.

## **CHAPTER 4**

### **MEASUREMENT OF INTERPARTICLE FORCES IN NMP-WATER**

#### **MIXTURES: SILICA-SILICA SYMMETRIC SYSTEM**

Together with zeolite-polymer adhesion, the interaction between zeolite particles plays a crucial role in determining particle-polymer interfacial morphology and particle dispersion in mixed-matrix membranes. Certainly the adhesion forces between components in air, described in Chapter 3, reflect their interactions in the end state of the membrane formation process. However, membrane fabrication also involves interactions between components in solvent. In particular, hollow fiber mixed-matrix membranes are typically fabricated via a spinning process where polymer-solvent phase separation occurs starting at the outer fiber surface by solvent (NMP)–non-solvent (water) exchange [1, 2]. The full consideration of zeolite-zeolite, as well as zeolite-polymer interactions in different media, should enable us to understand better particle stability, dispersion, and membrane morphology associated with defect formation.

#### **4.1. OVERVIEW**

In this chapter, silica-silica interactions were chosen as a model system for interactions between zeolite particles in dope, because silica has a surface that is chemically similar to pure-silica MFI zeolite [3-5]. Silica is readily available as spheres, which allows us to use well-defined interaction models to analyze force data. The interfacial forces of a silica sphere with a silica-glass plate and polymer surfaces in media used in membrane spinning (air or NMP-water mixtures) were measured using the silica colloidal probe AFM technique. Adhesion and interactions of silica materials depend strongly on the medium. Silica-silica adhesion is weaker in general than silica-polymer

adhesion in solution, however, the relative magnitude of adhesion is the opposite in air. The behavior of the interactions between two silica surfaces in pure liquids followed qualitatively the prediction of the DLVO theory. The addition of NMP into water drastically altered the attractive and adhesive interactions compared to water alone. An unusually strong, long-range (50 ~ 80 nm), multi-stepped attractive force was observed on approach of hydrophilic silica surfaces in the NMP concentration range of 30 - 50 vol.%, where the pull-off force was also maximized. The origin of the observed long-range force was discussed based on analysis of the force curves, contact angle and zeta potential measurements, together with thermodynamic considerations. It is demonstrated that attraction most likely arises from bridging of surface adsorption layers composed of a macrocluster-like multilayered structure whose formation is driven by hydrogen bonding between the liquid components.

## **4.2. THEORETICAL BACKGROUND**

The interaction between two surfaces across a liquid medium is of fundamental and practical interest and is relevant to colloidal stability and dispersion [6-8]. In particular, the interaction behavior in mixed liquid systems is important in tribology, chromatography, separations, and composite fabrication [2, 9, 10]. Often, particle interactions measured in liquid media are explained in terms of the DLVO (Derjaguin-Landau-Verwey-Overbeek) theory, which consists of a repulsive electrostatic double-layer force and an attractive (in the case of two identical particles) van der Waals force. However, in many cases, the measured surface forces in a liquid cannot be expressed perfectly by DLVO forces due to additional forces. These “non-DLVO” forces include the hydro- or solvophobic force, capillary forces, and forces originating from competitive adsorption and liquid structuring near the surface [11].

A solid surface is known to induce positional or orientational ordering of liquid molecules near the solid-liquid interface, depending on the chemical nature of the surface

and liquid [8, 12]. Surface force measurements have revealed that molecular-layered structures exist on surfaces for various liquids, including pure liquids [8, 13, 14] and binary mixtures [10, 15, 16]. The molecular ordering often gives rise to an oscillatory solvation force with a period approximately equal to the diameter of the liquid molecule, reflecting the geometric packing of the liquid confined between the surfaces. It has been generally recognized that such molecular ordering may extend a few nanometers (below 10 nm) from the solid surface. In addition, this short-range structural force influences the magnitude of attractive interactions between surfaces [7, 17].

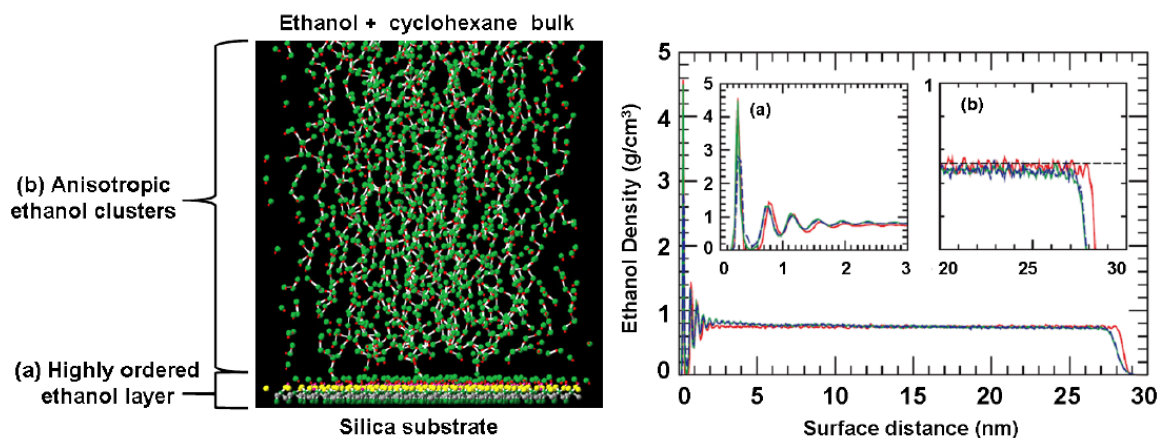


Figure 4.1: Simulated structure of surface macrocluster layers (left) and density profile of ethanol (right) on the silica surface in ethanol-cyclohexane mixtures: (a) highly-ordered ethanol layer ( $\sim 3$  nm) and (b) aggregate of anisotropic ethanol cluster ( $\sim 30$  nm) [12].

In contrast, Misukami et al. reported that long-ranged molecular structures extending several tens of nanometers from hydrophilic silica surfaces in binary mixtures, such as aliphatic or aromatic alcohols in a non-polar liquid such as cyclohexane [18-21]. They suggested that alcohols are able to form the organized layer structures, termed “surface molecular macroclusters”, through intermolecular hydrogen bonding. A molecular dynamics simulation provided a structural insight into the alcohol surface macrocluster on the silica surface. It was found that the macrocluster structure consists

of two layers – a highly-ordered first layer of alcohol molecules connected by hydroxyl groups to the silica surface via hydrogen bonding, and a second layer of anisotropic alcohol clusters with their long-axis oriented perpendicular to the surface, as shown in Figure 4.1 [12]. Contact of the macroclusters on opposite surfaces caused a long-range attraction extending to 40 - 70 nm, stemming from reduced interfacial tension between the macroclusters and the bulk phase as illustrated in Figure 4.2.

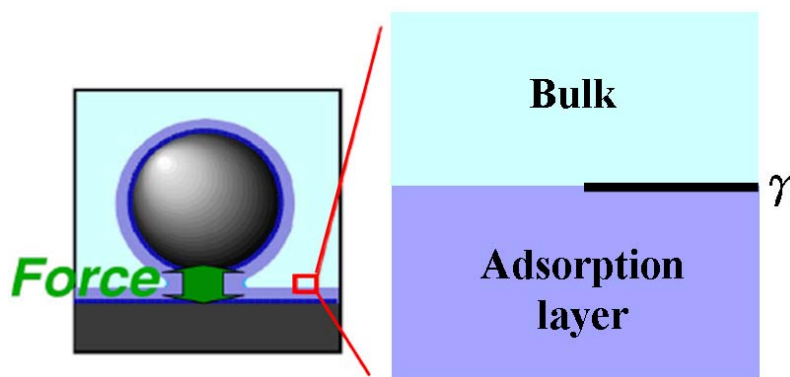


Figure 4.2: Schematic of bridging mechanism of the macrocluster surface adsorption layers.

The range of attraction corresponded to approximately twice the adsorption layer thickness. This bridging mechanism of the surface adsorption layers was also assumed to be responsible for the appearance of a maximum pull-off force between the hydrophilic silica surfaces at a specific alcohol composition. Similar structural forces arising from competitive adsorption onto silica surfaces between polar hydrogen bonding liquids were also observed for a 2,6-lutidine-water binary mixture [22]. More basic 2,6-lutidine was presumably able to adsorb preferentially on the silica surface relative to water molecules. It was proposed that the appearance of a strong attractive force at a specific 2,6-lutidine composition was due to overlap of the selective adsorption layer of 2,6-lutidine between opposing silica surfaces [22].

Hence, the presence of non-DLVO forces such as these structural and capillary forces should be taken into account together with the classical DLVO forces for a more accurate understanding of the macroscopic behavior of colloidal particle stability, dispersion and adhesion in complex mixtures of associating liquids [23, 24].

## **4.3. EXPERIMENTAL**

### **4.3.1. Materials and Procedure**

#### ***4.3.1.1. Materials***

Reagent-grade NMP ( $\geq 99.9\%$ , Aldrich) and polyetherimide Ultem<sup>®</sup> 1000 (GE Plastics) were used as received. Deionized (DI) water (18.2 M $\Omega$  cm) was prepared in a Millipore Milli-Q plus 185 purification system. Uniform silica microspheres ( $\sim 5\ \mu\text{m}$ ) were obtained in dry condition from Bangs Laboratories, Inc.

#### ***4.3.1.2. Sample Preparation***

##### ***4.3.1.2.1. Substrates***

The Hydrophilic silica plates were prepared by cleaning silica-glass slides in piranha solution (20/80 vol.% H<sub>2</sub>O<sub>2</sub>/H<sub>2</sub>SO<sub>4</sub>) at 80 °C for 1 h and thoroughly rinsing with DI water to increase the density of silanol groups on the glass surfaces. The water contact angle of the piranha-etched glass surface was estimated to be  $\sim 5^\circ$  by the sessile drop method. A Ultem<sup>®</sup> 1000 polymer film was prepared on the piranha-etched silicon substrate by a knife-edge coating method [25-27], as described in Chapter 3. The polymer film was dried at room temperature for 24 h after coating and then dried again under vacuum at 60 °C for 12 h.

##### ***4.3.1.2.2. Silica Colloidal Probes***

The silica colloidal probe was prepared by attaching a single silica microsphere to the apex of a tipless cantilever (FORT-TL, Applied NanoStructures, Inc.) using a

minimal amount of epoxy glue. No contamination of the silica particle was verified by the SEM inspection after force measurements, as shown in Figure 4.3. The gluing was completed by curing and drying at room temperature for 24 h. The silica colloidal probe was successively washed with ethanol, acetone, and DI water, and then transferred to a desiccator and stored prior to force measurements.

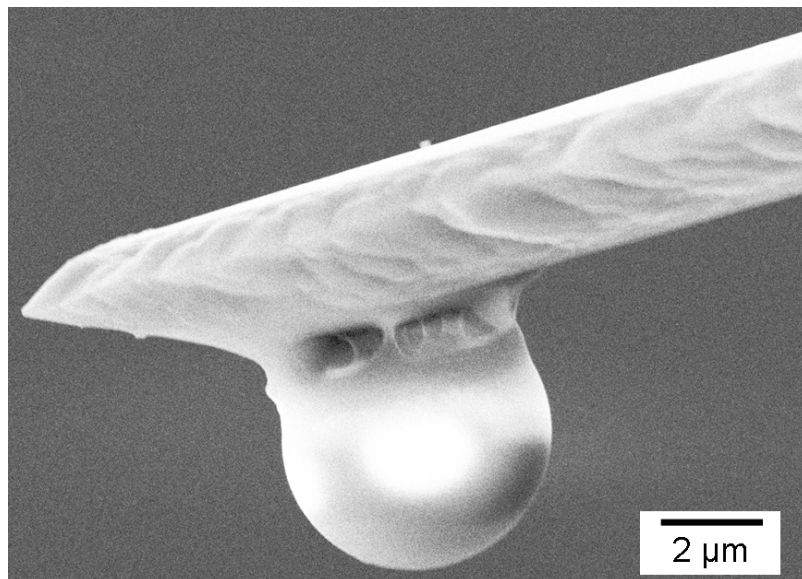


Figure 4.3: SEM image of a silica colloidal probe.

## 4.3.2. Experimental Methods

### 4.3.2.1. AFM Force Measurements

The interaction forces ( $F$ ) between a silica sphere and substrates were measured as a function of the separation distance ( $D$ ) in air or NMP-water mixtures using a scanning probe microscope (PicoScan 5, Molecular Imaging). Two types of substrates, a hydrophilic silica-glass plate and an Ultem polymer surface, were used in this study. The obtained diode voltage-displacement data were converted to cantilever deflection-distance curves by defining zeros of both force and separation. Cantilever deflections were converted to force by multiplying by the spring constant of the cantilever.



The spring constant of each cantilever was determined using the resonant frequency method. The stiffness of the cantilevers used in the present work was in the range of 2.23 - 2.86 N/m. The obtained forces were normalized by the radius ( $R$ ) of the sphere attached to the cantilever using the Derjaguin approximation [28]. The radius of the silica particle was estimated accurately from the SEM image.

To ensure the compatibility of the data obtained at different media, one tip was used throughout the force measurements. Forces applied to a probe during the measurement were kept constant at  $650 \pm 30$  nN. The approach speed of the colloidal probe to the substrate was kept in the range of 20 - 100 nm/s. The experimental results were independent of the approach rate, indicating that the hydrodynamic repulsion force was negligible. For each set of force measurements, force-distance curves were obtained from at least 30 randomly-chosen points within  $100 \times 100 \mu\text{m}^2$  areas on the substrate. Adhesive forces are determined from the average well depth of the retraction portion of force curves. The error bars for the force data correspond to the 99 % confidence interval. The forces at each medium condition were independent of the order of measurement. Experiments with a different probe produced qualitatively similar force data.

To ensure the negligible effect of the presence of epoxy resin on AFM experimental data, in particular, in NMP, raw approach force ( $F$ )-displacement curves were compared in pure water and NMP, respectively, as shown in Figure 4.4. From the contact lines of force-displacement curves it is possible to draw information about the elastic-plastic behavior of the cantilever. After surface contact, force curves exhibit straight contact lines both in pure water and in NMP without any additional deformation of the cantilever induced by the presence of epoxy resin between the silica particle and the probe. Furthermore, the slope of the force-displacement curve in the contact regime is a measure of the stiffness of the cantilever because the silica surface is assumed to be a hard material. The cantilever stiffness in NMP is the same as that in water, indicating

that the effect of the epoxy resin on the cantilever stiffness and hence force curves in NMP is negligible.

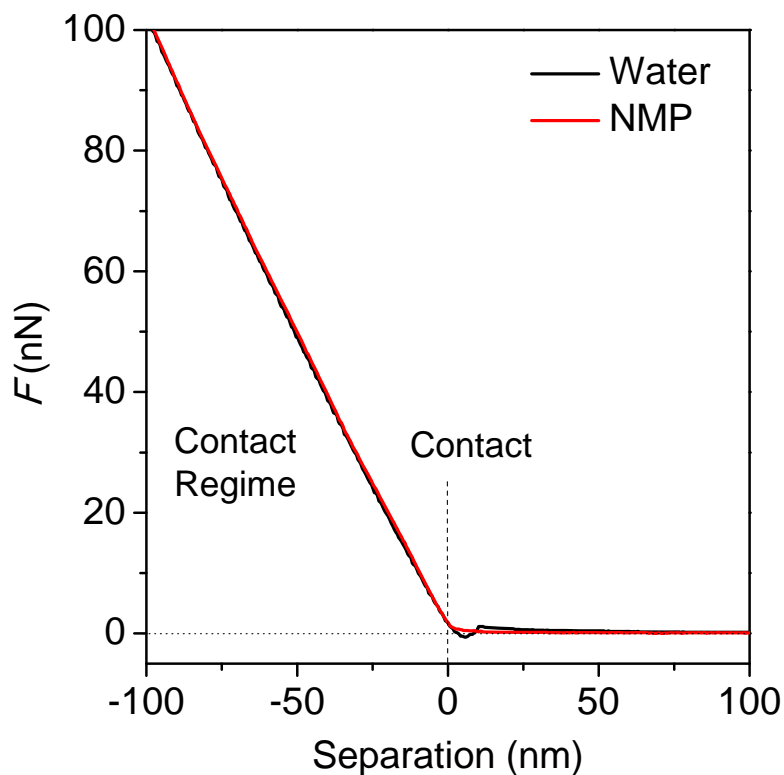


Figure 4.4: Raw approach force ( $F$ )-displacement curves between two silica surfaces in pure water and NMP, respectively.

#### 4.3.2.2. Contact Angle and Zeta Potential Measurements

The contact angles ( $\theta$ ) of NMP-water mixture solutions on the hydrophilic and hydrophobic glass surfaces were measured by the sessile drop method using a video capture apparatus (VCA2500XE, AST Products, Inc.) at room temperature. At least five droplets at different regions of the two pieces of the surface were used to obtain reliable contact angle data. Thus, the contact angle values are the averages of results obtained from a set of at least 10 experiments.

A Zetasizer 3000 instrument (Malvern Instrument) was used to measure the electrophoretic mobilities of the silica particles suspended in NMP-water mixtures as a

function of NMP concentration. The mobility data were converted to zeta potentials ( $\zeta$ ) using the Helmholtz-Smoluchowski equation. The zeta potential values are the averages of results obtained from a set of at least 3 experiments. All electrophoretic measurements were taken at room temperature.

#### **4.3.2.3. Solution Property Measurements**

Viscosity ( $\eta$ ) measurements of NMP-water mixtures at various NMP concentrations were performed with a Physica MCR-300 rheometer (Anton Paar UAS inc.) with cone-and-plate geometry at a shear rate of 1 – 1000 s<sup>-1</sup>.

### **4.4. RESULTS AND DISCUSSION**

#### **4.4.1. Silica-Silica versus Silica-Polymer Adhesion**

Adhesion of a silica sphere with a silica plate and an Ultem polymer surface are measured and compared as a function of medium conditions to understand the relative adhesive force of the siliceous material (zeolite) with other components (polymer and zeolite) present in the dope during the mixed-matrix membrane spinning process. Adhesion forces are strongly dependent on the medium, as shown in Figure 4.5. Silica-silica adhesion is weaker than silica-polymer adhesion in all NMP-water mixtures, with the difference in adhesion increasing with increasing water content. This result implies that silica-polymer adhesion becomes favorable relative to silica-silica adhesion as water amount in dope solution increases during solvent-exchange. However, silica-silica adhesion increases dramatically and overwhelms silica-polymer adhesion in air, suggesting that a complex change in mechanisms driving adhesion occurs during the drying process. These changes may, for example, lead to aggregation of siliceous particles (zeolites) within mixed-matrix membranes or to the delamination of polymer from the zeolite interface. However, it is important to point out that during spinning, these processes are occurring in a dynamic environment where the density and

composition of the solution is changing due to solvent exchange, polymer phase separation, and evaporation, simultaneously. In addition to these factors is the potential influence of shear forces. It is beyond the scope of this work to measure or model all of these factors. Rather, we seek to characterize quantitatively the equilibrium interactions between components in order to establish driving forces acting during the dynamic spinning process.

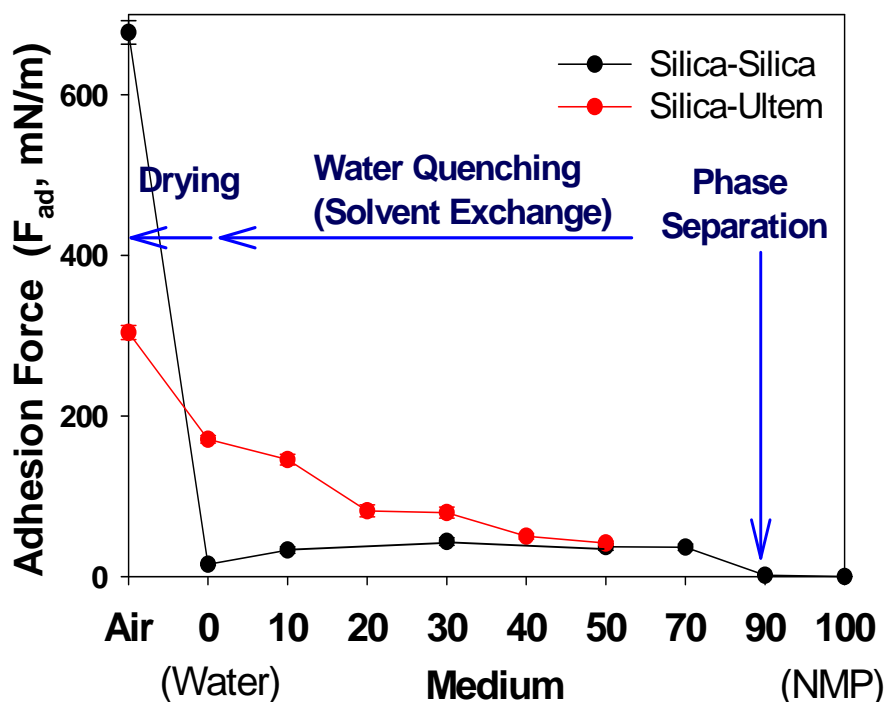


Figure 4.5: Silica-silica versus silica-polymer adhesion as a function of medium conditions.

#### 4.4.2 Silica-Silica Interactions in NMP-Water Binary Mixtures

##### 4.4.2.1. Interactions in Pure Liquids

Figures 4.6a and 4.6b show the typical force-distance curves between silica surfaces in DI water and in pure NMP, respectively, upon approach and retraction.

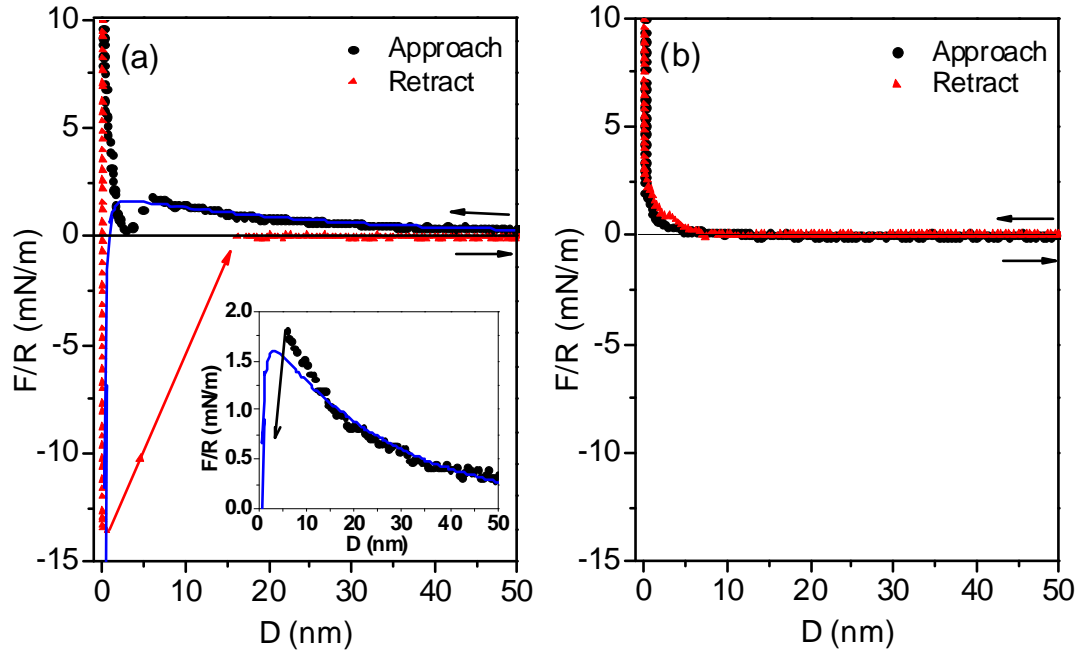


Figure 4.6: Force ( $F/R$ ) - separation ( $D$ ) curves between a hydrophilic silica sphere and a hydrophilic glass plate during approach and retraction in a pure liquid: (a) in DI water (The data points represent the experimental surface force and the solid line indicates the best fit to DLVO theory at constant surface potential. The fitting parameters are: Nonretarded Hamaker constant ( $H_A$ ) =  $6.5 \times 10^{-21}$  J, Debye length ( $\kappa^{-1}$ ) = 35 nm and surface potential ( $\psi_0$ ) = - 76 mV) and (b) in NMP.

The approach force curve in DI water exhibited the typical DLVO behavior which is a sum of the electrostatic force and the van der Waals force as shown in Figure 4.6a. When the surfaces approached, the interaction force increased exponentially from a large separation. This long-range interaction is attributable to the double-layer electrostatic repulsive force between the similarly charged surfaces. The repulsive interaction showed the maximum at  $\sim 6$  nm before the probe jumped onto the glass plate because of the van der Waals attractive force. The measured jump distance was within a few nanometers of the location predicted by the van der Waals attraction ( $\sim 2$  nm), although there was a degree of uncertainty in determining the point of zero separation [29]. It was similar to

the jump distance ( $\sim 7$  nm) reported by Vakarelski et al. for interaction between a silica sphere and a mica plate in pure water [30]. When the glass plate was pushed up further after the jump-into contact, a dip in the repulsive interaction was detected at  $\sim 3$  nm. When the glass plate was retracted from the probe, the probe jumped off from the surface at a certain separation of  $\sim 15$  nm. The pull-off force was determined from the average well depth upon retraction and estimated to be  $15 \pm 1$  mN/m, implying that only van der Waals attraction is acting between the two surfaces in water.

The experimental approach force curve was fitted to the DLVO theory assuming constant surface potential [7]. The values of the permittivity ( $\epsilon$ ) and refractive index ( $n$ ) of the media shown in Table 4.1 were used to calculate the nonretarded Hamaker constant ( $H_A$ ) for silica and glass across a liquid media on the basis of the Lifshitz theory [31].

Table 4.1: Permittivity ( $\epsilon$ ), refractive index ( $n$ ), dynamic viscosity ( $\eta$ ) and surface tension ( $\gamma$ ) of a NMP-water mixture as a function of NMP concentration (vol.%).

NMP vol %	$\epsilon^a$	$n^b$	$\eta$ (cP) <sup>c</sup>	$\gamma$ (mN/m) <sup>d</sup>
0	78.4	1.333	0.930	72.1
10	76.4	1.336	1.111	49.5
30	71.6	1.343	2.214	48.9
50	64.9	1.355	4.122	48.1
70	55.1	1.375	5.754	46.9
90	40.7	1.419	3.153	44.0
100	32.2	1.470	1.690	40.8

*Note.* <sup>a</sup> From literature [32]. <sup>b</sup> The values for the mixtures were calculated using simple mixing rule, while those for pure liquids were taken from literature [33, 34]. <sup>c</sup> The experimentally measured values. <sup>d</sup> From literature [35].

A nonretarded Hamaker constant of  $6.5 \times 10^{-21}$  J was calculated for pure water. The surface potential ( $\psi$ ) was estimated to be -76 mV from the best fit of the theoretical curve to the data, as illustrate in Figure 4.6a. The surface potential can be approximated by the zeta potential ( $\zeta$ ) because of the low ionic strengths involved [36]. There was a reasonable agreement between the fitted surface potential and the experimentally measured zeta potential value of -82 mV. Although the forces measured at large separation were described well by the DLVO theory, those at small separation could not be fitted to the DLVO force perfectly. It was found that the repulsive forces measured at distance, below approximately 10 nm, were larger than predicted by the DLVO theory, as shown in the inset of Figure 4.6a. This stronger repulsive force has been attributed to the hydration force originating from the ordered layering of water molecules in the vicinity of the silica surfaces [11, 29]. The dip in the interaction force observed at a separation of  $\sim 3$  nm has been interpreted in terms of the energy to break the hydration layer [17, 37-39].

The force curves in pure NMP were purely repulsive and almost identical during approach and retraction, as shown Figure 4.6b. The magnitude and range of the electrostatic repulsive force were suppressed in NMP media, compared to those in water. No jump-into contact and no measurable pull-off force were observed upon approach and retraction, respectively, indicating the attenuation of the van der Waals attraction in pure NMP.

The difference in the force curves measured in water versus in NMP could be qualitatively explained by the variation of the medium dielectric properties based on the DLVO theory. The observed repulsive interaction in pure NMP might have an electrostatic contribution because of the potential to form surface charges in polar organic liquids. The silica or glass surface can acquire a negative charge due to trace amounts of water in the nonaqueous system, although the charge is likely to be very small [17, 38]. This was confirmed by zeta potential measurement, which showed that the magnitude of

the zeta potential value of the silica particle was reduced by the addition of NMP into water, and the value for NMP was much smaller than that for pure water, as presented in Figure 4.7. Figure 4.7 also shows the Hamaker constant between silica and glass across the NMP-water medium, calculated from the Lifshitz theory using the medium properties given in Table 4.1, as a function of NMP concentration. The Hamaker constant and hence van der Waals attraction are predicted to decrease with increasing NMP concentration. Hence, the negligible pull-off and jump-into contact forces observed for NMP were mainly attributable to the weakening of van der Waals attraction caused by the variation in the refractive index and permittivity of the medium.

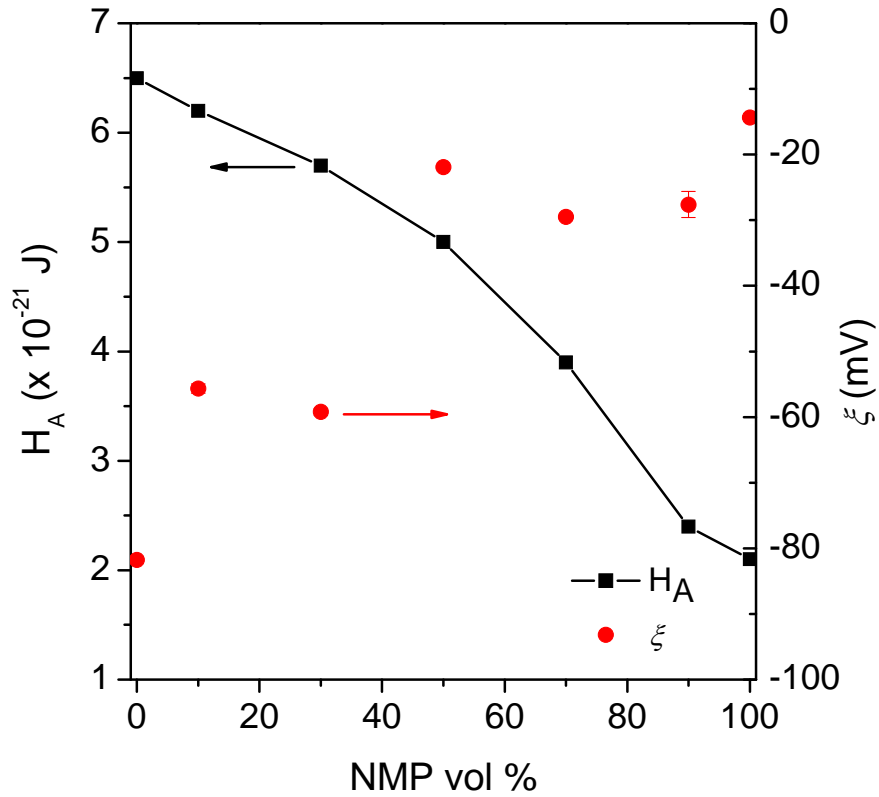


Figure 4.7: Nonretarded Hamaker constant ( $H_A$ ) as a function of NMP concentration (vol.%) for silica and glass surfaces across a NMP-water mixture calculated from the Lifshitz theory using the medium properties given in Table 4.1 and the experimental zeta potential value ( $\zeta$ ) of the silica particle suspension in a NMP-water mixture obtained from the electrophoretic mobility measurements.



#### 4.4.2.2. Interactions in NMP-Water Binary Mixtures

The surface force profiles between a hydrophilic silica sphere and a hydrophilic glass plate in NMP-water mixtures were measured as a function of NMP concentration and are illustrated in Figure 4.8a.

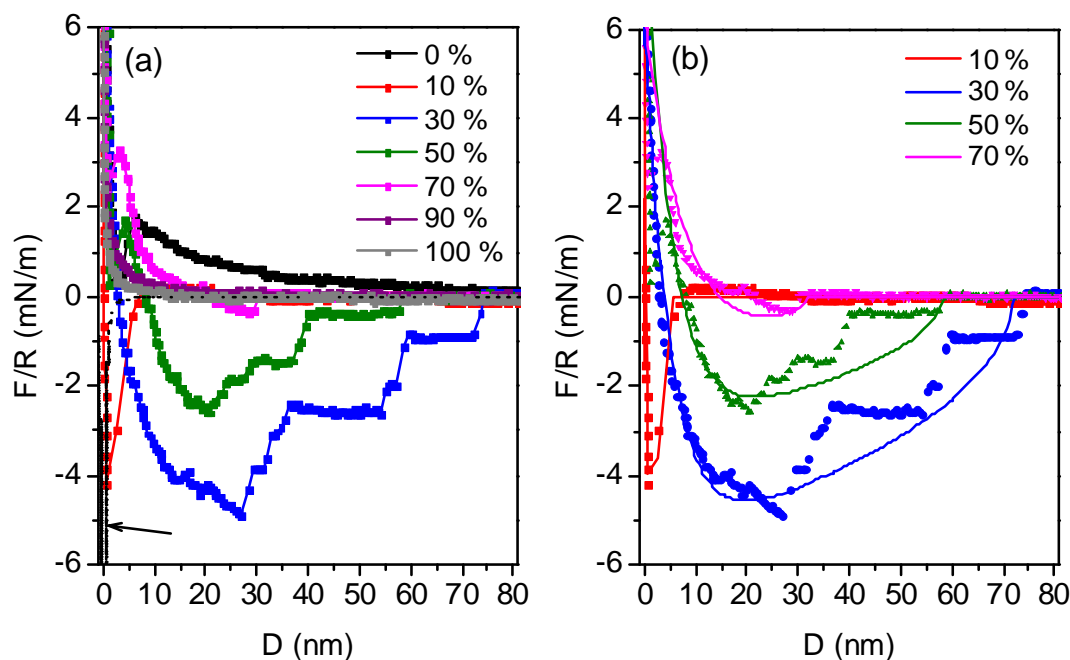


Figure 4.8: (a) Force ( $F/R$ ) - separation ( $D$ ) curves between a hydrophilic silica sphere and a hydrophilic glass plate during approach in NMP-water mixtures at various NMP concentrations (vol.%). (The dashed line indicated by the arrow represents the van der Waals attraction calculated by using a nonretarded Hamaker constant of  $6.5 \times 10^{-21}$  J for the silica/water/glass.) (b) Force profiles between the surfaces during approach in NMP-water mixtures at NMP concentrations of 10, 30, 50, and 70 vol.%. (data points represent the experimental surface force and solid line are curves fitted to equation 4.1.).

The addition of NMP into water drastically changed the magnitude and range of the interaction force. A remarkable increase in the magnitude of the attraction between the surfaces was observed at 10 vol.% NMP. The interaction was purely attractive, and the probe was pulled into strong adhesive contact from a separation of  $8.7 \pm 1.2$  nm,

resulting in a minimum attraction of  $\sim 4$  mN/m. The pull-off force was measured to be  $33.1 \pm 4.1$  mN/m, which was approximately twice that in water. A further increase in NMP concentration up to 30 - 50 vol.% led to strong and long-range attractive forces with multiple discontinuous step features. At 30 vol.% NMP, the long-range attraction appeared at a distance of  $75 \pm 9$  nm, exhibited the minimum interaction of  $\sim 5.0$  mN/m at  $\sim 25$  nm, and became repulsive at  $\sim 5$  nm upon compression. The measured pull-off force was further increased to  $50.2 \pm 5.5$  mN/m relative to that measured at 10 vol.% NMP. The magnitude and range of attraction as well as the pull-off force started to decrease with NMP concentration beyond 30 vol.%. At 50 vol.% NMP, the attractive interaction extended to  $66 \pm 8$  nm and became repulsive at  $\sim 10$  nm, and the interaction force had a maximum at a separation of  $\sim 7$  nm where the probe jumped onto the surface. It is noteworthy that the probe jumped into contact, exhibiting the repulsive maxima at NMP concentration higher than 30 vol.%, although this repulsive maximum disappeared beyond 70 vol.% NMP. The range of attraction decreased significantly to  $41 \pm 3$  nm at 70 vol.% NMP, and the long-range attractive force finally disappeared at 90 vol.% NMP, where the force curve was almost identical to that observed in pure NMP.

The change in the pull-off force ( $F_{off}/R$ ) and the range of attraction as a function of NMP concentration are shown in Figure 4.9. Both the attractive pull-off force and the range of attraction showed a maximum at 30 vol.% NMP, beyond which they started to decrease with a sharp reduction at NMP concentrations higher than 70 vol.%.

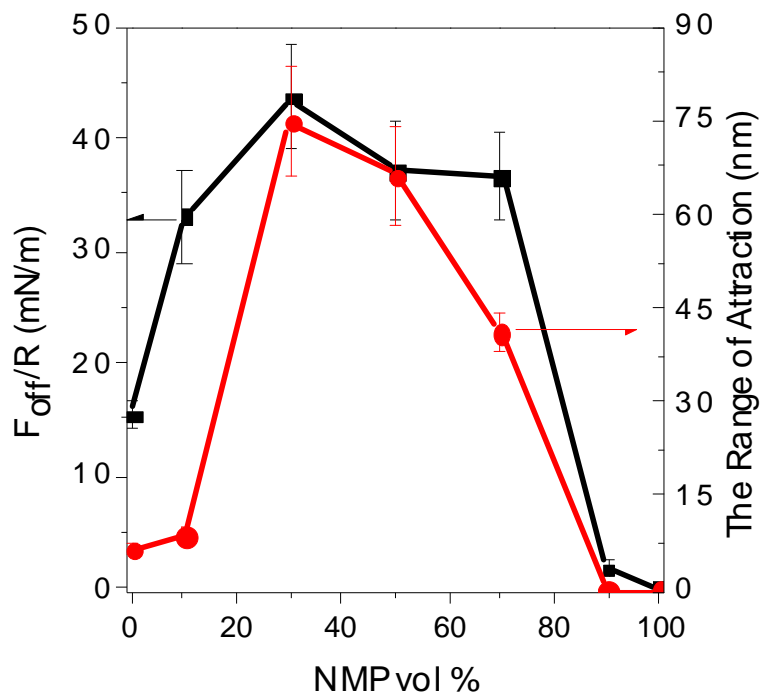


Figure 4.9: Pull-off force ( $F_{off}/R$ ) and the range of attraction between a hydrophilic silica sphere and a hydrophilic glass plate in a NMP-water mixture at various NMP concentrations (vol.%).

In contrary to the cases in pure liquids, it is difficult to explain the behavior of the interactions between the surfaces in NMP-water mixtures on the basis of the DLVO theory. DLVO theory predicts that attractive forces resulting from van der Waals interactions are expected to decrease gradually as NMP composition increases, because of the reduction in the Hamaker constant, as shown Figure 4.7. This contrasts with the dramatic changes in the attractive and pull-off forces following the addition of NMP. In addition, the range of the strong attractive force appearing at 30 - 50 vol.% NMP is much greater than that predicted by the van der Waals force ( $\sim 2$  nm). These unexpected features of the interaction forces imply that the interaction in a NMP-water mixture involves non-DLVO contributions.

The presence of solvent in water is known to alter liquid structuring near a surface [7, 11, 17]. By analogy to other studies of associating liquid mixture, the bridging of the

opposed surface adsorption layers upon approach might give rise to the sudden appearance of attraction not predicted by DLVO theory, as proposed also by other investigators [18-22, 40]. In addition, the sharp increase in the pull-off force may reflect the presence of a condensed adsorption layer around the surface at contact. This possible surface-induced phase separation is different from that occurring spontaneously in partially miscible mixtures, because NMP-water mixtures are completely miscible and no phase separation takes place in the bulk phase. Although local phase separation induced near hydrophilic silica surfaces in NMP-water mixtures has not been reported previously to our knowledge, the structural change accompanied by the preferential binding of NMP and displacement of the vicinal water by NMP on the silica surface appears to be expected based on molecular structure. For example, the silica surface contains weak-acid hydroxyl groups which easily adsorb water, as well as many basic organic molecules such as amines and amides through hydrogen bonding [41-44]. Water molecules are known to be adsorbed on the silica surface to form a multilayered structure through physical adsorption as well as hydrogen bonding [41, 45]. Upon the addition of NMP into water, a competition for adsorption sites on the silica surface would occur between the two polar components. Stronger liquid-solid interactions can cause one component in a liquid mixture to be preferentially adsorbed on the surface [10]. NMP is a cyclic amide and is a strongly dipolar aprotic solvent with two lone pairs of electrons on the amide carbonyl oxygen that act as a strong electron donor for hydrogen bonding [46-48]. In particular, the resonance structure of the amide carbonyl group promotes increased basicity of NMP, resulting in a tendency to form strong hydrogen bonds. In fact, it is known that compared to the OH groups of water, the amide carbonyl oxygen acts as a stronger acceptor site for hydrogen-bonding with hydroxyl protons [9, 48, 49]. As a result, NMP molecules can be expected to adsorb preferentially onto the oxide solid surface, relative to water. It was proposed by Yoon et al. that the preferential adsorption of methanol onto silica disrupts the hydration water structure in the vicinity of silica in

methanol-water mixtures [11]. The higher electrical dipole moment value of NMP (4.09 D) than that of water (1.82 D) may also contribute to the preferential adsorption of NMP [46, 47, 50].

Evidence for the displacement of water by NMP comes from contact angle measurements, as shown in Figure 4.10. Water contact angle on the hydrophilic silica surface was a finite value of  $\sim 5^\circ$ , while a droplet of pure NMP instantaneously spread, which indicated that NMP has a higher wetting affinity with the hydrophilic silica surface compared to water.

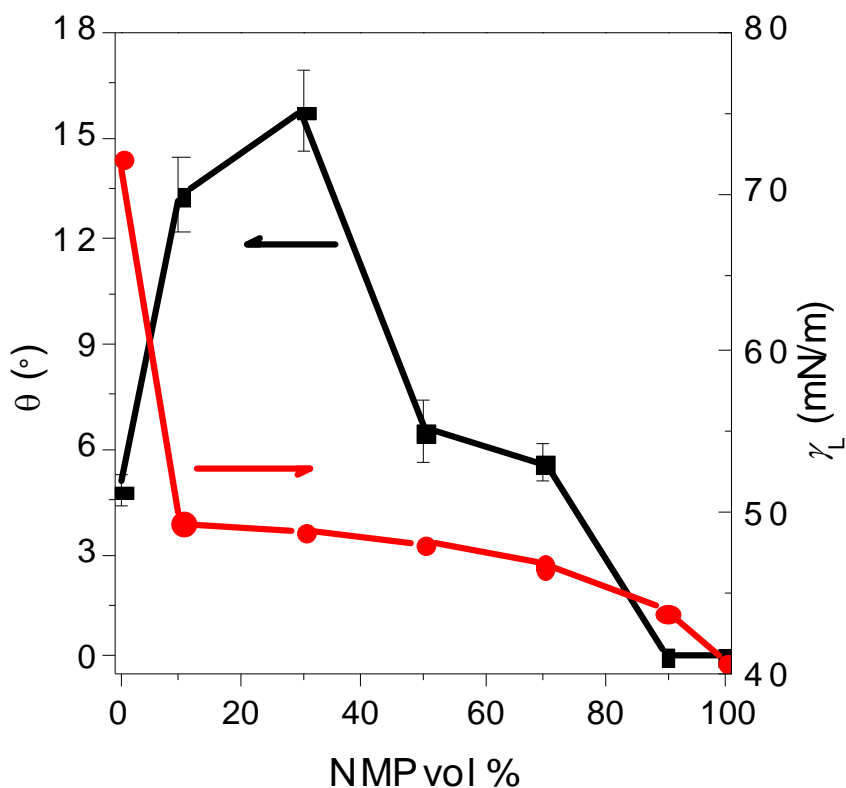


Figure 4.10: The contact angle ( $\theta$ ) on the hydrophilic glass plate and liquid-vapor surface tension ( $\gamma_L$ ) of a NMP-water mixture solution at various NMP concentrations (vol.%).

Together with the liquid-solid interaction, we should consider the effects of liquid-liquid interactions on the structuring of liquids near solid surfaces. The NMP-water binary mixture system is non-ideal and it shows complex fluid structure arising

from competing self- and hetero-associations [9, 46, 47]. Although NMP is not self-associative through hydrogen bonding, the NMP molecule is known to form energetically favorable  $\text{NMP}(\text{H}_2\text{O})_2$  heterocomplexes through strong hydrogen bonding, which results in a complex behavior in mixture thermophysical properties [9, 46, 47]. Even small amounts of NMP can be packed effectively into water structures by the formation of  $\text{NMP}(\text{H}_2\text{O})_2$  complexes. The disrupting effect on the water structure is more remarkable for water-rich mixtures where preferential heteroassociation occurs [9, 46, 47].

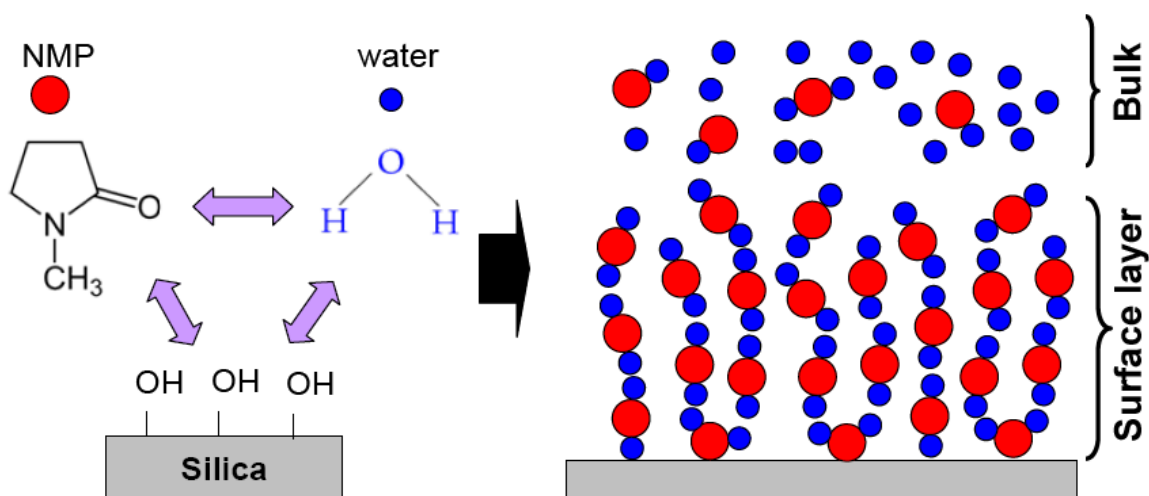


Figure 4.11: Competitive hydrogen bonding of liquid components (NMP and water) on the silica surface (left) and hypothesized liquid structures near the silica surface.

With these considerations, the structural change near the silica surface following the addition of NMP into water appears to be evident, although it may occur in a complicated way due to high affinity of NMP molecules both with water and hydroxyl groups on the silica surface. At small NMP fractions, water molecules adjacent to the silica surface are probably displaced by NMP molecules that subsequently form  $\text{NMP}(\text{H}_2\text{O})_2$  heterocomplexes. Although the complete exclusion of water molecules from the region adjacent to the silica surface may not be possible, NMP can break the hydrogen bonded water network within the hydration sheath on the silica surface by

forming these  $\text{NMP}(\text{H}_2\text{O})_2$  complexes, as shown in Figure 4.11. The preferential adsorption of NMP molecules onto silica and enhanced presence of NMP-water heteroassociations near the surface, relative to the bulk phase, is likely to be responsible for the changes in contact angle of the solution on glass.

The presence of NMP in water not only changed the contact angle on glass, but also affected the liquid-vapor surface tension of the solution, as illustrated in Figure 4.10. The addition of 10 vol.% of NMP into water drastically reduced the liquid-vapor surface tension of the solution. After this initial sharp decrease, the surface tension of the solution decreased weakly with the NMP composition. The trend is related to not only the presence of hydrophobic groups in NMP that tend to remain at the air-liquid interface, but also the influence of the interactions between NMP and water on the surface tension [35, 51]. If the change in the solution liquid-vapor surface tension was the dominant effect determining the wettability of the glass surface, we would expect the contact angle of the surface to decrease by the addition of NMP. However, this was not the case. The contact angle increased dramatically by the addition of 10 vol.% NMP, indicating an increase in the solid-liquid interfacial tension. This increased solid-liquid interfacial tension is consistent with the structural changes in the adsorption layer discussed above. Therefore, it is plausible to suggest that the remarkable increase in attraction observed by the addition of 10 vol.% NMP may result from the sudden bridging of surface adsorption layers created by the presence of NMP in water.

The further increase in NMP concentration up to 30 - 50 vol.% produced unusually strong and long-range attraction, as well as a maximum in adhesive force, behavior that is quite similar to that observed by Mizukami et al. for the interactions between silica surfaces in alcohol-cyclohexane mixtures [18-21]. They also proposed that the preferential adsorption of one liquid component induced the formation of macrocluster adsorption layers adjacent to the silica surface, whose bridging upon approach led to the long-range attraction. We expect the structure of the surface

macrocluster formed by competitive hydrogen-bonding in NMP-water mixtures to be similar to, but more complicated than, that observed in alcohol-cyclohexane mixtures, where the exclusive adsorption of one component (alcohol) onto the silica surface created the selective adsorption layer composed of a single species. It should be noted that step-wise attractions were observed in the range of 30 - 50 vol.% NMP. Multiple jumps in approach force curves have been observed in other pure liquid or mixture systems and are usually interpreted as rupture and subsequent displacement events of the individual liquid layers upon compression [7, 8, 17, 28, 29]. The appearance of multiple step-like attraction in the force profile for 30 - 50 vol.% NMP may reflect the formation of complicated and multilayered structures of the macrocluster adsorption layer in the vicinity of the hydrophilic silica surface. In fact, such complex and discrete layer structures on solid surfaces have been observed in other mixture liquids [10, 52]. As NMP concentration increased up to 30 - 50 vol.%, the increase in surface excess NMP may disrupt the hydrogen bonded water structure severely due to formation of  $\text{NMP}(\text{H}_2\text{O})_2$  complexes near the silica surface. Heterocomplex clusters might preferentially build up adjacent to the silica surface through intermolecular hydrogen bonding in line along the axis normal to the surface, leading to the creation of multilayered and longer-ranged aggregate structures of clusters extending a few tens of nanometers, which corresponds to approximately half the range of attraction. The solution contact angle on the silica glass surface was maximized at 30 vol.% NMP, which resulted presumably from the generation of high interfacial tension between the surface adsorption layer and the bulk phase.

We observed that the strength and range of attraction, as well as the pull-off force, started to decrease beyond 30 vol.% NMP. Simultaneously, the solution contact angle on the hydrophilic silica surface decreased with increasing NMP composition, indicating a reduction in the interfacial tension between the adsorption layer and the bulk solution. The formation of  $\text{NMP}(\text{H}_2\text{O})_2$  clusters in the bulk phase is known to affect significantly



the preferential adsorption phenomenon and hence surface liquid structuring [9, 20, 40]. In particular, it was proposed that the increase in the cluster formation in the bulk phase could reduce the surface adsorption layer-bulk interfacial energy by the exchange of solute between the clusters on the surface and those in the bulk solution [20, 40]. The further increase in NMP fraction beyond 30 vol.% might raise the amount of heterocomplex clusters in the bulk phase, which would be exchanged by those within the surface macrocluster layer, leading to a reduction in the adsorption layer-bulk interfacial tension [20, 40]. As a result, a shorter-ranged and less ordered, fragile structure of surface cluster layer is likely to form on the surface. It should be noted that the repulsive maxima and subsequent surface jump-into contact at 2 ~ 4 nm were observed at 50 - 70 vol.% NMP. The appearance of a jump-into contact in the repulsion regime may also be interpreted in terms of a less ordered surface adsorption layer, relative to that formed at 30 vol.% NMP. The surface layers formed in the range of 50 - 70 vol.% NMP are apparently broken by compressive forces applied by the approaching surfaces, resulting in the jump-into contact behavior. On the other hand, surface layers created at 30 vol.% NMP are relatively firm structures that would be gradually squeezed out upon compression without any surface ‘jump’. Together with the weakening of structural ordering, the interfacial tension and thickness of adsorption layer also appeared to decrease with NMP concentration beyond 30 vol.% NMP, which could account for a reduction in the strength and range of attraction, respectively, for 50 - 70 vol.% NMP.

The attractive force and pull-off force as well as the solution contact angle were reduced remarkably and no evidence for long-range attraction was observed beyond 70 vol.% NMP. The formation of NMP-water heterocomplex in the bulk phase was maximized at around 70 vol.% NMP, which coincides with the known viscosity of NMP-water mixtures, which exhibits a maximum at 70 vol.% NMP (corresponding to 33 mol.% NMP) due to the most efficient packing of NMP into  $\text{NMP}(\text{H}_2\text{O})_2$  structures [46] as shown in Table 4.1. The drastic increase in the exchange of cluster solutes between

adsorption layer and bulk solution is expected beyond 70 vol % NMP where the amount of NMP(H<sub>2</sub>O)<sub>2</sub> heteroclusters in the bulk reaches a plateau [9]. As a result, the interfacial tension as well as the thickness of the surface adsorption layer would be significantly reduced, resulting in a remarkable decrease in the magnitude and range of the attractive force beyond 70 vol.% NMP.

To verify this hypothesis, the approach force curves were analyzed using a model equation. The overall approach force profile, including bridging of macrocluster adsorption layers on the opposed silica surfaces, can be described by the following equation [20, 21, 40]:

$$\frac{F}{R} = \frac{F_\gamma}{R} + \frac{F_s}{R} = -\frac{2\pi\gamma\sqrt{(2t-D)(2R+D)}}{R} + ae^{-bD} \quad (4.1)$$

Here, the first term is the capillary attractive force caused by the contact of adsorption layers, and the second term is the steric repulsive force resulting from the overlap of adsorption layers upon compression, similar to the solvation force.  $F$ ,  $R$ ,  $\gamma$ ,  $t$ ,  $D$ ,  $a$ , and  $b$  are the force, radius of the sphere, interfacial energy, adsorbed layer thickness, distance, and reciprocal decay length of the solvation force, respectively.

Table 4.2: The fitting parameters ( $t$  and  $\gamma$ ) estimated from the force curves at 10 – 70 vol.% NMP.

NMP vol %	$t$ (nm)	$\gamma$ (mN/m)	$R^2$
10	$2.8 \pm 0.8$	$12.5 \pm 3.4$	$\sim 0.70$
30	$36.0 \pm 5.3$	$4.0 \pm 0.7$	$\sim 0.87$
50	$29.0 \pm 4.5$	$2.4 \pm 0.3$	$\sim 0.65$
70	$16.0 \pm 2.9$	$1.7 \pm 0.2$	$\sim 0.86$

*Note.* Uncertainty is 99 % confidence interval.

The values of  $t$  and  $\gamma$  were determined by fitting the experimental approach force to the model, as shown in Figure 4.8b (solid lines). The good quality of the fit supports the assignment of the long-range attraction to the contact of adsorbed layers. The fitting parameters ( $t$  and  $\gamma$ ) for the 10 - 70 vol.% NMP force curves are summarized in Table 4.2. The thickness of the adsorbed layer was close to the half of the range of attraction [18-21, 40]. As expected, the adsorption layer thickness had a maximum value of  $36 \text{ nm} \pm 5.3 \text{ nm}$  at 30 vol.% NMP, and decreased beyond 30 vol.% NMP. On the other hand, the interfacial tension decreased continuously with the NMP concentration in the range of 10 - 70 vol.%, as shown in Table 4.2. This indicates that the surface adsorption layer for 10 vol.% NMP is a thin, but highly ordered, structure generating the highest interfacial tension. A thicker and well ordered macrocluster layer with relatively high interfacial tension was formed at 30 vol.% NMP. A decrease in both the thickness and interfacial tension of the surface adsorption layer with increasing NMP concentration beyond 30 vol.% NMP is responsible for a reduction in the strength and range of attraction, respectively. An increase in clusters in the bulk phase with increasing NMP concentration probably promoted the exchange of solute clusters between adsorption layer and bulk solution, resulting in a reduction in interfacial tension, as well as in thickness of adsorption layer by disrupting the structures of adsorption layers.

The values of the solution contact angles ( $\theta$ ) on the hydrophilic glass surface were correlated with the measured pull-off forces ( $F_{off}/R$ ) and the ranges of attractions between the surfaces in NMP-water mixtures, as shown in Figure 4.12a and 4.12b, respectively. The pull-off force increased with  $\theta$ , in further support of the hypothesis that wetting layers (macroclusters) are governing the adhesion phenomena in NMP-water mixtures. The range of the attractive force increased with  $\theta$ , except the value at 10 vol.% NMP, as indicated by the arrow in Figure 4.12b. This extraordinary deviation at 10 vol.% NMP can be explained by the proposed bridging of the adsorption layers. The analysis of approach force curves revealed that the thinnest selective adsorption layers formed at 10

vol.% NMP, and were associated with the highest interfacial tension, as shown in Table 4.2. This thin adsorption layer might reduce the separation where the surfaces could experience the bridging attraction.

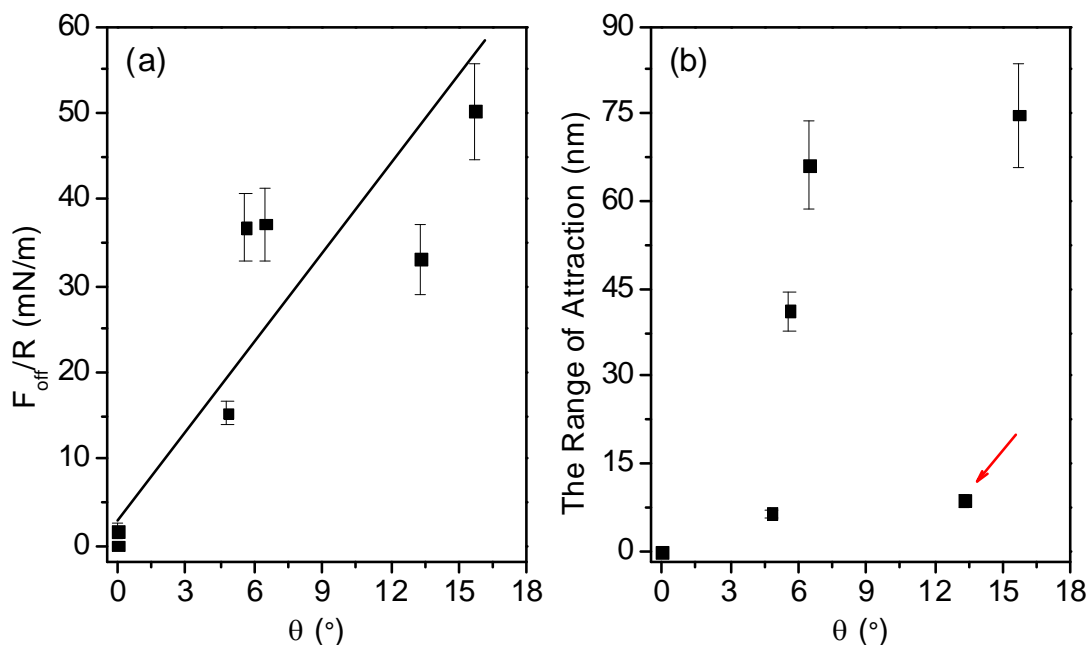


Figure 4.12: Correlation of the contact angle ( $\theta$ ) to (a) the pull-off force ( $F_{off}/R$ ) and (b) the range of attraction.

#### 4.5. CONCLUSIONS

In this chapter, the interactions between two hydrophilic silica surfaces in different media (air and NMP-water mixtures) were investigated by AFM force measurements. Silica-silica adhesion is weaker than silica-polymer adhesion in NMP-water mixtures; however, the relative magnitude of adhesion displayed the opposite trend in air. This suggests that mechanisms driving adhesion forces between components in dope solution depend strongly on the medium which is changed during the membrane spinning process.

The interactions between two silica surfaces in pure liquids were found to be qualitatively described by DLVO theory. However, in NMP-water mixtures, the forces

were altered drastically, characterized by attractive and adhesive forces that could not be described with DLVO theory. A strong, multi-stepped attraction appeared at a separation of 60 - 80 nm at 30 - 50 vol.% NMP in water. The adhesive pull-off force was maximized at around 30 vol.% NMP. This force was hypothesized to arise from the bridging of surface macrocluster-like adsorption layers on the hydrophilic silica surfaces, which was verified by solution contact angle measurements and force curve analysis. Competitive adsorption of NMP and water onto the silica surface, as well as hydrogen bonding between the liquid components through hydrogen bonding are believed to induce a complex liquid macrocluster near the hydrophilic surface. The decrease in the attraction and adhesion beyond 30 vol.% NMP was interpreted in terms of the reduction in the interfacial tension between the surface adsorption layer and bulk phase associated with the exchange of cluster solutes.

#### 4.6. REFERENCES

1. Chung, T.S., L.Y. Jiang, Y. Li, and S. Kulprathipanja, *Prog. Polym. Sci.*, 2007. **32**(4): p. 483-507.
2. Husain, S. and W.J. Koros, *J. Membr. Sci.*, 2007. **288**(1-2): p. 195-207.
3. Desbiens, N., I. Demachy, A.H. Fuchs, H. Kirsch-Rodeschini, M. Soulard, and J. Patarin, *Angew. Chem. Int. Ed.*, 2005. **44**(33): p. 5310-5313.
4. Eroshenko, V., R.C. Regis, M. Soulard, and J. Patarin, *J. Am. Chem. Soc.*, 2001. **123**(33): p. 8129-8130.
5. Lee, J.H., B.J.R. Thio, T.H. Bae, and J.C. Meredith, *Langmuir*, 2009. **25**(16): p. 9101-9107.
6. Franz, V. and H.J. Butt, *J. Phys. Chem. B*, 2002. **106**(7): p. 1703-1708.
7. Kanda, Y., T. Nakamura, and K. Higashitani, *Colloids Surf. A*, 1998. **139**(1): p. 55-62.

8. Bonaccorso, E., M. Kappl, and H.J. Butt, *Curr. Opin. Coll. Interface Sci.*, 2008. **13**(3): p. 107-119.
9. Hong, P.D. and H.T. Huang, *Polymer*, 2000. **41**(16): p. 6195-6204.
10. Lim, R.Y.H. and S.J. O'Shea, *Langmuir*, 2004. **20**(12): p. 4916-4919.
11. Yoon, R.H. and S. Vivek, *J. Colloid Interface Sci.*, 1998. **204**(1): p. 179-186.
12. Andoh, Y., K. Kurahashi, H. Sakuma, K. Yasuoka, and K. Kurihara, *Chem. Phys. Lett.*, 2007. **448**(4-6): p. 253-257.
13. Lim, R. and S.J. O'Shea, *Phys. Rev. Lett.*, 2002. **88**(24): p. 246101.
14. Sun, G.X., E. Bonaccorso, V. Franz, and H.J. Butt, *J. Chem. Phys.*, 2002. **117**(22): p. 10311-10314.
15. Christenson, H.K., *Chem. Phys. Lett.*, 1985. **118**(5): p. 455-458.
16. Christenson, H.K. and C.E. Blom, *J. Chem. Phys.*, 1987. **86**(1): p. 419-424.
17. Kanda, Y., S. Iwasaki, and K. Higashitani, *J. Colloid Interface Sci.*, 1999. **216**(2): p. 394-400.
18. Mizukami, M. and K. Kurihara, *Chem. Lett.*, 1999(10): p. 1005-1006.
19. Mizukami, M. and K. Kurihara, *Chem. Lett.*, 2000(3): p. 256-257.
20. Mizukami, M., M. Moteki, and K. Kurihara, *J. Am. Chem. Soc.*, 2002. **124**(43): p. 12889-12897.
21. Mizukami, M., Y. Nakagawa, and K. Kurihara, *Langmuir*, 2005. **21**(21): p. 9402-9405.
22. Beysens, D. and D. Esteve, *Phys. Rev. Lett.*, 1985. **54**(19): p. 2123-2126.

23. Li, Y.Q., N.J. Tao, J. Pan, A.A. Garcia, and S.M. Lindsay, *Langmuir*, 1993. **9**(3): p. 637-641.
24. Regdon, I. and I. Dekany, *Colloid Polym. Sci.*, 2003. **281**(9): p. 845-851.
25. Meredith, J.C., A. Karim, and E.J. Amis, *Macromolecules*, 2000. **33**(16): p. 5760-5762.
26. Meredith, J.C., A.P. Smith, A. Karim, and E.J. Amis, *Macromolecules*, 2000. **33**(26): p. 9747-9756.
27. Stafford, C.M., K.E. Roskov, T.H. Epps, and M.J. Fasolka, *Rev. Sci. Instrum.*, 2006. **77**(2): p. 023908.
28. Butt, H.H. and R. Stark, *Colloids Surf. A*, 2005. **252**(2-3): p. 165-168.
29. Brant, J.A. and A.E. Childress, *Environ. Eng. Sci.*, 2002. **19**(6): p. 413-427.
30. Vakarelski, I.U., K. Ishimura, and K. Higashitani, *J. Colloid Interface Sci.*, 2000. **227**(1): p. 111-118.
31. Lifshitz, E.M., *Sov. Phys. JETP*, 1956. **2**: p. 73.
32. Virtanen, P.O., *Suomen Kemistilehti*, 1967. **40**(11): p. 313-316.
33. Blanco, B., S. Beltran, J.L. Cabezas, and J. Coca, *J. Chem. Eng. Data*, 1997. **42**(5): p. 938-942.
34. Dancil, K.P.S., D.P. Greiner, and M.J. Sailor, *J. Am. Chem. Soc.*, 1999. **121**(34): p. 7925-7930.
35. Garcia-Abuin, A., D. Gomez-Diaz, J.M. Navaza, and I. Vidal-Tato, *J. Chem. Eng. Data*, 2008. **53**(11): p. 2671-2674.
36. Veeramasuneni, S., M.R. Yalamanchili, and J.D. Miller, *J. Colloid Interface Sci.*, 1996. **184**(2): p. 594-600.

37. Adler, J.J., Y.I. Rabinovich, and B.M. Moudgil, J. Colloid Interface Sci., 2001. **237**(2): p. 249-258.
38. Freitas, A.M. and M.M. Sharma, J. Colloid Interface Sci., 2001. **233**(1): p. 73-82.
39. Toikka, G., R.A. Hayes, and J. Ralston, J. Colloid Interface Sci., 1996. **180**(2): p. 329-338.
40. Yilmaz, N., M. Mizukami, and K. Kurihara, Langmuir, 2007. **23**(11): p. 6070-6075.
41. Airoidi, C. and L.S. Santos, Thermochim. Acta, 1986. **104**: p. 111-119.
42. Arakaki, L.N.H., J.G.P. Espinola, S.F. de Oliveira, J.M.P. de Freitas, A.G. Gouveia, and C. Airoidi, Colloids Surf. A, 2002. **203**(1-3): p. 129-136.
43. Belyakova, L.A., N.N. Vlasova, L.P. Golovkova, A.M. Varvarin, D.Y. Lyashenko, A.A. Svezhentsova, N.G. Stukalina, and A.A. Chuiko, J. Colloid Interface Sci., 2003. **258**(1): p. 1-9.
44. Musto, P., G. Ragosta, G. Scarinzi, and L. Mascia, Polymer, 2004. **45**(5): p. 1697-1706.
45. Parida, S.K., S. Dash, S. Patel, and B.K. Mishra, Adv. Colloid Interface Sci., 2006. **121**(1-3): p. 77-110.
46. Aparicio, S., R. Alcalde, M.J. Davila, B. Garcia, and J.M. Leal, J. Phys. Chem. B, 2008. **112**(36): p. 11361-11373.
47. Davila, M.J., R. Alcalde, and S. Aparicio, Ind. Eng. Chem. Res., 2009. **48**(2): p. 1036-1050.
48. Chen, X.H., K.E. Gonsalves, and M.I. Baraton, Chem. Mater., 1997. **9**(1): p. 328-333.
49. Fawcett, W.R., J. Phys. Chem., 1993. **97**: p. 9540-9546.



50. Riddick, J.A., W.B. Bunger, and T.K. Sakano, *Organic Solvents: Physical Properties and Methods of Purification*. 1986, New York: John Wiley & Sons.
51. Kokkoli, E. and C.F. Zukoski, J. Colloid Interface Sci., 1999. **209**(1): p. 60-65.
52. Lin, Q., E.E. Meyer, M. Tadmor, J.N. Israelachvili, and T.L. Kuhl, Langmuir, 2005. **21**(1): p. 251-255.

## **CHAPTER 5**

### **MEASUREMENT OF INTERPARTICLE FORCES IN NMP-WATER MIXTURES: SILICA-SILANATED SILICA ASYMMETRIC SYSTEM**

#### **5.1. OVERVIEW**

Together with zeolite-zeolite interactions, the interplay of zeolite-solvent and zeolite-polymer interactions is suggested to determine the final structure of mixed-matrix membrane [1, 2]. Mahajan and Koros emphasized on the use of solvents that interact less or poorly with the molecular sieve compared to the polymer; thus preventing competition of the solvent molecules with the polymer for the sieve surface [2]. On the other hand, silanes have been used to modify the zeolite surface to improve compatibility with the polymer [1, 3, 4]. However, how the silane layer on the silica (zeolite) surface affects zeolite-solvent interactions as well as zeolite-zeolite interactions, which is related with the membrane morphology, is unanswered. We demonstrated that NMP-water mixtures can induce the surface adsorption layer on the hydrophilic silica surface due to high affinity between the silica surface and solvent molecules, resulting in strong and long-range attraction between two hydrophilic silica surfaces in Chapter 4. In this chapter, we report the forces for asymmetric surfaces between a silica particle and a silanated, hydrophobic glass plate in NMP-water mixtures using AFM. The results from the asymmetric case, are compared with the symmetric case, in order to understand the effect of the silane layer on the liquid structuring on the silanated surface, associated with silica-solvent interactions, as well as the role of non-DLVO forces in silica-silica interactions in associating solutions. A strong and long-range attractive force was observed in pure water. This attraction was affected significantly by the topography of

the hydrophobic surface, and was attributed to a capillary force arising from the bridging of the two surfaces by nanoscale bubbles on the hydrophobic surface. The pull-off force decreased with increasing NMP concentration, which was explained in terms of the wettability of the surface determined by solution contact angle. Similar to the case of symmetric surfaces, a long-ranged attraction between the asymmetric surfaces was observed as % NMP increased, with a maximum attraction at 30 vol. % NMP, which is in good agreement with the formation of surface macrocluster layers on the hydrophilic silica surface.

## **5.2. THEORETICAL BACKGROUND**

In addition to the liquid structural forces discussed in Chapter 4, solvo- or hydrophobic forces have also been considered as non-DLVO interactions between surfaces. Strong and long-range attractions between hydrophobic surfaces in aqueous media have been generally designated as “hydrophobic” interactions [5-21]. Although several mechanisms for these hydrophobic forces have been proposed, much attention has been paid to the role of bubbles and dissolved gas in aqueous solutions between two hydrophobic surfaces, particularly in the case of silanated glass surfaces and solid polymers. Together with AFM imaging and other experimental evidence, such as neutron or X-ray reflectivity, direct force measurements provide evidence that the long-range attraction acting between chemically silanated surfaces in aqueous medium originates from the spontaneous capillary bridging of preexisting submicroscopic bubbles on the surface [5-21]. Submicroscopic bubbles, which are introduced by the exposure of the hydrophobic surface to air, or by dissolved air in the water, nucleate on defect sites on the hydrophobic surfaces. As the surfaces approach, the bubbles coalesce to form a capillary bridge between surfaces, generating a strong and long-range attraction that seeks to decrease the bubble surface area. This attraction is due to the unfavorable liquid-vapor interfacial energy and large negative Laplace pressure within the capillary bridge

[21]. Together with liquid structural forces discussed in Chapter 4, solvo- or hydrophobic forces should be taken into account for an understanding of the role of non-DLVO forces in interactions between silica surfaces in NMP-water mixtures.

### **5.3. EXPERIMENTAL**

#### **5.3.1. Materials and Procedure**

##### ***5.3.1.1. Materials***

Reagent-grade NMP ( $\geq 99.9\%$ ) and octadecyltrichlorosilane (OTS,  $\geq 99.9\%$ ) were purchased from Aldrich and used as received. Deionized (DI) water ( $18.2\text{ M}\Omega\text{ cm}$ ) was prepared in a Millipore Milli-Q plus 185 purification system. Uniform silica microspheres ( $\sim 5\text{ }\mu\text{m}$ ) were obtained in dry condition from Bangs Laboratories, Inc.

##### ***5.3.1.2. Sample Preparation***

Hydrophobic glass surfaces were obtained by immersing the piranha-etched glass slides in a 0.1 vol.% solution of OTS in toluene under a nitrogen atmosphere. The hydrophobicity of the glass plate was controlled by varying the immersion time (5, 10 and 60 min). Excess OTS was removed with a toluene rinse after silanation. The arithmetic average ( $Ra$ ) and root-mean-square ( $Rms$ ) roughness for the hydrophobic glass surface were obtained from topography of  $5 \times 5\text{ }\mu\text{m}^2$  areas using a scanning probe microscope (PicoScan 5, Molecular Imaging) operated in tapping mode.

#### **5.3.2. Experimental Methods**

The silica colloidal probe used in Chapter 4 was employed to measure the surface forces between a hydrophilic silica sphere and a hydrophobic silica surface. AFM surface force and contact angle measurements were followed by the procedure described in Chapter 4.

## 5.4. RESULTS AND DISCUSSION

### 5.4.1. Hydrophilic Silica-Hydrophobic Silica Interactions in Water

Figure 5.1a shows the approach force curves between a hydrophilic silica sphere and a series of silanated glass plates of varying water contact angle.

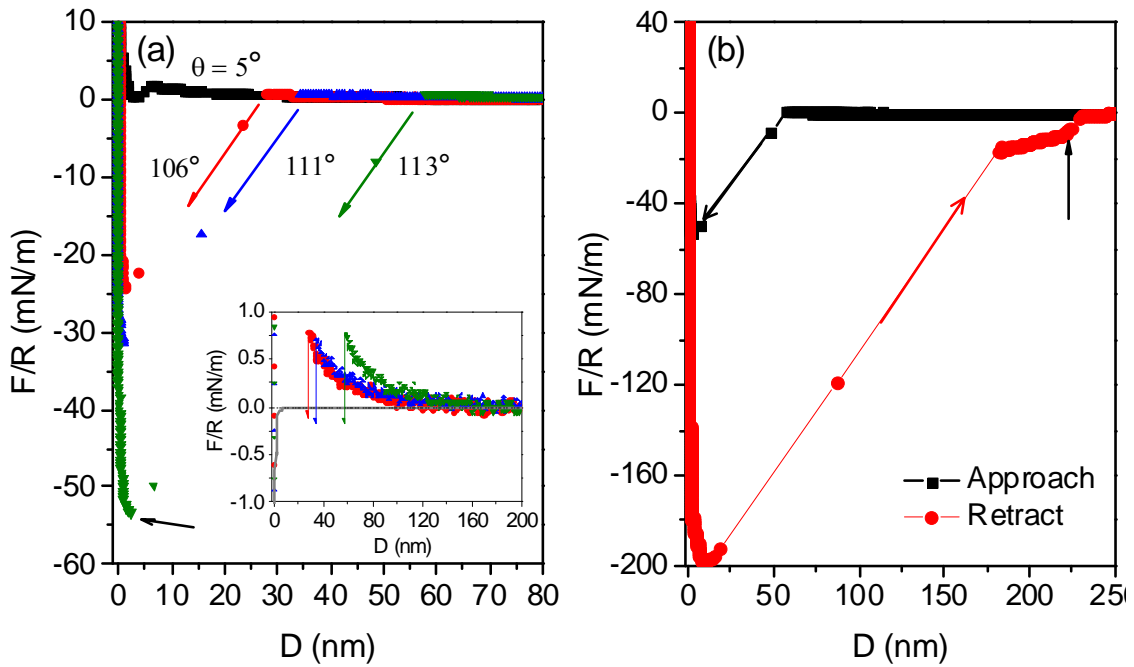


Figure 5.1: (a) Force ( $F/R$ ) - separation ( $D$ ) curves between a hydrophilic silica sphere and OTS-coated glass plates having different contact angles ( $\theta = 5, 106, 111$  and  $113^\circ$ ) during approach in DI water (The solid line in the inset represents the van der Waals attraction calculated by using a nonretarded Hamaker constant of  $7.1 \times 10^{-21}$  J for the silica/water/OTS-coated glass). (b) Force-separation curves between a hydrophilic glass sphere and an OTS-coated glass plate ( $\theta = 113^\circ$ ) during approach and retraction in DI water. (The arrow indicates a jump at a large separation during retraction).

Upon approach, the surfaces experienced repulsion at large separations before the probe jumped into contact, as shown in the inset of Figure 5.1a. Typically, the force curve exhibited jump-into contact at a distance longer than 25 nm, indicating a strong and long-range attraction. The jump-in distance increased sharply with the water contact

angle ( $\theta$ ) of the hydrophobic surface: The average jump-in distances were  $28 \pm 3$  and  $50 \pm 9$  nm for water contact angles  $\theta = 106$  and  $113^\circ$ , respectively. The forces measured between the hydrophilic and hydrophobic surfaces were much stronger and longer-ranged than the predicted van der Waals attractive force, as shown in the inset of Figure 5.1a, even after the effect of the OTS layer was taken into account. The OTS layer increases the van der Waals force by 10 % [22, 23]. The gradient of the van der Waals force curve predicted that the cantilever would jump into contact at a distance of about 2 nm, which was much shorter than the experimentally measured jump-in distances.

The abrupt appearance of a long-range attraction at a separation of 25 - 60 nm, far beyond van der Waals force range, can be explained by the capillary force originating from the spontaneous bridging of preexisting submicroscopic bubbles. This mechanism has been generally accepted to interpret the strong and long-range attraction observed between two hydrophobic surfaces, in particular, for the chemically silanated surfaces. For the relatively less stiff colloidal probe used in the AFM, the surface jumped into contact immediately upon bubble bridging, resulting in instantaneous jumps at large separation in the force curves [5, 10, 12, 21]. The measured jump-in distance has been considered to be comparable to the height of the preexisting bubble on the surface [9, 11, 12, 21]. Indeed, it was previously observed that the nanobubble bridging mechanism governs the asymmetric interaction between a hydrophilic and a hydrophobic surface, much like two hydrophobic surfaces [9, 22]. Thermodynamic considerations have been used to demonstrate that nanobubbles can exist on rough and hydrophobic surfaces. The net capillary force arising from bubble bridging can be attractive in the case of asymmetric surfaces where one of the surfaces is hydrophilic ( $\theta \sim 0^\circ$ ), although in that case the contact angle of the other surface should exceed  $90^\circ$  [22].

In fact, long-range attractive forces between a hydrophilic and a silanated, hydrophobic surface in water have been measured up to a surface separation of  $\sim 80$  nm, although the magnitude and range of the force were dependent on the experimental setup

and the hydrophobization method [5, 7, 9, 10, 23]. In particular, the range of the attractive forces observed in this work (25 - 60 nm) is comparable to that reported by Ducker et al. for a similar asymmetric system [22]. They observed long-range attraction at a separation of 25 - 75 nm between a hydrophilic silica sphere and an OTS-coated silica plate, and attributed the sudden jump-into contact at a large separation to the bubble bridging mechanism [22]. In addition to the observation of the steps and discontinuities at large separation [5, 7, 10, 14, 15, 17-21], the force profiles obtained in the present study exhibit other characteristic features suggestive of nanobubble bridging. Upon approach, a short-range repulsion prior to the onset of the long-range attraction was observed, as shown in the inset of Figure 5.1a. The appearance of the steep prejump repulsion is considered to be typical of the presence of nanobubbles and is attributed to the electrostatic double layer repulsion between the negatively charged bubble and silica surfaces [6, 11, 12, 14, 15, 21, 22]. After the probe jumped into contact, there was a soft compliance region at a distance of 3 - 5 nm before the hard-wall contact was made, as indicated by the arrow in Figure 5.1a. This behavior has been rationalized by the lateral spreading of submicroscopic bubbles and the compression of gas entrapped within the bubbles [6, 11, 12, 14, 15, 21].

Figure 5.1b shows the force curves between a hydrophilic silica sphere and a hydrophobic glass plate ( $\theta = 113^\circ$ ) during approach and retraction, respectively. The retraction curve exhibited strong and long-range adhesive behavior. The surfaces jumped apart from contact to a large distance of  $\sim 220$  nm, and the measured pull-off force was  $201 \pm 11$  mN/m. A rough estimate of the capillary force arising from bubble bridging for asymmetric surfaces can be obtained from the following equation [9].

$$\frac{F_c}{R} = 2\pi\gamma(\cos\theta_1 + \cos\theta_2) \quad (5.1)$$

Here,  $\theta_1 (= 5^\circ)$  and  $\theta_2 (= 113^\circ)$  are the water contact angles of the two interacting surfaces, respectively, and  $\gamma (= 72.05 \text{ mN/m})$  is the air-water interfacial tension. The capillary force was estimated to be 274 mN/m, which was similar to the experimentally measured value. On the other hand, the van der Waals force ( $F_{VW}$ ) between a silica sphere and a glass plate can be calculated from the following equation,

$$\frac{F_{VW}}{R} = -\frac{H_A}{6D_0^2} \quad (5.2)$$

where  $H_A$  is the Hamaker constant and  $D_0$  is contact separation ( $= 2 \text{ \AA}$ ) [24]. The van der Waals adhesive force was predicted to be 30 mN/m by using the Hamaker constant of  $7.1 \times 10^{-21} \text{ J}$  for the asymmetric surfaces across water. (This value was calculated from the Lifshitz theory using the medium properties given in Chapter 4, with a consideration that the thin OTS layer increases  $H_A$  by about 10 %). This result strongly suggests that the interaction for the present system was governed by a capillary force originating from nanobubble bridging, and not by van der Waals attraction between the silica surfaces. In addition, a step was also found at a large separation distance in the force curve upon retraction, as indicated by the arrow in Figure 5.1b, which has been interpreted as the rupture of the bridging bubbles [5, 6, 8, 11, 12, 15, 20].

In cases where a sudden jump to contact occurs, the jump-in distance can be taken as a relative measure of the magnitude of attraction [25, 26]. The measured jump-in distance, and hence the strength and range of the attractive force, increased sharply with the water contact angle of the hydrophobic surface, which was in qualitative agreement with the observation by other authors who found that the attractive force increased remarkably with contact angle above  $90^\circ$  [5, 16, 23, 27]. A drastic increase in the attraction in a rather narrow range of  $\theta = 106 - 113^\circ$  implies that there might be another factor affecting the long-range hydrophobic attraction, in addition to the water contact angle [16, 27, 28].



The role of the morphological characteristics of the surface in the strength and range of the hydrophobic force has been investigated by several authors [9, 18, 28-31]. Ederth et al. and Nalaskowski et al. claimed that the nature of long-range interaction  $> 20$  nm attributable to the bridging of nanobubbles was related more to the surface roughness than to the surface hydrophobicity estimated by the contact angle [28, 29]. Serro et al. also suggested that these interactions depend strongly on the surface topography, by its influence on formation of nanobubbles near surface defects in non-wetting liquids, which was confirmed with AFM imaging [9]. In fact, Wood et al. observed no evidence for long-range attraction between relatively defect-free surfaces hydrophobized by OTS [30, 31].

In an attempt to understand the effect of the surface topography on the hydrophobic interactions, AFM images of the glass plates, hydrophobized by different immersion times in OTS solution are illustrated in Figure 5.2. The values of the roughness and water contact angle of the OTS-coated glass surfaces, as well as the measured jump-in distance for their asymmetric interaction with a hydrophilic silica particle in water, are presented in Table 5.1.

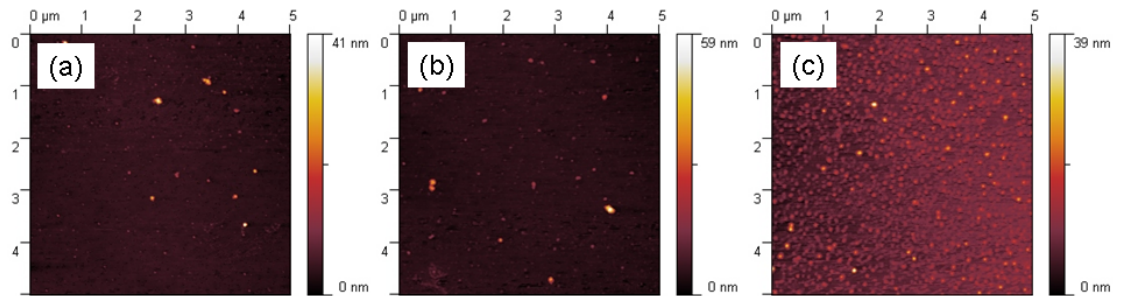


Figure 5.2: AFM topographic images ( $5.0 \times 5.0 \mu\text{m}^2$ ) of OTS-coated glass plates silanated with various immersion times: (a) 5 min ( $\theta = 106^\circ$ ), (b) 10 min ( $\theta = 111^\circ$ ) and (c) 60 min ( $\theta = 113^\circ$ ).

Table 5.1: Surface roughness ( $Ra$  and  $Rms$ ) and water contact angles ( $\theta$ ) of OTS-coated glass surfaces silanated with various immersion times ( $t$ ), and jump distances ( $D_j$ ) of a hydrophilic silica probe onto the OTS-coated surfaces in DI water.

$t$ (min)	Roughness		$\theta$ (°)	$D_j$ (nm)
	$Ra$ (nm)	$Rms$ (nm)		
5	$0.6 \pm 0.1$	$1.3 \pm 0.3$	$106.2 \pm 0.8$	$27.8 \pm 3.2$
10	$0.8 \pm 0.1$	$1.8 \pm 0.3$	$110.6 \pm 0.6$	$33.5 \pm 4.4$
60	$2.0 \pm 0.1$	$2.8 \pm 0.4$	$113.3 \pm 0.7$	$50.3 \pm 8.5$

*Note.* Roughness and water contact angle data are averages of 3 and 10 measurements, respectively. Uncertainty is 99 % confidence interval.

The AFM images show that the adsorption of OTS molecules resulted in the formation of molecular clusters [16], whose size remained relatively constant over the range of contact angle in the present study. The water contact angle increased slightly with increasing immersion time from 5 to 60 min, while the surface coverage of the OTS domains, and hence the surface roughness, increased by about 2X. Comparing the change in surface roughness with the jump-in distance, the sharp increase in the strength and range of attraction appears to be correlated to the increase in surface roughness. Thermodynamically, the formation and stability of submicroscopic gas bubbles at solid-liquid interfaces is known to be controlled by the surface roughness and heterogeneities [9, 18, 32]. Hence, it is reasonable to postulate that the increased number of OTS domains, and thus increased surface roughness, promoted the formation of gas bubbles by providing surface geometric defects and heterogeneities where gas bubbles could be trapped, resulting in stronger and longer-ranged attraction [9, 18, 28].

### 5.4.2 Hydrophilic Silica-Hydrophobic Silica Interactions in NMP-Water Binary

#### Mixtures

Figure 5.3 illustrates the approach force-distance curves between a hydrophilic silica sphere and an OTS-coated hydrophobic glass surface (water contact angle = 113 °) in NMP-water mixtures as a function of NMP concentration.

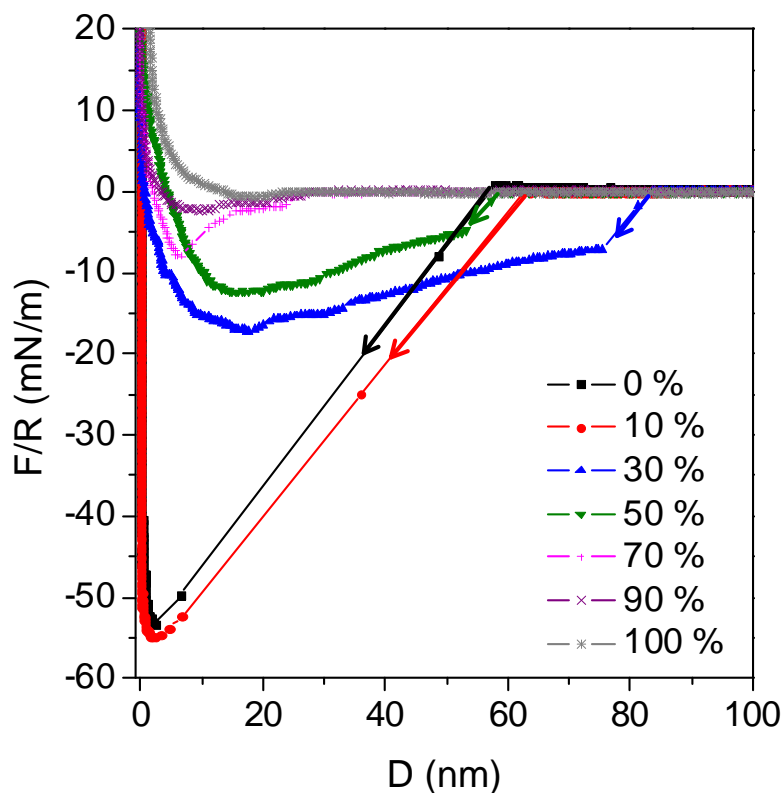


Figure 5.3: Force ( $F/R$ ) - separation ( $D$ ) curves for a hydrophilic silica sphere and an OTS-coated glass plate (water contact angle = 113°) during approach in NMP-water mixtures at various NMP concentrations (vol.%)

A strong and long-range attractive force similar to that seen in pure water was observed at 10 vol.% NMP. The probe jumped into contact at a distance of  $55 \pm 4$  nm. However, the force curve was drastically changed at 30 vol.% NMP. The range of the attractive force extended further to  $75 \pm 5$  nm, where a discontinuous step from zero to a finite value of the force appeared. Then, the force decreased gradually with a decrease in

separation and reached to the maximum attraction, followed by a soft compliance at a separation of  $\sim 15$  nm prior to hard-wall contact. This extended soft compliance region was observed in 30 - 50 vol.% NMP. Beyond 30 vol.% NMP, the range of attraction began to decrease with increasing NMP content, and finally, no long-range attraction was observed beyond 70 vol.% NMP. On the other hand, the maximum attraction strength decreased continuously with NMP composition without exhibiting a maximum.

Figure 5.4 shows the retraction force curves for the asymmetric surfaces in NMP-water mixtures as a function of NMP composition.

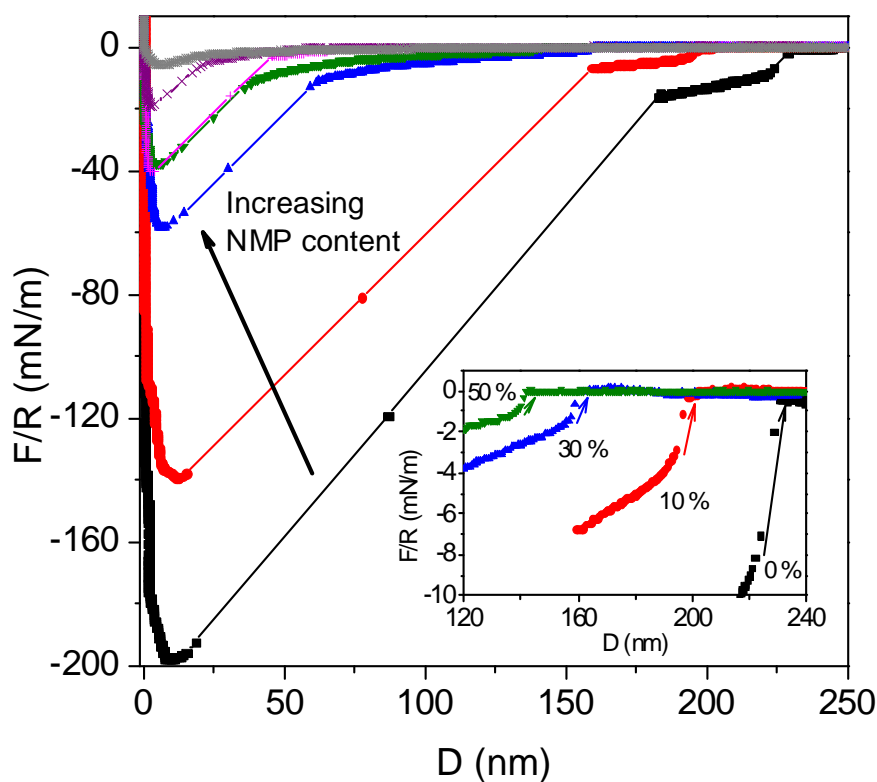


Figure 5.4: Force ( $F/R$ ) - separation ( $D$ ) curves for a hydrophilic silica sphere and an OTS-coated glass plate (water contact angle =  $113^\circ$ ) during retraction in NMP-water mixtures at various NMP concentrations (vol.%). (The arrow in the inset indicates a jump at a large separation during retraction).

It was found that both jump-out distance and pull-off force decreased continuously with increasing NMP concentration like the trend of the maximum attainable attraction seen in Figure 5.3. Although a stepped profile was observed at large separation for 0 - 50 vol.% NMP solution, indicative of the collapse of bridging bubbles [6, 8, 11, 12, 20, 33], the step size decreased with increasing NMP concentration (shown in the inset of Figure 5.4). These findings suggest that the solvophobic attraction arising from the bridging of submicroscopic bubbles in water was reduced by the addition of NMP.

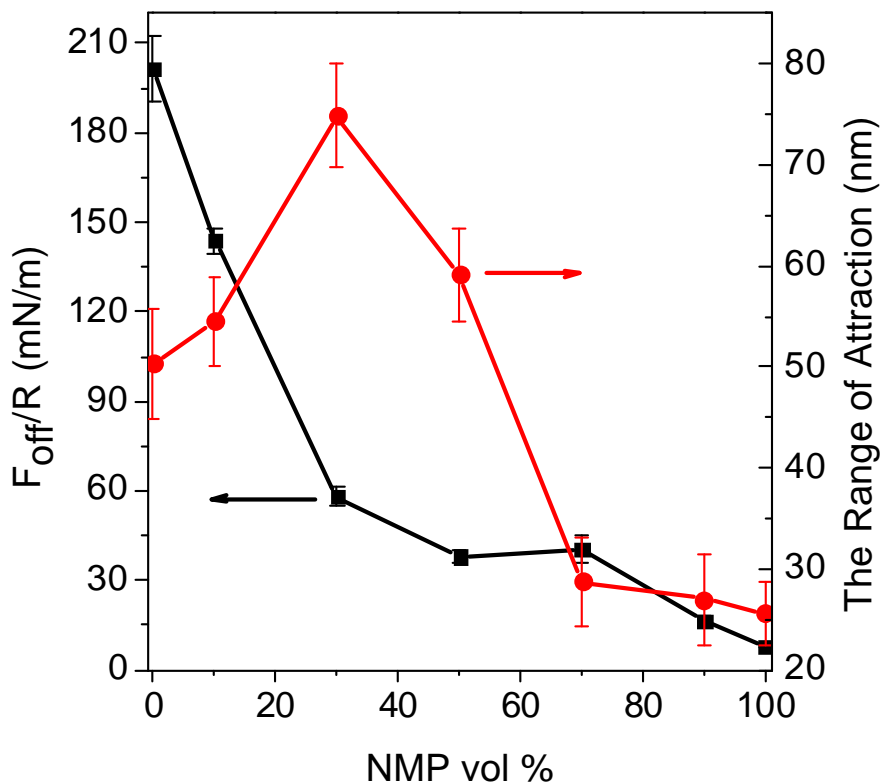


Figure 5.5: Pull-off force ( $F_{off}/R$ ) and the range of attraction between a hydrophilic silica sphere and an OTS-coated glass plate (water contact angle =  $113^\circ$ ) in a NMP-water mixture at various NMP concentrations (vol.%).

The pull-off forces and the range of attraction are plotted as a function of NMP vol.% in Figure 5.5. The measured pull-off force decreased with NMP content, while the

range of attraction exhibited a maximum at 30 vol.% NMP, implying that the mechanism governing the pull-off force was different from that governing the attractive force.

The addition of solvent can alter the solvophobic force by changing the wettability of the surfaces as well as medium properties [25, 26, 34]. The solution liquid-vapor surface tension and contact angle on the hydrophobic glass surface are plotted as a function of NMP composition in Figure 5.6.

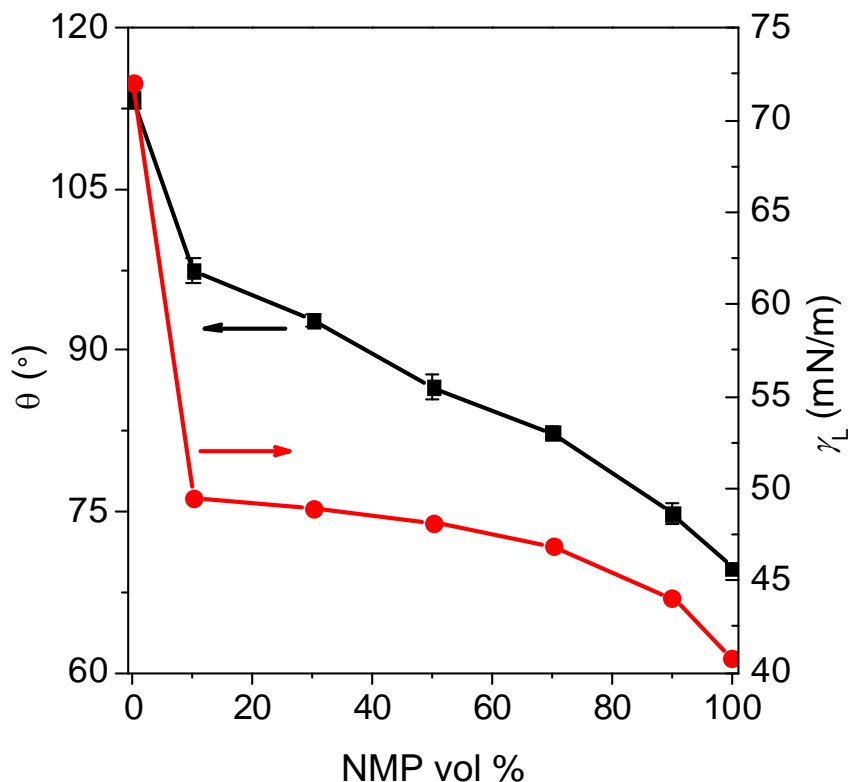


Figure 5.6: The contact angle ( $\theta$ ) on an OTS-coated hydrophobic glass plate and liquid-vapor surface tension ( $\gamma_L$ ) of a NMP-water mixture solution at various NMP concentrations (vol.%).

Both surface tension and contact angle decreased as the NMP concentration increased. Hence, the reduction in the contact angle was due primarily to the accumulation of NMP molecules at the air-liquid interface [25, 35]. It is important to note that the hydrophobized glass surface did not show a maximum in the solution

contact angle resulting from the increased solid-liquid interfacial tension, which was observed for a hydrophilic glass surface.

Theoretical considerations predict that the capillary attractive force originating from bridging of submicroscopic bubbles is proportional to the liquid-vapor surface tension of the solution [13, 18]. Hence, the addition of NMP to water reduces the solvophobic attractive force by decreasing the liquid-vapor surface tension of the solution. On the other hand, the reduction in the solution contact angle on the hydrophobic surface, due to the presence of NMP predicts that the hydrophobic surface becomes less solvophobic with an expected decrease in the magnitude of the attractive force, as NMP concentration increases. In fact, the measured pull-off force decreased with solution liquid-vapor surface tension and contact angle, as a function of the NMP concentration. Similarly, a decrease in the step size observed at a large separation (in the retraction force curve) with NMP content can be explained by the known decrease in the number and size of stable nanobubbles with increasing the wettability of the surface [9, 12].

To confirm the effect of the wettability of the hydrophobic surface on the adhesive force, the measured pull-off forces were compared to the contact angle ( $\theta$ ) of the OTS-coated glass substrate and to the predicted van der Waals force ( $F_{vw}$ ), as illustrated in Figure 5.7a. The pull-off force increased gradually when  $\theta$  was smaller than  $90^\circ$ , and it increased sharply with  $\theta$  and overwhelmed the predicted van der Waals force when  $\theta$  exceeded  $90^\circ$ . This indicates that the measured pull-off force for surfaces having  $\theta > 90^\circ$  appears to be governed predominantly by the solvophobic force resulting from nanobubble bridging, which is in qualitative agreement with results reported by Considine et al. for symmetric solvophobic interactions between two hydrophobic surfaces [34]. They found that the solvophobic force increased markedly with the contact angle when the advancing contact angle of the liquid medium was above  $80^\circ$ , and interpreted this observation in terms of the bubble bridging mechanism [34]. It is

noteworthy that the adhesion behavior for the asymmetric solvophobic system was qualitatively similar to that for the symmetric cases.

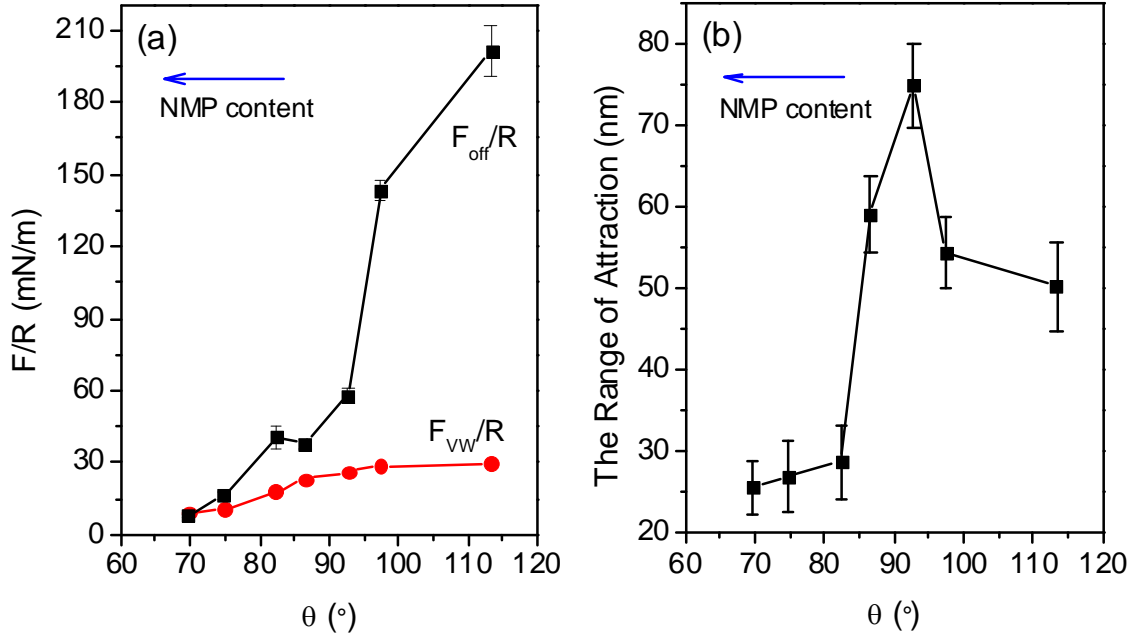


Figure 5.7: Correlation of the contact angle ( $\theta$ ) on the OTS-coated hydrophobic glass plate of a NMP-water mixture solution to (a) the pull-off force ( $F_{off}/R$ ) (The predicted van der Waals force ( $F_{vw}/R$ ) was calculated by using equation 5.2. Nonretarded Hamaker constants were calculated from the Lifshitz theory using the medium properties given in Chapter 4. The presence of the thin OTS layer was considered to increase the van der Waals force by about 10 %). (b) the range of attraction between a hydrophilic silica sphere and an OTS-coated glass plate in a NMP-water mixture at various NMP concentrations, respectively.

While the adhesive pull-off force was correlated strongly with the wettability of the surface, there appeared to be no well-defined correlation between the contact angle and the separation at which the long-range attraction occurred during approach, as illustrated in Figure 5.7b. The attractive range in the asymmetric case behaved similarly to two hydrophilic surfaces in NMP-water mixture: The attractive range exhibited a



maximum value for 30 vol.% NMP. However, we note that here the range for asymmetric surfaces showed a higher value for the water-rich medium (0 - 10 vol.% NMP), compared to the symmetric surfaces. This enables us to speculate that the range of attraction is not determined solely by the wettability of the hydrophobic surface, but that the structural change in liquid ordering near on the hydrophilic surface may also affect the overall range of attraction, as described in Chapter 4.

It is difficult to analyze quantitatively the range of the solvophobic attractive force, because the size and stability of surface-adherent bubbles are influenced by the change in solution physical properties as well as the wettability of the surface [18, 34]. Nevertheless, the qualitative explanation can be made as follows. The structural characteristics of both surfaces are involved in the mechanism governing the overall attraction for the asymmetric case: One characteristic is the macrocluster-like surface adsorption layer formed on the hydrophilic silica surface, and the other is the submicroscopic bubbles on the hydrophobic glass surface. The attraction observed between the surfaces in NMP-water mixtures is likely a result of the contact of the surface-adherent nanobubbles on the hydrophobic surface with the surface adsorption layer on the hydrophilic surface. Under this circumstance, the overall range of attractive force could be determined by the size of the preexisting submicroscopic bubble and the thickness of the surface adsorption layer on each surface, respectively. The size and number of stable submicroscopic bubbles on the hydrophobic surface are expected to decrease, leading to a decrease in the solvophobic attraction with increasing NMP concentration, as mentioned above. On the other hand, the selective surface adsorption layer might be induced on the hydrophilic surface with its thickness being maximized to be about 36 nm at 30 vol.% NMP and being reduced with NMP concentration beyond 30 vol.% NMP, as discussed in Chapter 4. The abrupt jump-into contact at large separation observed in the water-rich medium (0 - 10 vol.% NMP) would be attributable to the predominant solvophobic force arising from the instantaneous bridging of nanobubbles

on the hydrophobic surface. At 30 vol.% NMP, nanobubbles could still exist on the OTS layer-liquid interface, although their size and number might slightly decrease due to a minor increase in wettability of the surface [9, 12]. On the other hand, the thickness of the surface macrocluster layer on the hydrophilic surface would be maximized. As the surfaces approach, the surface-adherent nanobubbles contact with the thick surface adsorption layer on the other surface and coalesce gradually to form a bubble bridge. Hence, the maximized range of the attraction at 30 vol.% NMP probably reflects the increased thickness of the surface adsorption layer on the hydrophilic silica surface. The formation of bubble bridges at surface contact is supported by the dependence of pull-off force on solution liquid-vapor surface tension and contact angle on the hydrophobic surface, as well as the observation of a step at large separation in the retraction curve. The bubble bridging process occurring in NMP-water mixtures appears to be not as abrupt as that in the water-rich liquid, due to the presence of the thick and relatively soft liquid adsorption layer. In fact, the approach force profile measured for 30 - 50 vol.% NMP was characterized with an initial jump and a subsequent gradual increase in the attraction and an extended soft compliance regime. These are likely associated with the “squeezing out” of the surface adsorption layer as well as the compression of gas within bridging bubbles [12, 34]. A further increase in NMP concentration beyond 30 vol.% NMP is expected to reduce both the size and number of the submicroscopic bubbles and the thickness of adsorption layer with a decrease in the overall range of attractive force: The range of attractive force was reduced at 50 vol.% NMP, although the shape of the force profile was similar to that for 30 vol.% NMP. Beyond 50 vol.% NMP, the range of attractive force was significantly reduced, as expected.

For the magnitude of the maximum attainable attraction observed in the approach curve, it decreased continuously with increasing NMP concentration, which was similar trend to that of the pull-off force. This suggests that the origin of the ultimate attraction might come from the capillary force arising from nanobubble bridging after contact of the

adsorption layer and the nanobubbles although the adsorption layer could affect the range of attraction. It can be concluded that the maximum attraction upon approach together with the pull-off force upon retraction was governed predominantly by the solvophobic force related to the wetting property and nanobubble formation of the hydrophobic surface, although the van der Waals force, in part, was involved.

## 5.5. CONCLUSIONS

In this chapter, the interactions between asymmetric silica surfaces in NMP-water mixtures were investigated using the silica probe AFM technique. A strong and long-range attraction was observed in pure water. The strength and range of the attractive force were markedly affected by the roughness of the hydrophobic surface. The characteristic force curves such as jumps and discontinuities in the approach and retract curve and steep pre-jump repulsion strongly suggested the presence of the strong hydrophobic force arising from the bridging of nanobubbles existing on the hydrophobic surface.

For the asymmetric surfaces in NMP-water mixtures, the combination of two different non-DLVO forces appeared to play a role in the overall interaction: (1) the solvophobic force resulting from the bridging of submicroscopic bubbles on the hydrophobic surface and (2) the structural force originating from the surface adsorption layer on the hydrophilic surface. The pull-off force and maximum attainable attractive force decreased continuously with increasing NMP concentration, and they were well correlated with the solution contact angle on the hydrophobic force. Hence, it was plausible to assume that the pull-off adhesive force and ultimate attractive force was predominantly controlled by the solvophobic forces based on the wettability of the hydrophobic surfaces and the nanobubble formation on the surface. In contrary, the range of attraction exhibited the maximum at around 30 vol.% NMP, which was presumably attributed mainly to the presence of the thickest surface macrocluster layer

induced on the hydrophilic surface and its contact with the surface-adherent nanobubbles on the hydrophobic surface.

## 5.6. REFERENCES

1. Husain, S. and W.J. Koros, *J. Membr. Sci.*, 2007. **288**(1-2): p. 195-207.
2. Mahajan, R. and W.J. Koros, *Ind. Eng. Chem. Res.*, 2000. **39**(8): p. 2692-2696.
3. Duval, J.M., A.J.B. Kemperman, B. Folkers, M.H.V. Mulder, G. Desgrandchamps, and C.A. Smolders, *J. App. Polym. Sci.*, 1994. **54**(4): p. 409-418.
4. Mahajan, R. and W.J. Koros, *Polym. Eng. Sci.*, 2002. **42**(7): p. 1420-1431.
5. Ishida, N., N. Kinoshita, M. Miyahara, and K. Higashitani, *J. Colloid Interface Sci.*, 1999. **216**(2): p. 387-393.
6. Carambassis, A., L.C. Jonker, P. Attard, and M.W. Rutland, *Phys. Rev. Lett.*, 1998. **80**(24): p. 5357-5360.
7. Ishida, N., T. Inoue, M. Miyahara, and K. Higashitani, *Langmuir*, 2000. **16**(16): p. 6377-6380.
8. Ishida, N., M. Sakamoto, M. Miyahara, and K. Higashitani, *Langmuir*, 2000. **16**(13): p. 5681-5687.
9. Serro, A.P., R. Colaco, and B. Saramago, *J. Colloid Interface Sci.*, 2008. **325**(2): p. 573-579.
10. Meyer, E.E., K.J. Rosenberg, and J. Israelachvili, *Proc. Natl. Acad. Sci. USA*, 2006. **103**(43): p. 15739-15746.
11. Tyrrell, J.W.G. and P. Attard, *Phys. Rev. Lett.*, 2001. **87**(17): p. 176104.
12. Tyrrell, J.W.G. and P. Attard, *Langmuir*, 2002. **18**(1): p. 160-167.

13. Attard, P., Langmuir, 1996. **12**(6): p. 1693-1695.
14. Attard, P., Langmuir, 2000. **16**(10): p. 4455-4466.
15. Attard, P., Adv. Colloid Interface Sci., 2003. **104**: p. 75-91.
16. Rabinovich, Y.I. and R.H. Yoon, Colloids Surf. A, 1994. **93**: p. 263-273.
17. Christenson, H.K. and P.M. Claesson, Adv. Colloid Interface Sci., 2001. **91**: p. 391-436.
18. Nguyen, A.V., J. Nalaskowski, J.D. Miller, and H.J. Butt, Int. J. Mineral Proc., 2003. **72**(1-4): p. 215-225.
19. Parker, J.L. and P.M. Claesson, Langmuir, 1994. **10**(3): p. 635-639.
20. Parker, J.L., P.M. Claesson, and P. Attard, J. Phys. Chem., 1994. **98**(34): p. 8468-8480.
21. Stevens, H., R.F. Considine, C.J. Drummond, R.A. Hayes, and P. Attard, Langmuir, 2005. **21**(14): p. 6399-6405.
22. Ducker, W.A., Z.G. Xu, and J.N. Israelachvili, Langmuir, 1994. **10**(9): p. 3279-3289.
23. Yoon, R.H., D.H. Flinn, and Y.I. Rabinovich, J. Colloid Interface Sci., 1997. **185**(2): p. 363-370.
24. Lim, R. and S.J. O'Shea, Phys. Rev. Lett., 2002. **88**(24): p. 246101.
25. Kokkoli, E. and C.F. Zukoski, J. Colloid Interface Sci., 1999. **209**(1): p. 60-65.
26. Kokkoli, E. and C.F. Zukoski, Langmuir, 1998. **14**(5): p. 1189-1195.
27. Rabinovich, Y.I. and R.H. Yoon, Langmuir, 1994. **10**(6): p. 1903-1909.

28. Nalaskowski, J., S. Veeramasuneni, J. Hupka, and J.D. Miller, J. Adhes. Sci. Technol., 1999. **13**(12): p. 1519-1533.
29. Ederth, T. and B. Liedberg, Langmuir, 2000. **16**(5): p. 2177-2184.
30. Wood, J. and R. Sharma, Langmuir, 1995. **11**(12): p. 4797-4802.
31. Wood, J. and R. Sharma, J. Adhes. Sci. Technol., 1995. **9**(8): p. 1075-1085.
32. Ryan, W.L. and E.A. Hemmingsen, J. Colloid Interface Sci., 1993. **157**(2): p. 312-317.
33. Papastavrou, G., S. Akari, and H. Mohwald, Europhys. Lett., 2000. **52**(5): p. 551-556.
34. Considine, R.F. and C.J. Drummond, Langmuir, 2000. **16**(2): p. 631-635.
35. Garcia-Abuin, A., D. Gomez-Diaz, J.M. Navaza, and I. Vidal-Tato, J. Chem. Eng. Data, 2008. **53**(11): p. 2671-2674.

## **CHAPTER 6**

### **CHARACTERIZATION OF ZEOLITE (MFI)/POLYMER COMPOSITE PROPERTIES**

The nature of the particle-polymer interface strongly influences the mechanical, thermal and structural properties by altering the structure and dynamics of the polymer matrix near the filler surface [1-3]. In particular, both mechanical (strength) and transport (selectivity) properties may be affected by the presence of defects in the composites. Furthermore, the polymer properties can be affected profoundly by the thermo-mechanical history during membrane fabrication [4]. Hence, questions arise as to how zeolite surface modification (Grignard or solvothermal treatment) influences the interfacial, mechanical, and transport properties' dependence on thermal history. Knowledge of the roughening effect of the particle surfaces on interfacial and physical properties of composites would allow better design of surface treatments.

#### **6.1. OVERVIEW**

Mg(OH)<sub>2</sub> inorganic whisker- or asperity-like nanostructures were achieved on pure-silica MFI nano- and micro-particle surfaces via Grignard (GT) or solvothermal treatment (ST). The interfacial, mechanical, and thermal properties of neat polymers (Ultem<sup>®</sup> 1000 and PVAc) and their composites with untreated and surface-modified MFI particles used in the AFM studies were characterized under different annealing conditions. The creation of nano-roughness on the MFI surface promoted compatibility between the zeolite and the polymer matrix, resulting in void-free interfaces. Mechanical properties (tensile strength and elongation at break) of Ultem based films showed no difference with or without zeolite surface modification. In contrast, PVAc composites containing surface-

modified particles exhibited increased tensile strength and elongation at break as compared with composites containing unmodified zeolite. Surface modification of the microparticles exhibited interfacial and mechanical enhancement over a wider range of annealing temperatures than nanoparticles. Differential scanning calorimetry (DSC) revealed that surface-treatment of MFI resulted in broader glass transitions compared to PVAc composites containing unmodified MFI. This is explained by improved interfacial adhesion and associated slower chain relaxation dynamics. Furthermore, X-ray diffraction (XRD) demonstrated that enhanced adhesive interactions between the PVAc and the MFI surface are associated with surface-induced orientation of the MFI particles within the polymer matrix. The optimal surface morphology, associated with the most enhanced mechanical and thermal properties of the composites, was produced with the solvothermal method.

## **6.2. EXPERIMENTAL**

### **6.2.1. Materials and Procedure**

#### **6.2.1.1. Materials**

##### *6.2.1.1.1. Chemicals*

The following chemicals were used as received: poly(vinyl acetate) (PVAc,  $M_w$  = 500,000 g/mol, Sigma-Aldrich), Ultem<sup>®</sup> 1000 (GE Plastics), tetraethylorthosilicate (TEOS, 98 % Sigma-Aldrich), tetrapropylammonium hydroxide (TPAOH, 40 % w/w aqueous solution, Alfa Aesar), tetrapropylammonium bromide (TPABr, 98 %, Sigma-Aldrich), ethylenediamine (EDA, 99 %, Sigma-Aldrich), methylmagnesium bromide (3 M in ether, Sigma-Aldrich), 2-propanol (Sigma-Aldrich), dichloromethane (DCM, 99.5 %, Sigma-Aldrich), toluene (99.8 %, Sigma-Aldrich), magnesium sulfate heptahydrate (Acros) and sodium chloride (NaCl, Fisher Scientific).



#### 6.2.1.1.2. Pure-Silica MFI Particles

Pure-silica MFI nanoparticles (nMFIs) were synthesized hydrothermally from TEOS/TPAOH/water solutions. The solution with molar ratio of 1TEOS/0.24TPAOH/360H<sub>2</sub>O was stirred at room temperature for 24 h and hydrothermally crystallized at 150 °C for 4 days. Large MFI microparticles ( $\mu$ MFI) were also prepared using the method described in the literature [5]. The solution with molar ratio of 1 TEOS:0.1 TPABr:0.1 NaOH:98 H<sub>2</sub>O was aged at 50 °C for 7 days and crystallized at 120 °C for 2 days. The synthesized zeolite particles were then washed with DI water via at least five centrifugation cycles, followed by drying at 80 °C. The particles were calcinated at 550 °C for 8 h in air.

#### 6.2.1.1.3. Surface-Modified MFI Particles

**Grignard Treatment (GT):** Grignard treatment was performed after seeding the zeolite surfaces with NaCl. 0.5 g of MFI particles was dispersed in 3 M aqueous NaCl solution. The suspension was filtered using a microfiltration membrane with 0.1  $\mu$ m pores. The collected particles were then dried at 80 °C for 12 h to remove some of the residual water. The NaCl seeded particles were placed in round bottom flask, followed by the addition of 8 ml of toluene. After purging the flask with nitrogen 1.5 ml of 3 M CH<sub>3</sub>MgBr in ether was added using transfer needles. The suspension was sonicated at 20 kHz for 4 h and then stirred at room temperature under nitrogen for 12 h. 2-propanol was added drop-wise to quench the Grignard reagent and the mixture was centrifuged to collect the particles. To remove residual solvents, the particles were washed with 2-propanol several times. After that, 40 ml of DI water was added to the particles and the mixture was sonicated at 20 kHz for 2 h. The particles were washed with DI water via several cycles of centrifugation and dispersion, followed by drying at 80 °C.

***Solvothermal Treatment (ST):*** The deposition of  $\text{Mg}(\text{OH})_2$  was performed in the solvent mixture of EDA and a  $\text{MgSO}_4$  aqueous solution at high temperature. 0.2 g of zeolites was dispersed in 10 ml of EDA by sonication, followed by the drop-wise addition of 1 ml of 1 M aqueous  $\text{MgSO}_4$  solution under vigorous stirring. After further stirring for 1 h, the mixture was transferred to Teflon-lined autoclave and solvothermal treatment was performed at 160 °C in the oven for 12 h. The particles were washed with DI water via several centrifugation cycles and dried at 80 °C. The amount of  $\text{Mg}(\text{OH})_2$  in final products was controlled by adjusting  $\text{MgSO}_4$  concentration in the aqueous solution. The detailed procedure was described in the literature [5].

#### ***6.2.1.2. Composite Film Preparation***

Unmodified and surface-treated MFI zeolites were dried in a vacuum oven at 140 °C for 24 h. The proper amounts of dried particles (to form 1, 2.5, 5, and 10 vol.% MFI loaded films) were dispersed in DCM by stirring for 24 h, followed by bath and horn type sonication at 42 kHz for 20 min and at 20 kHz for 1 min, respectively. Sonication procedures were repeated at least 3 times to ensure a uniform dispersion of zeolite particles in the solvent. The desired amount of dried polymer (PVAc or Ultem<sup>®</sup> 1000) was added to the zeolite suspensions, and then the mixtures were agitated using a rotational shaker for 48 h. The composite films were prepared by casting the solution mixtures with a blade on OTS (Octadecyltrichlorosilane)-treated glass substrates for PVAc films and plain glass substrates for Ultem films, respectively, and slowly dried under a solvent (DCM) saturated environment for 24 h. The films were subsequently dried at room temperature for 7 days, and free standing films were obtained by carefully peeling films from the glass using a razor. Finally, composite films were annealed in a vacuum oven at either 20, 40, or 100 °C for PVAc films, and either 150 or 230 °C for Ultem films, respectively, for 24 h. All samples were slowly cooled down to room temperature at ~ 6 °C/h cooling rate. The thickness at various positions on the films was

measured by a micrometer (Mitutoyo Corp., model C112CEB). For each film, 25 measurements were performed within  $2.5 \times 2.0 \text{ cm}^2$  area of the film, and the average thickness was obtained. All the films used in this work had an average thickness of  $110 \pm 3 \text{ }\mu\text{m}$  for PVAc films, and  $80 \pm 5 \text{ }\mu\text{m}$  for Ultem films, respectively.

## **6.2.2. Experimental Methods**

### **6.2.2.1. MFI zeolite particles**

The mass fractions of  $\text{Mg}(\text{OH})_2$  in surface-modified MFI particles were estimated by DSC and thermogravimetric analysis (TGA) performed on a Netzsch STA409. A sharp endothermic peak in the range of  $370 - 430 \text{ }^\circ\text{C}$  appears in the DSC curve due to the dehydration of  $\text{Mg}(\text{OH})_2$  to  $\text{MgO}$ . The mass fraction of  $\text{Mg}(\text{OH})_2$  was calculated from the  $\text{H}_2\text{O}$  loss in this temperature region. The surface morphology and size of MFI crystals were determined using SEM (LEO 1530).

### **6.2.2.2. MFI/Polymer Composites**

Mechanical properties of polymer composite films were measured using a high-throughput impact and strain (HTMECH) apparatus [6-8]. A force sensor records the force-time profile for each of the 30 measurement points on a typical  $2.5 \times 2.0 \text{ cm}^2$  area of films. Each force-time profile was converted to strain-stress curve, and statistical mechanical properties of polymer composite films such as the tensile strength and elongation were obtained. All mechanical tests were performed at a constant strain rate ( $0.5 \text{ mm/s}$ ) under ambient conditions. To characterize the glass transition behavior of the PVAc composites, DSC measurements were performed with a TA instruments Q21 at a heating rate of  $5 \text{ }^\circ\text{C/min}$  over the temperature range of  $-10$  to  $120 \text{ }^\circ\text{C}$  in a nitrogen atmosphere. Specimens about  $4 \text{ mg}$  for DSC measurements were cut out from the films prepared above and sealed in aluminum pans with lids. Onset temperatures at points where the glass transition begins and ends, respectively, were measured and the width of

the glass transition,  $\Delta T$ , was determined as a difference of each onset temperature. The glass transition temperature ( $T_g$ ) was determined from the inflection point of the glass transition region of the samples which are annealed at 100 °C. The  $T_g$  value for pure PVAc was estimated to be around 45 °C. All thermal properties of the samples were measured from the first heating run. Prepared PVAc composite films were also characterized by XRD. XRD patterns were obtained on a Philips X'pert Pro powder diffractometer and a PW3011 proportional detector equipped with a parallel plate collimator ( $\text{CuK}\alpha$ ,  $\lambda = 1.5418 \text{ \AA}$ ). SEM was used to examine the interfacial morphology of MFI/polymer composites. Fracture surfaces of the composites containing 10 vol.% of untreated and surface-treated MFI were observed with a LEO 1530 instrument.

## 6.3. RESULTS AND DISCUSSION

### 6.3.1. Particle Modification

The surface morphology of untreated (UN) and surface-modified MFI nanoparticles (nMFIs) and microparticles ( $\mu$ MFIs), via Grignard (GT) or solvothermal treatment (ST), were compared using SEM images (Figures 6.1 and 6.2).

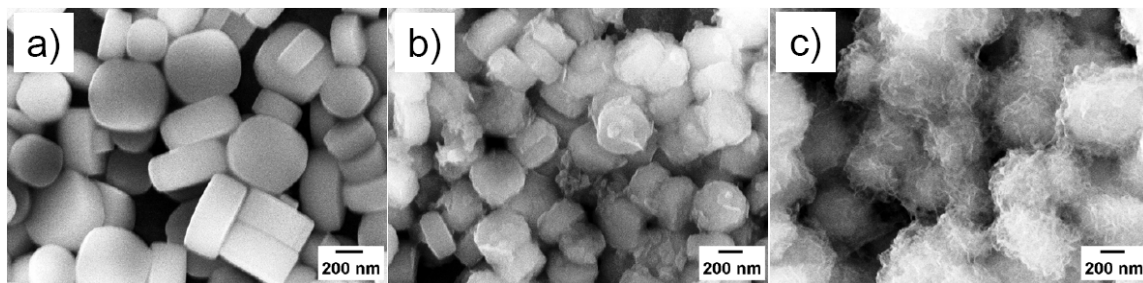


Figure 6.1: SEM images of untreated and surface-treated MFI nanoparticles (nMFI); (a) untreated (UN), (b) Grignard-treated (GT, 15 wt%  $\text{Mg}(\text{OH})_2$ ), and (c) Solvothermally-treated (ST, 20 wt%  $\text{Mg}(\text{OH})_2$ ).

Unmodified nMFIs show smooth surfaces, with uniform “rounded-cubic” shape and a size of around  $300 \times 300 \times 150 \text{ nm}^3$ . SEM images clearly show that the surface

roughness of nMFI was significantly altered by GT or ST method, by the formation of inorganic whisker- or asperity-like nanostructures. The surface nanostructures were identified as  $\text{Mg}(\text{OH})_2$  by energy-dispersive spectroscopy (EDS) and XRD, as reported in a previous study [5]. ST produced well-defined nano-whiskers on the nMFI surfaces with higher surface roughness, compared to GT, which was verified with external surface area analysis [5]. The length of the nano-whiskers is estimated to be around 70 nm from the SEM images, as shown in Figure 6.1. Their width appears to be 1 ~ 2 orders of magnitude smaller than the length scale, indicating high aspect ratio structures. The mass fractions of  $\text{Mg}(\text{OH})_2$  of GT- and ST-nMFI samples were determined to be approximately 15 and 20 wt%, respectively from DSC and TGA measurements.

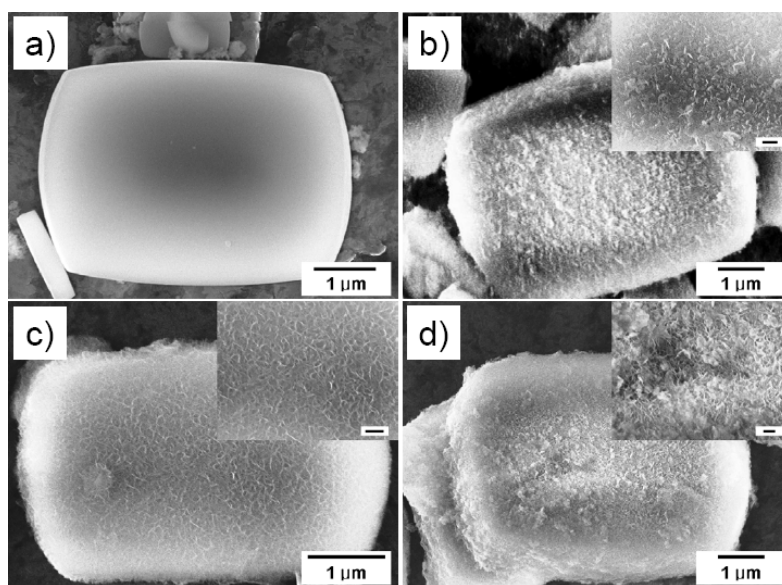


Figure 6.2: SEM images of untreated and surface-treated MFI microparticles ( $\mu\text{MFI}$ ); (a) untreated (UN), (b) Grignard-treated (GT, 5 wt%  $\text{Mg}(\text{OH})_2$ ), (c) Solvothermally-treated (ST, 5 wt%  $\text{Mg}(\text{OH})_2$ ), (d) Solvothermally-treated (HST, 20 wt%  $\text{Mg}(\text{OH})_2$ ). Scale bars in inset figures indicate 200 nm.

For the MFI microparticles ( $\mu\text{MFIs}$ ), untreated MFI crystals also have smooth surfaces with a “rounded-boat” shape, ranging in size from  $1 \times 0.5 \times 0.2 \mu\text{m}^3$  to  $5 \times 3.5 \times$

1  $\mu\text{m}^3$  with a broad size distribution. After GT or ST modification, well-defined surface nanostructures were formed on the  $\mu\text{MFI}$  surface, which provide a large planar surface for the nucleation and growth of the nanostructures. The GT method created roughened surface morphologies composed of whisker- and platelet-shaped nanocrystals, while ST led to uniform whisker-like structures ( $\sim 100$  nm in length) with high aspect ratio, as shown in Figure 6.2. The amount of  $\text{Mg}(\text{OH})_2$  in the GT and ST modified  $\mu\text{MFI}$  was estimated to be around 5 wt%. ST modified  $\mu\text{MFIs}$  with a higher amount of  $\text{Mg}(\text{OH})_2$  ( $\sim 20$  wt%) were also prepared, and these exhibit a denser nano-whisker morphology with increased roughness, compared to 5 wt%  $\text{Mg}(\text{OH})_2$  loaded (Figure 6.2d).

### **6.3.2. MFI/Polymer Composites**

#### **6.3.2.1. MFI/Ultem Composites**

##### *6.3.2.1.1. Morphology*

The morphology of MFI-Ultem interfaces in composites was studied by examining SEM images of fracture surfaces (shown in Figure 6.3). The interfaces were affected significantly by the surface morphology of MFI particles. Unmodified composites show dewetted interfaces with interfacial voids. This void formation at filler-polymer interfaces is presumably due to poor interfacial adhesion between the MFI surface and the Ultem, which was also confirmed by the AFM studies described in Chapter 3 [9]. In fact bare MFI adhesion to Ultem had the lowest adhesion with bare MFI ( $3.35 \pm 0.1$   $\mu\text{N}$ ) compared to all other polyimide materials examined, whereas PVAc had the highest adhesion ( $4.28 \pm 0.1$   $\mu\text{N}$ ). The incorporation of GT-nMFI reduced interfacial voids and resulted in a wetted MFI-Ultem interface, implying enhanced MFI-Ultem interfacial adhesion. This is in good agreement with the work of Shu et al., where nanowisker structures (physical roughness) on LTA zeolite surfaces enhanced interfacial adhesion between the zeolite and Ultem polymer and thus improve the mechanical and transport properties of composites [10]. It is well known that the entropy

penalty for polymer adsorption onto a rougher surface is lower because a polymer chain loses less configurational entropy to adsorb onto a rough surface as compared to the case of a smooth surface [10-12]. Hence, thermodynamically-induced adsorption (reduced entropy loss) and increased contact area were proposed to be possible reasons for enhancement in interfacial adhesion at the particle-polymer interfaces with nano-asperities [5, 10]. Furthermore, the improved interfacial adhesion by the GT surface modification correlates well with the AFM measurements shown in Chapter 3. In fact, the adhesion force of a Grignard-modified MFI particle with Ultem was about 2X higher than that of unmodified MFI.

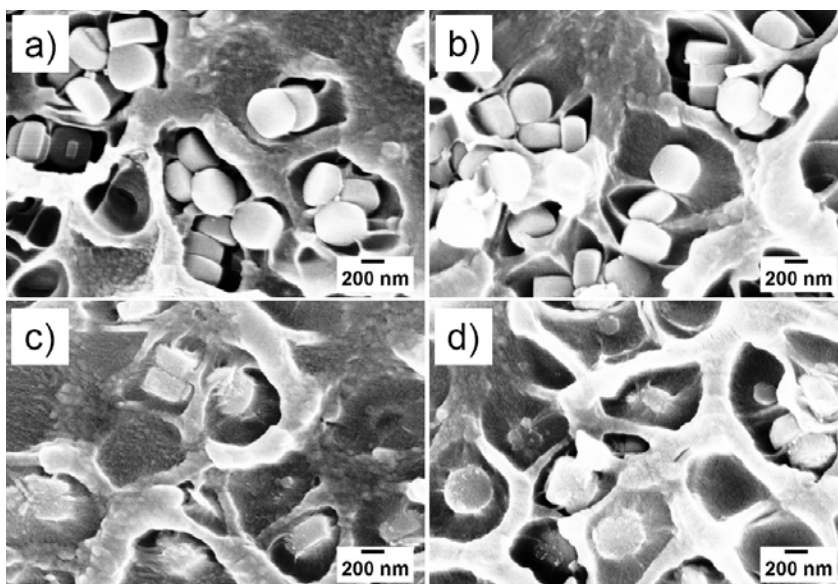


Figure 6.3: SEM images of Ultem composites containing 10 vol.% of untreated (UN) and Grignard-treated (GT) nMFI, which are annealed at 150 and 230 °C for 24 h, respectively: UN-nMFI (a) 150 °C and (b) 230 °C and GT-nMFI (c) 150 °C and (d) 230 °C.

#### 6.3.2.1.2. Mechanical Properties

Mechanical characterization of MFI/Ultem composites was performed to determine how mechanical properties were influenced by the presence of untreated or

surface-modified MFI particles. Mechanical properties (tensile strength and elongation) of Ultem composites decreased with addition of MFI zeolite, regardless of the surface treatment and annealing condition, as illustrated in Figure 6.4. Zeolite surface treatment had no observable effect on mechanical properties, despite the improved MFI-Ultem adhesion resulting from GT modification observed in SEM images and AFM studies (Chapter 3). It is possible that glassy Ultem polymer is mechanically too strong to allow detection of mechanical enhancement (improvement in load transfer efficiency) by improved filler-polymer interfacial adhesion.

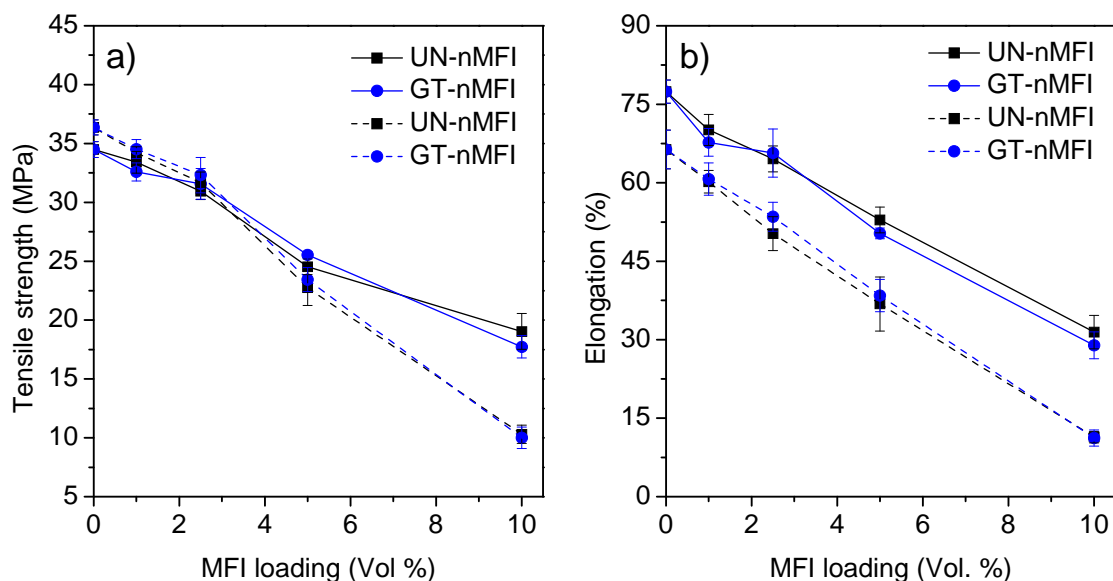


Figure 6.4: Mechanical properties (a) tensile strength and b) elongation at break of Ultem composites containing untreated (UN) and Grignard-treated (GT) nMFI as a function of MFI loading (1 – 10 vol.%) and annealing conditions (150 °C (solid line) and 230 °C (dot line) for 24 h, respectively).

### 6.3.2.2. MFI/PVAc Composites

In the following sections, rubbery and flexible PVAc was used as a model polymer to investigate the effect of polymer characteristics on the physical and mechanical enhancement of polymer composites by surface modifications.



#### 6.3.2.2.1. Morphology

The interfaces in PVAc composites were influenced by the surface morphology (roughness) of MFI particles as well as film annealing conditions. Figures 6.5 and 6.6 show SEM images of fracture surfaces of PVAc composites containing 10 vol.% of untreated and surface-modified particles for nMFI (Figure 6.5) and  $\mu$ MFI (Figure 6.6), respectively.

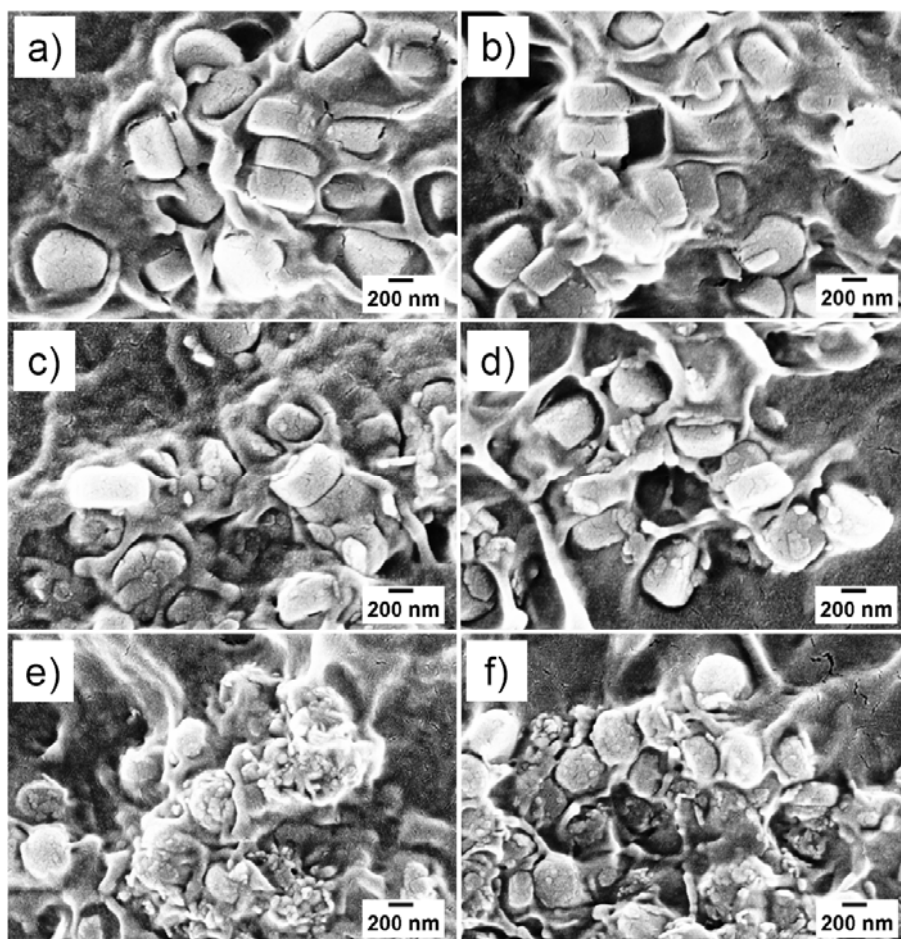


Figure 6.5: SEM images of PVAc composites containing 10 vol.% of untreated (UN) and surface-treated (GT and ST) nMFI, which are annealed at 20 and 100 °C for 24 h, respectively: UN (a) 20 °C and (b) 100 °C, GT (c) 20 °C and (d) 100 °C, and ST (e) 20 °C and (f) 100 °C.

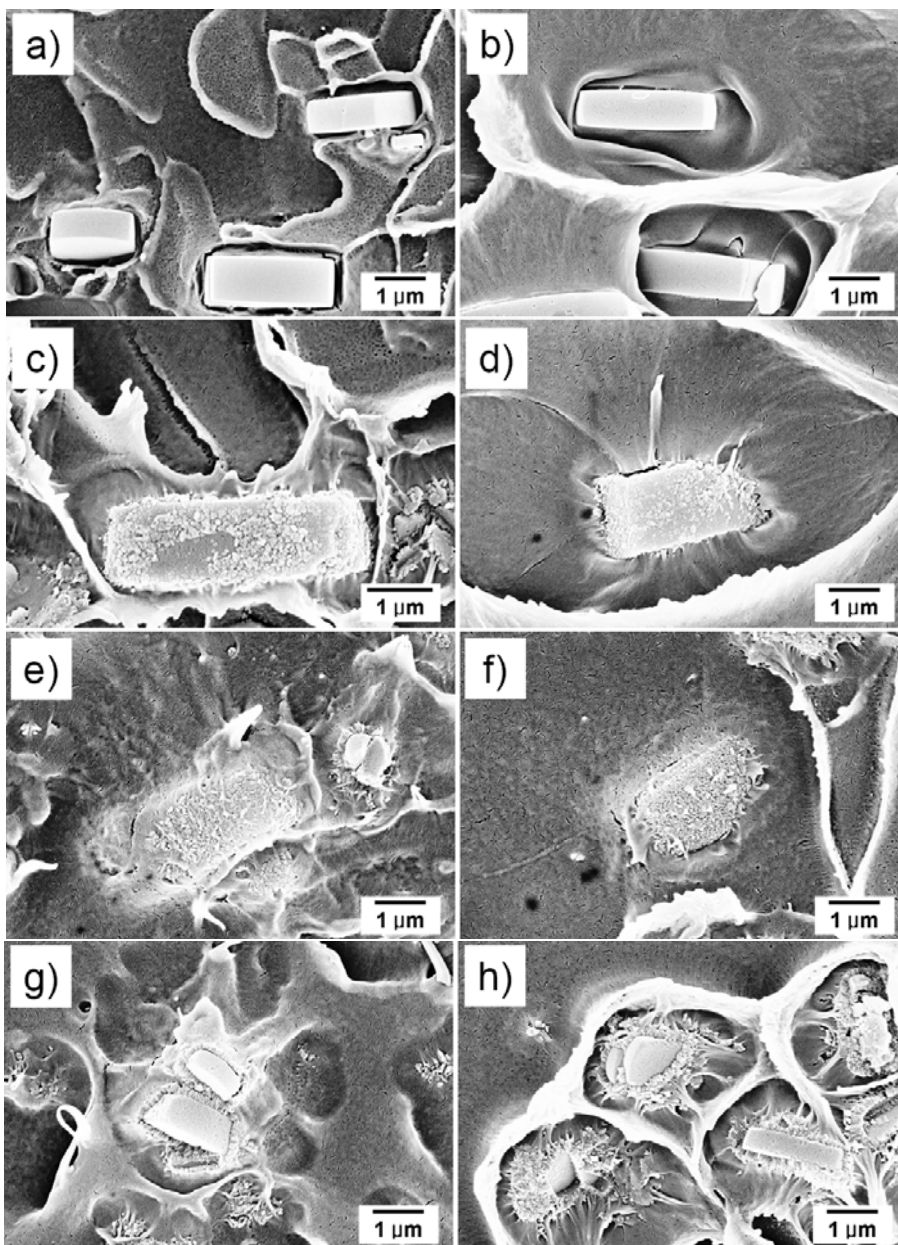


Figure 6.6: SEM images of PVAc composites containing 10 vol.% of untreated (UN) and surface-treated (GT and ST)  $\mu$ MFI, which are annealed at 20 and 100 °C for 24 h, respectively: UN (a) 20 °C and (b) 100 °C, GT (c) 20 °C and (d) 100 °C, ST (e) 20 °C and (f) 100 °C, and HST (g) 20 °C and (h) 100 °C.

The films composed of PVAc and unmodified MFI particles, regardless of particle size, showed a dewetted filler-polymer interface with interfacial voids around the particles (Figures 6.5a and 6.6a). The interfacial voids seem to be reduced after melt

annealing at 100 °C and subsequent slow cooling (Figures 6.5b and 6.6b). The interfacial voids at the MFI-PVAc interface are observed despite the fact that PVAc exhibited higher adhesion with MFI compared to polyimide and polyetherimide polymers in the Chapter 3 AFM studies [9]. This indicates that the interfacial attraction between MFI and PVAc is not sufficient to overcome other forces driving defect formation.

When the Grignard- or solvothermally-modified MFI particles are incorporated into PVAc, the resultant films exhibited wetted PVAc-MFI interfaces with significantly reduced or no detectable interfacial voids (Figures 6.5c, 6.5e, 6.6c and 6.6e). The interfacial morphology of the composites is determined by the balance achieved between the PVAc-MFI interaction energy, the cohesive energy of the polymer, and the entropy changes associated with the available configurations [10]. Entropy generally opposes polymer adsorption chains at a filler surface, while favorable interactions with the surface can potentially overcome these configurational limitations. Hence, the interplay of energetic and entropic factors determines the final structure of the composite. It has been proposed by others that nanoroughened structures may stabilize polymer chain adsorption at such interfaces, relative to flat surfaces, by minimizing entropic penalties for polymer adsorption [5, 10, 13]. In addition, nanoroughened structures can greatly enlarge the contact area, so that any attractive interaction energy might be enhanced. This was illustrated by the fact that the ST-nMFI, having a higher surface roughness, also showed reduced interfacial voids compared to GT-nMFI (Figures 6.5c and 6.5e). We propose that both increased surface area and reduced entropic penalty for adsorption lead to the elimination of dewetted void morphologies in the GT-MFI/PVAc and ST-MFI/PVAc composites [5, 10, 13].

Likewise, the increased roughness of ST-MFI microparticles ( $\mu$ MFI), induced by increasing the  $\text{Mg}(\text{OH})_2$  content from 5 to 20 wt%, may further enhance the compatibility of surface nanostructures with the PVAc matrix. However, composites with ST- $\mu$ MFI containing 20 wt% of  $\text{Mg}(\text{OH})_2$  showed “naked” MFI particles and evidence of free

whiskers in the film (Figures 6.6g and 6.6h). This apparent delamination between the ST-deposited  $\text{Mg}(\text{OH})_2$  layer and the MFI surface may indicate relatively weak adhesion between the solid layer of 20 wt% of  $\text{Mg}(\text{OH})_2$  on the MFI surfaces, compared to the 5 wt%  $\text{Mg}(\text{OH})_2$  sample. This result suggests that it is crucial to control the content of  $\text{Mg}(\text{OH})_2$  for achieving improved interfacial adhesion.

The interfacial morphology of composites depends on the annealing temperature as well as the surface roughness of the filler. Annealing at high temperature (100 °C), above the  $T_g$  of PVA, reduced the size of interfacial voids in the PVAc composites made with untreated MFI particles, regardless of the particle size (Figures 6.5b and 6.6b). Annealing provides additional mobility to PVAc chain segments, which likely enables access to otherwise inaccessible regions around the zeolites, resulting in relaxation of void defects near the MFI-matrix interface [14]. Another possible mechanism for the observed reduction in interface voids after annealing above  $T_g$  is that air bubbles existing in the void region might become mobile and could diffuse out through PVAc during the annealing process. However, high temperature annealing resulted in increased interfacial voids in PVAc composites embedded with GT- or ST-nMFI, as shown in Figures 6.5d and 6.5f. Because these voids are associated with the apparent stripping of whiskers from the nMFI surface, the increased voids are likely explained by a relatively weaker adhesion of inorganic surface nanostructures with the nMFI surface, compared to adhesion with the PVAc matrix. PVAc chain relaxation during melting and subsequent slow cooling produces stress at the polymer-particle interface, resulting in delamination between the whisker structures and the nMFI surface (Figures 6.5d and 6.5f).

Contrary to nMFI, nano-roughened structures on the  $\mu\text{MFI}$  surface still exhibited the wetted particle-PVAc interface even after melt annealing, shown in Figures 6.6d and 6.6f. This robust improvement in interfacial morphology after annealing is additional evidence of that  $\text{Mg}(\text{OH})_2$  nanostructures are more strongly adhered to  $\mu\text{MFI}$  surfaces than to nMFI. Considering that the nanostructure dimensions are near 40 to 100 nm, the

reduced curvature of the  $\mu$ MFI particle planar surfaces may result in more stable nucleation and growth of the nanostructures than nMFI with higher curvature [5]. Hence, the formation of stably-bound nanostructures and with significant strength to withstand residual stress during composite annealing can be achieved on the larger  $\mu$ MFI particles.

#### 6.3.2.2.2. Mechanical Properties

Representative tensile stress-strain curves for pure PVAc and PVAc composites containing 10 vol.% of unmodified  $\mu$ MFI at different annealing temperatures are presented in Figure 6.7.

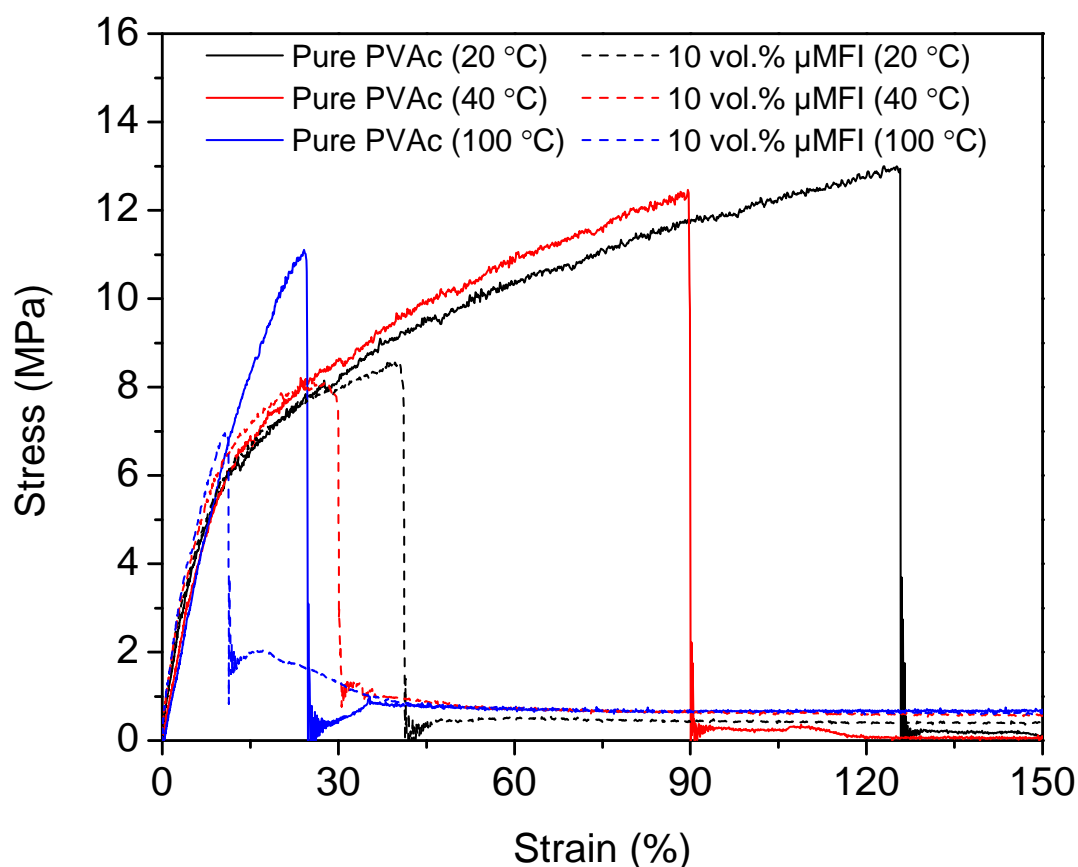


Figure 6.7: Stress-strain curves for pure PVAc and PVAc composites containing 10 vol.% of UN- $\mu$ MFI, annealed at 20, 40 and 100 °C for 24 h, respectively.

The addition of MFI particles led to a decrease in both the tensile strength and elongation at break. The modulus for PVAc composites is indistinguishable from that of pure PVAc up to strains of  $\sim 10\%$ . Even in the absence of filler, the mechanical properties of polymer may change during annealing [15]. In particular, the elongation at break significantly decreased with increasing annealing temperature for both pure PVAc and PVAc composites. This indicates that the PVAc matrix becomes more brittle as annealing temperature increases, in keeping with known densification behavior of amorphous glassy polymers annealed above  $T_g$ .

The tensile strength and elongation at break of PVAc composites containing bare and surface-treated nMFI or  $\mu$ MFI particles, as a function of filler loading (0 – 10 vol.%) and annealing temperatures (20 and 100 °C) are shown in Figures 6.8 and 6.9, respectively.

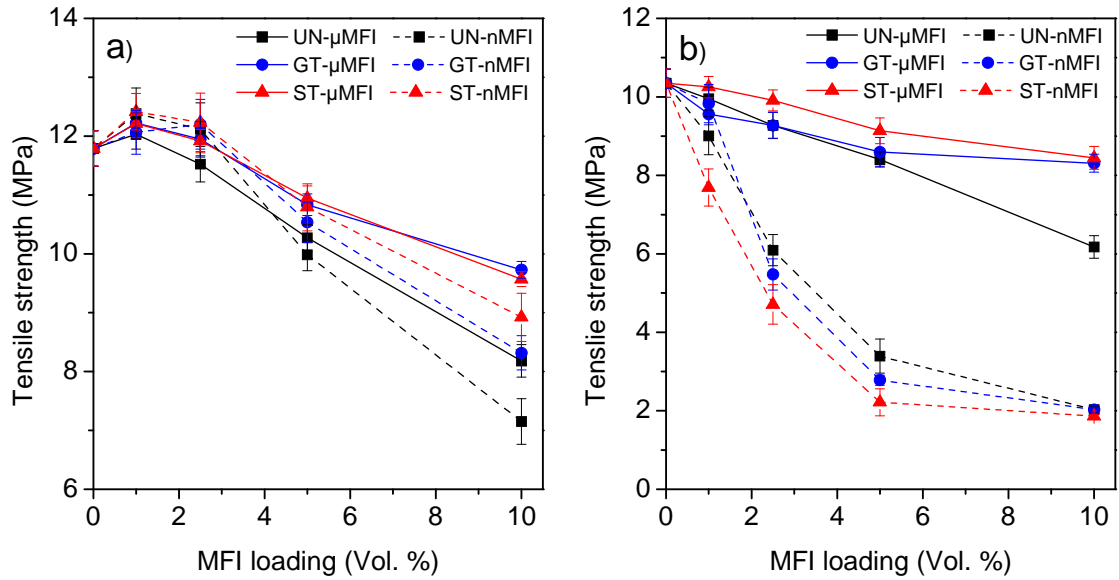


Figure 6.8: Tensile strength of PVAc composites containing UN-, GT- and ST-nMFIs or  $\mu$ MFIs as a function of MFI loading (1 – 10 vol.%) and annealing conditions ((a) 20 °C (solid line) and (b) 100 °C (dot line) for 24 h, respectively).

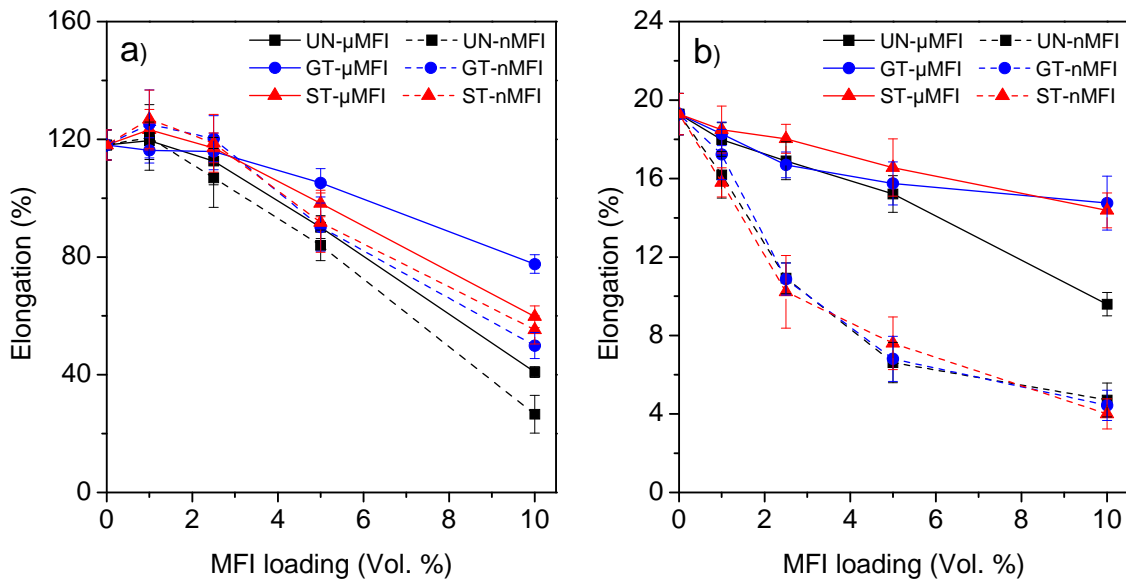


Figure 6.9: Elongation at break of PVAc composites containing UN-, GT- and ST-nMFIs or  $\mu$ MFIs as a function of MFI loading (1 – 10 vol.%) and annealing conditions ((a) 20 °C (solid line) and (b) 100 °C (dot line) for 24 h, respectively).

For the PVAc composites annealed at 20 °C, both the tensile strength and elongation slightly increased with MFI loading up to 1 vol.% MFI and decreased beyond that, regardless of the size and surface morphology of MFI particles. The tensile strength and elongation of the composites depends strongly on the effectiveness of stress transfer and the fracture behavior associated with stress concentration at the filler-matrix interfaces [1, 16, 17]. This decrease in mechanical properties with increasing MFI content can be explained by poor interfacial adhesion and hence inefficient stress transfer between the filler surface and the polymer matrix [1, 17], which was verified with void formation around the filler surface observed in SEM images (Figures 6.5a, 6.5b, 6.6a and 6.6b). For a given particle volume fraction, the mechanical properties of the composites further decreased for the smaller nMFIs. This is attributed to the increased polymer-MFI interfacial area which was proven to be inefficient at transferring stress.

Although both the tensile strength and elongation at break decrease with MFI loading, the reduction in the mechanical properties of PVAc composites was suppressed

via Grignard or solvothermal modification on the MFI particles (Figures 6.8a and 6.9a). At 10 vol.% of GT-MFI or ST-MFI, enhanced tensile strength and elongation at break were clearly observed relative to unmodified MFI-PVAc composites, suggesting improved interfacial adhesion due to surface modification of the particles with nanowhisker structures [17]. Improved adhesion and reduced defect formation at polymer-particle interfaces is known to enhance the effectiveness of load transfer and minimizes stress concentration at the interfaces, leading in an increase in strength and elongation [1]. Together with SEM evidence and previous AFM results (Chapter 3), the mechanical enhancement of composites made with surface-treated MFI, relative to bare MFI, results from improved interfacial adhesion with minimal interfacial voids associated with nano-roughened structures on the particle surfaces (Figures 6.5a-c and 6.6a-c). Thermodynamically-induced adsorption (smaller entropy loss upon adsorption) and increased attractive interaction by enlarged contact area are proposed to be possible reasons for enhancement in interfacial adhesion at the particle-polymer interface by creating nano-asperities on the particle surface [5, 10, 13].

The mechanical behavior of neat and composite films depends strongly on the annealing temperature. For the samples annealed at 100 °C, both the mechanical strength and elongation show a monotonic decrease as MFI loading increases (Figures 6.8b and 6.9b) for all cases. The reduction of mechanical properties by addition of MFI particles to the polymer matrix was most significant for the smaller nMFI particles having a higher total surface area [1]. This result implies that the interfacial stress transfer between the MFI surface and the polymer phase is still inefficient after melt annealing. Although interfacial voids were reduced after higher temperature annealing, voids still existed as shown Figures 6.5b and 6.6b. Thus, the particle cannot transfer any load and the mechanical properties of the composite decrease with increasing particle loading.

The effects of annealing temperature on the mechanical properties of the composites containing 10 vol.% of MFI particles are shown in Figure 6.10.



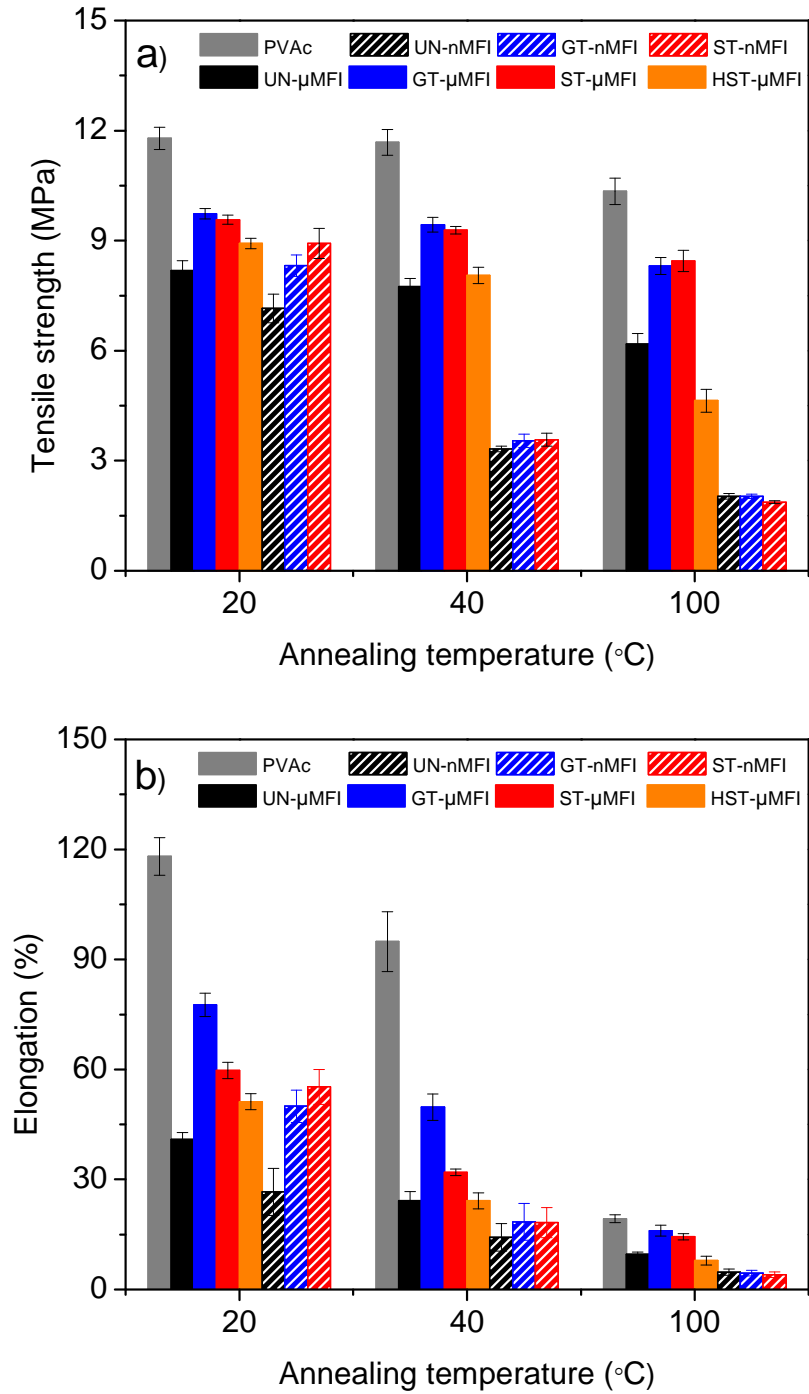


Figure 6.10: Mechanical properties (a) tensile strength and b) elongation at break) of pure PVAc and PVAc composites containing 10 vol.% of UN-, GT-, and ST-nMFIs or  $\mu$ MFIs as a function of the annealing temperature (20, 40, and 100 °C for 24 h, respectively). (HST denotes ST- $\mu$ MFIs with a higher content of  $\text{Mg}(\text{OH})_2$  (20 wt%)).

The elongation for both pure PVAc and PVAc composite films decreased significantly after higher temperature annealing, since the PVAc matrix becomes brittle with increased extent of chain relaxation. After annealing at lower temperature (20 °C), PVAc films filled with 10 vol.% of surface-modified MFI particles showed higher strength and elongation than composites with unmodified MFI, regardless of particle size. However, mechanical enhancement by nanostructured nMFI decreased with increasing annealing temperature, and finally, no improvement was observed for samples annealed at 100 °C.

On the contrary, the films containing nanostructured  $\mu$ MFIs exhibit mechanical enhancement relative to untreated MFI over the entire range of annealing temperature, indicating the formation of strongly-bound nanostructures on the larger  $\mu$ MFI surface (than compared to nMFI). This result correlates well with the interfacial morphology observed from SEM images, where interfacial voids and whisker delamination were observed with nMFI, while nanostructured  $\mu$ MFI surfaces showed no whisker delamination and fewer interfacial voids after annealing at high temperature (100 °C). Therefore, the creation of nanoscale morphology on the MFI surface, in particular on  $\mu$ MFIs, is correlated strongly with improved interfacial adhesion, minimal void formation, and improved mechanical properties compared to unmodified MFI. This is likely mediated by improved load transfer between the zeolite and the polymer matrix. The robust effect of nanostructured  $\mu$ MFIs, and the absence of these improvements with nanostructured nMFI, is probably attributed to relatively strongly-adhered nano-asperities on the larger particle, as discussed above.

Interestingly, the film containing ST- $\mu$ MFI with a higher content (20 wt%) of  $\text{Mg}(\text{OH})_2$  showed significantly reduced mechanical properties with increasing annealing temperature, with strength and elongation falling below even than those of bare MFI filled samples. The poor mechanical properties are correlated with observed delamination between the nanowhiskers and the zeolite surface (Figures 6.6g and 6.6h).

Relaxation of the polymer phase with increased annealing temperature is likely to further pull the nanostructures away from the particle surface, leading to a decrease in stress transfer efficiency. This result suggests there is an optimum amount of  $\text{Mg(OH)}_2$  for efficient stress transfer and interfacial improvement.

#### *6.3.2.2.3. Thermal Properties*

When an amorphous polymer is cooled from the rubbery to the glassy state through the glass transition region, the polymer below the  $T_g$  is in a non-equilibrium state characterized by excess volume, entropy, enthalpy and internal stress [15, 18-21]. The polymer slowly approaches the thermodynamic and structural equilibrium state through the conformational rearrangement of polymer segments under isothermal conditions. This process towards equilibrium is referred to as annealing, physical aging, or relaxation, and its rate depends on the physical environment (structural mobility) of the glass and the annealing temperature [18, 19, 21]. Increasing chain mobility or annealing temperature, close to but below the  $T_g$  of the polymer, accelerates the relaxation rate. The polymer structure is densified and becomes more uniform, as it moves to a more nearly equilibrium state upon annealing [20].

The thermal behavior of composite materials reflects the relaxation characteristics of polymer at the particle interface as well as that of the bulk polymer [3]. To better understand how the incorporation of nanostructured MFI affects the glass transition behavior associated with enthalpic relaxation, DSC measurements were performed on the composites with respect to the surface morphology of the fillers and annealing temperature.  $\Delta T$  and  $T_g$  values were listed in Table 6.1. Representative DSC spectra and  $\Delta T$  values for pure PVAc and PVAc composites containing 10 vol.% of nMFI with different surface treatments, as a function of annealing temperature, are presented in Figures 6.11a and 6.11b, respectively.

Table 6.1: Thermal properties (the width of the glass transition,  $\Delta T$ , and  $T_g$ ) of pure PVAc and PVAc composites containing 10 vol.% of UN-, GT- and ST-nMFIs or  $\mu$ MFIs as a function of the annealing temperature (20, 40, and 100 °C for 24 h, respectively).

Samples	$\Delta T$ (°C)			$T_g$ (°C)
	20 °C	40 °C	100 °C	
Pure PVAc	$23.6 \pm 0.9$	$15.5 \pm 0.7$	$5.1 \pm 0.6$	$44.9 \pm 2.2$
UN-nMFI	$15.4 \pm 1.3$	$10.5 \pm 0.5$	$4.3 \pm 0.5$	$44.7 \pm 1.9$
GT-nMFI	$20.0 \pm 1.2$	$12.7 \pm 0.6$	$4.4 \pm 0.2$	$45.5 \pm 2.2$
ST-nMFI	$22.4 \pm 1.7$	$14.8 \pm 1.1$	$4.0 \pm 0.4$	$45.7 \pm 1.1$
UN- $\mu$ MFIs	$14.7 \pm 1.9$	-	$4.1 \pm 0.3$	$44.6 \pm 0.5$
GT- $\mu$ MFIs	$20.6 \pm 1.2$	-	$4.3 \pm 0.2$	$45.9 \pm 1.3$
ST- $\mu$ MFIs	$22.9 \pm 1.1$	-	$4.3 \pm 0.6$	$43.9 \pm 0.9$

*Note.* Uncertainty is standard deviation.

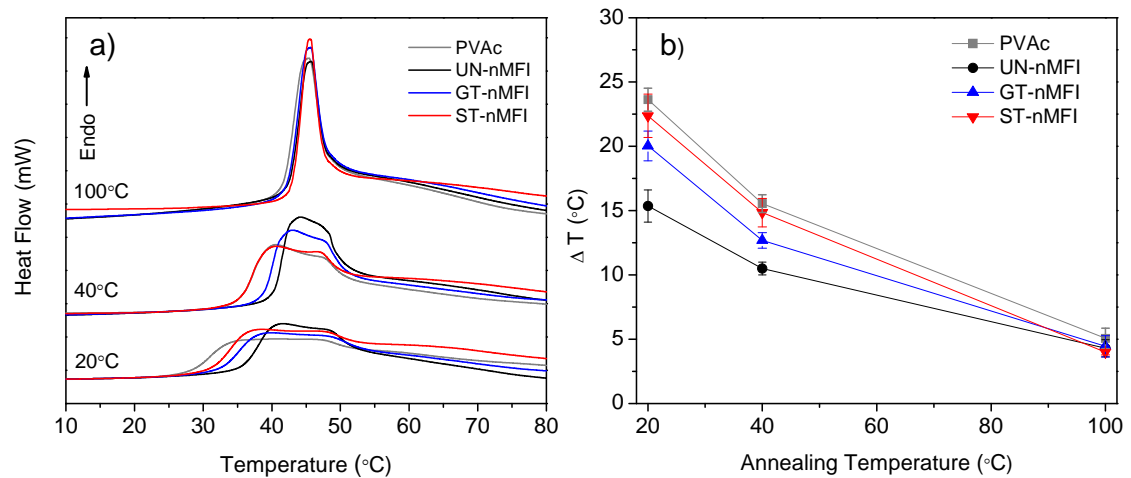


Figure 6.11: (a) DSC curves (b) width of the glass transition ( $\Delta T$ ) of pure PVAc and PVAc composites containing 10 vol% of UN-, GT and ST-nMFIs as a function of the annealing temperature (20, 40, and 100 °C for 24 h, respectively).

The neat PVAc is purely amorphous without any melting peak in the DSC curves. The changes in the glass transition with increased annealing temperature showed similar trends for both pure PVAc and PVAc composites: broad endothermic peaks appeared in the DSC heating curve of the samples annealed at 20 °C, attributed to a broad distribution of different relaxation times associated with a wide distribution of molecular environments having different conformational mobilities [4, 19, 22]. The position, magnitude and broadness of the peak is an indirect measure of the extent of enthalpic relaxation during annealing [19]. The endothermic peak shifts to higher temperature, increases in height, and narrows with increased annealing temperature. These changes in the glass transition peak are usually understood to be due to homogenization of chain segment local environments during the annealing process [19, 23].

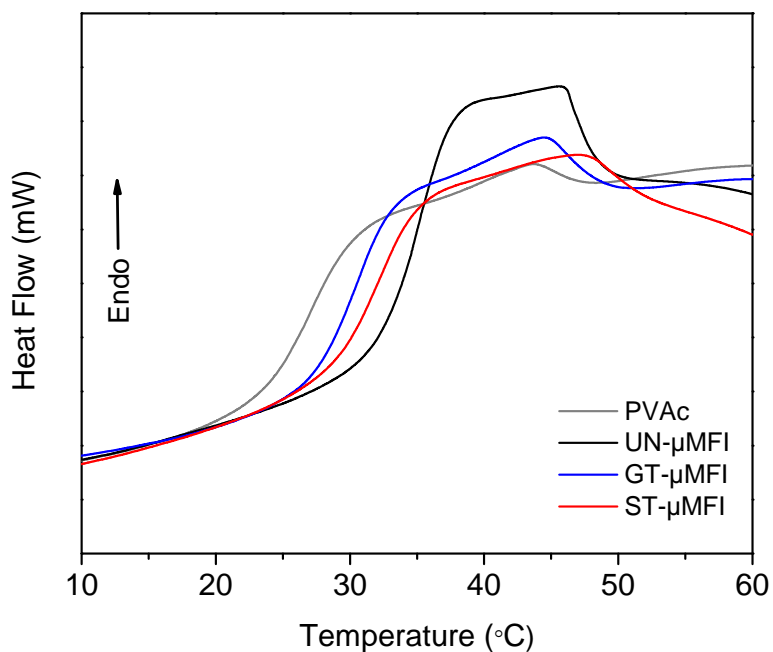


Figure 6.12: DSC curves of pure PVAc and PVAc composites containing 10 vol% of UN-, GT- and ST- $\mu$ MFIs, which are annealed at 20 °C for 24 h.

MFI/PVAc composites showed a narrower glass transition region than that of neat PVAc when the samples were annealed below  $T_g$  (20 and 40 °C), in particular for the

untreated nMFI-filled PVAc composites. This characteristic glass transition behavior of unmodified nMFI-filled PVAc was similar to the larger sized  $\mu$ MFI, where a narrow and intense glass transition was observed in the sub- $T_g$  annealed composites, as shown in Figure 6.12. On the other hand, no significant differences in the breadth or  $T_g$  value was observed between neat PVAc and PVAc composites after melt annealing at 100 °C for either nMFI or  $\mu$ MFI.

In polymer composites, the presence of fillers can significantly influence the relaxation dynamics and glass transition behavior of the polymer by altering the local structure near the filler interface [2, 3, 18]. The width of the thermal transition and  $T_g$  value in DSC curves were known to be altered with the addition of fillers, depending on the level of the polymer-filler interactions at interface [3, 18, 19, 24, 25]. The chain relaxation dynamics of the filled systems can be suppressed or accelerated in comparison with the neat polymer by changing the segmental mobility of polymer segments in the vicinity of the filler interface, depending on the strength of attractive interaction between the polymer and the filler [3, 18, 24]. If the polymer chains have a strong affinity for the particle surface, strongly-bound polymer chains near the filler surface experience a reduction in the chain mobility [2, 3, 18-21, 24, 26-28]. This restriction effect retards the rate of segmental relaxation relative to that of the neat polymer, and increases the  $T_g$  [2, 3, 18, 21, 24, 25]. In addition, the relaxation dynamics can determine the breadth of the relaxation time distribution [18]. In fact, a strong interaction between polymer and filler tends to broaden the glass transition of composites compared to that of bulk polymers [3, 18, 21, 24, 28].

Alternatively, if there are voids present around the filler particle, then the polymer exists in a state similar to a polymer-air interface. Although MFI exhibited higher adhesion with PVAc than with polyimide and polyetherimide, the MFI-PVAc interfacial adhesion is apparently not strong enough to prevent void formation. The weakness of the MFI-PVAc interactions is evident in SEMs of composite fracture surfaces where

dewetted interfaces were apparent between the untreated MFI surface and the PVAc (Figures 6.5a and 6.6b). Hence, in the MFI/PVAc composites, there is an effective air-polymer interface around each particle. The free surface is characterized as a highly mobile liquid-like interface having lower activation energy for conformational chain rearrangement and a narrower distribution of relaxation times than those of bulk polymer [27, 29]. This enhanced mobility is hypothesized to be due mainly to the segregation of chain ends to the free surface due to conformational entropy. The relaxation rate of chain segments in free surfaces is much faster than that of bulk polymer [27]. Hence, two relaxation domains with different relaxation rates can be proposed to exist in the MFI/PVAc composite system: the modes corresponding to the normal segmental motion of bulk polymer and faster relaxation dynamics corresponding to more mobile segments in the air/polymer interface in internal voids. Since the overall relaxation behavior of polymer composites depends on the relative contributions of the dynamics of each domain, the presence of a poorly-interacting filler increases the overall relaxation rate by creating highly mobile polymer regions around particles. Thus, under the same annealing condition the polymer matrix in the PVAc composite containing untreated MFI particles approaches the equilibrium glass state further, resulting in narrowing in width and increasing in the height of glass transition region, comparing to bulk PVAc. On the other hand, the PVAc composites prepared with surface modified (GT or ST) particles showed relatively broader glass transition peaks than composites with untreated particles. The broader glass transition in surface modified MFI composites is consistent with the wetted PVAc-filler interfaces observed in SEM images (Figures 6.5 and 6.6).

The observed difference in the width of the DSC endothermic peak of MFI/PVAc composites seems to depend on the degree (size and fraction) of interfacial voids surrounding the particles: the higher degree of interfacial voids (poorly wetted interface) for untreated MFI resulted in narrower and higher peaks due to the increased rate and extent of relaxation caused by enhancing overall chain mobility. On the other hand,

improved polymer-filler interaction, and hence suppressed formation of interfacial voids observed in surface-modified MFI fillers, is responsible for the relatively broader glass transition region. ST-nMFI, with a smaller degree of interfacial voids, showed broader and weaker glass transition peaks than GT-nMFI, as presented in Figure 6.11 and Table 6.1. This result supports the idea that the more roughened surface created by solvothermal treatment is more effective in enhancing interactions with PVAc, compared to the Grignard treatment. Surface treated samples, however, still showed narrower glass transitions than that of neat PVAc after sub- $T_g$  annealing. This implies that the interfacial voids might not be completely removed even though they are reduced significantly by surface modification.

In addition, the  $T_g$  of samples annealed at 100 °C were compared and there was no detectable difference in the value of  $T_g$  between PVAc and PVAc composites, within measurement error. These results suggest that the interaction between the highly relaxed PVAc matrix and either the bare or surface-modified particle is not strong enough to shift the overall  $T_g$  of the composite.

#### *6.3.2.2.4. XRD Characterization*

Pure PVAc and PVAc composite films composed of MFI particles with different surface morphologies were subjected to XRD to obtain further information regarding the interaction of zeolite particles with the polymer matrix. Figure 6.13a depicts the XRD patterns of pure PVAc and PVAc composites containing untreated  $\mu$ MFIs annealed at 20 °C and 100 °C. The XRD patterns of pure PVAc films annealed at 20 °C display two broad peaks at 13.1° and 22.1°, being consistent with those reported previously [30, 31]. These broad peaks result from the amorphous nature of PVAc and become more pronounced after annealing at 100 °C, implying that significant chain relaxation has occurred after melt annealing followed by slow cooling. For the MFI/PVAc composites, the presence of  $\mu$ MFIs within the PVAc matrix can be identified by a series of



characteristic peaks around  $8.2^\circ$ ,  $9.1^\circ$ , and  $23.5^\circ$ , which can be indexed as (101), (020) and (501) planes, respectively.

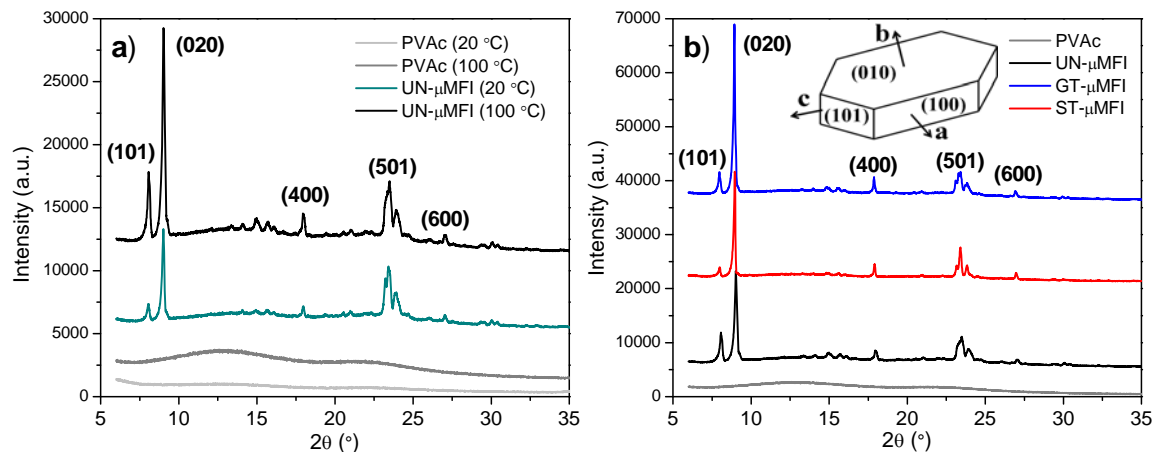


Figure 6.13: XRD patterns of (a) pure PVAc and PVAc composite films containing UN-μMFI, which are annealed at 20 and 100 °C for 24 h, respectively, (b) pure PVAc and PVAc composite films composed of UN-, GT- and ST-MFI μMFIs after annealing at 100 °C for 24 h, respectively.

For the unmodified μMFI, the relative intensities of these characteristic peaks remained essentially unchanged after annealing at 100 °C. On the other hand, interestingly, it was observed that intensity of the (020) MFI reflection was preferentially intensified after annealing at 100 °C for composites filled with surface-modified μMFI, as presented in Figure 6.13b. The relative (020) peak intensity is more pronounced, relative to the (010) peak, for the films made with GT- or ST-μMFI, compared to the (020) peak of untreated MFI composites. This result indicates that the surface-modified MFI particles are oriented preferentially with the b-out-of-plane direction within the PVAc matrix. This orientation preference may be attributed to the improvement in affinity of MFI filler with the PVAc phase associated with inorganic nanostructures on the filler surface, as illustrated in the morphological, mechanical and thermal characterization of the composites above. The rearrangement of polymer chain segments

during the annealing process may favor a specific orientation of the surface-treated MFI crystals that has more favorable interactions with the PVAc matrix. This result suggests that, by appropriate selection of the surface treatment method and the composite fabrication protocol, MFI particles with surface nanowhiskers may present a preferred orientation in the matrix, which often becomes critical to the film performance such as mechanical and membrane properties [32, 33].

#### **6.4. CONCLUSIONS**

This chapter investigated the effect of MFI zeolite loading, size, and surface treatment (Grignard or solvothermal method) with  $\text{Mg}(\text{OH})_2$  inorganic nanowhiskers on the structural, mechanical and thermal properties of MFI/Ultem and MFI/PVAc composites. It was found that the presence of nanostructures on the MFI surface improves compatibility and interfacial adhesion between the zeolite and the polymer matrix (both Ultem and PVAc), resulting in nearly defect-free interfaces. These results also indicated a strong correlation between interfacial morphology and adhesion forces determined previously by AFM. The enhancement is attributed to a surface roughening effect that facilitates adsorption (by lowering configurational entropy loss at the surface) and increases contact area.

For Ultem composites, there was no significant difference in mechanical properties with the different surface modifications. However, PVAc composites containing surface-modified particles had higher mechanical strength than those embedded with unmodified MFIs at the same loading. The annealing temperature of the composites had a strong influence on the morphological and mechanical properties of the films. The mechanical and morphological enhancement induced by surface modifications of the MFI nanoparticles decreased with increasing annealing temperature, while surface-modified MFI microparticles exhibited improvements relative to untreated samples over a wide range of annealing temperature. This robust effect of the

nanostructured microparticles indicates the formation of strongly-adhered nanostructures on the microparticle MFI surface (that was not apparent on the nanoparticle MFI). It was proposed that there is an optimum amount of  $\text{Mg}(\text{OH})_2$  for improving the mechanical properties and interfacial morphology of the composites, achieved by controlling the relative adhesion of nano-roughened structures with the polymer matrix versus the filler surface.

The dewetted (air/polymer) interfaces (interfacial voids) observed for untreated MFI/PVAc composites resulted in narrow glass transition regions due to the increased rate and extent of relaxation caused by high mobility of the polymer segments around the filler. On the contrary, the improved wetted interface (suppressed formation of interfacial voids) observed for surface-modified MFI fillers, led to slower relaxation and a broader glass transition region compared to that of unmodified particles. However, the extent of adhesion of nanostructures with the PVAc phase is apparently not strong enough to broaden the width and increase  $T_g$  value of PVAc by chain restriction effects. Improved interactions between the polymer and the surface-modified MFI induced a preferential orientation of the MFI particles within the PVAc matrix during the annealing process, confirmed by XRD analysis.

## 6.5. REFERENCES

1. Fu, S.Y., X.Q. Feng, B. Lauke, and Y.W. Mai, *Composites Part B*, 2008. **39**(6): p. 933-961.
2. Amanuel, S., A.N. Gaudette, and S.S. Sternstein, *J. Polym. Sci., Part B: Polym. Phys.*, 2008. **46**(24): p. 2733-2740.
3. Arrighi, V., I.J. McEwen, H. Qian, and M.B.S. Prieto, *Polymer*, 2003. **44**(20): p. 6259-6266.
4. Hutchinson, J.M., *Thermochim. Acta*, 1998. **324**(1-2): p. 165-174.

5. Bae, T.H., J.Q. Liu, J.S. Lee, W.J. Koros, C.W. Jones, and S. Nair, J. Am. Chem. Soc., 2009. **131**(41): p. 14662-14663.
6. Sormana, J.L. and J.C. Meredith, Macromolecules, 2004. **37**(6): p. 2186-2195.
7. Sormana, J.L. and J.C. Meredith, Mater. Res. Innov., 2003. **7**(5): p. 295-301.
8. Sormana, J.L. and J.C. Meredith, Macromol. Rapid Commun., 2003. **24**(1): p. 118-122.
9. Lee, J.H., B.J.R. Thio, T.H. Bae, and J.C. Meredith, Langmuir, 2009. **25**(16): p. 9101-9107.
10. Shu, S., S. Husain, and W.J. Koros, J. Phys. Chem. C, 2007. **111**(2): p. 652-657.
11. Baumgartner, A. and M. Muthukumar, Journal of Chemical Physics, 1991. **94**(5): p. 4062-4070.
12. Douglas, J.F., Macromolecules, 1989. **22**(9): p. 3707-3716.
13. Liu, J.Q., T.H. Bae, W.L. Qiu, S. Husain, S. Nair, C.W. Jones, R.R. Chance, and W.J. Koros, J. Membr. Sci., 2009. **343**(1-2): p. 157-163.
14. Mahajan, R. and W.J. Koros, Ind. Eng. Chem. Res., 2000. **39**(8): p. 2692-2696.
15. Sung, C.S.P., L. Lamarre, and K.H. Chung, Macromolecules, 1981. **14**(6): p. 1839-1841.
16. Ahmad, F.N., M. Jaafar, S. Palaniandy, and K.A.M. Azizli, Compos. Sci. Technol., 2008. **68**(2): p. 346-353.
17. Metin, D., F. Tihminhoglu, D. Balkose, and S. Ulku, Composites Part A, 2004. **35**(1): p. 23-32.
18. Lu, H.B. and S. Nutt, Macromolecules, 2003. **36**(11): p. 4010-4016.

19. Alves, N.M., J.F. Mano, E. Balaguer, J.M.M. Duenas, and J.L.G. Ribelles, *Polymer*, 2002. **43**(15): p. 4111-4122.
20. Yoshida, H., *Thermochim. Acta*, 1995. **266**: p. 119-127.
21. Salehi-Khojin, A., S. Jana, and W.H.K. Zhong, *J. Mater. Sci.*, 2007. **42**(15): p. 6093-6101.
22. Wu, W.B., W.Y. Chiu, and W.B. Liao, *J. Appl. Polym. Sci.*, 1997. **64**(3): p. 411-421.
23. Liao, K.R., D.P. Quan, and Z.J. Lu, *Eur. Polym. J.*, 2002. **38**(1): p. 157-162.
24. Rittigstein, P. and J.M. Torkelson, *J. Polym. Sci., Part B: Polym. Phys.*, 2006. **44**(20): p. 2935-2943.
25. Yim, A., R.S. Chahal, and L.E. Stpierre, *J. Colloid Interface Sci.*, 1973. **43**(3): p. 583-590.
26. Tsagaropoulos, G. and A. Eisenberg, *Macromolecules*, 1995. **28**(1): p. 396-398.
27. Ash, B.J., R.W. Siegel, and L.S. Schadler, *J. Polym. Sci., Part B: Polym. Phys.*, 2004. **42**(23): p. 4371-4383.
28. Verghese, K.N.E., R.E. Jensen, J.J. Lesko, and T.C. Ward, *Polymer*, 2001. **42**(4): p. 1633-1645.
29. Ash, B.J., D.F. Rogers, C.J. Wiegand, L.S. Schadler, R.W. Siegel, B.C. Benicewicz, and T. Apple, *Polym. Compos.*, 2002. **23**(6): p. 1014-1025.
30. Elashmawi, I.S., N.A. Hakeem, and E.M. Abdelrazek, *Physica B*, 2008. **403**(19-20): p. 3547-3552.
31. Zidan, H.M., *J. Polym. Sci., Part B: Polym. Phys.*, 2003. **41**(1): p. 112-119.
32. Bonilla, G., D.G. Vlachos, and M. Tsapatsis, *Microporous Mesoporous Mater.*, 2001. **42**(2-3): p. 191-203.

33. Chau, J.L.H., Y.S.S. Wan, A. Gavriilidis, and K.L. Yeung, Chem. Eng., 2002. **88**(1-3): p. 187-200.

## CHAPTER 7

### CONCLUSIONS AND RECOMMENDATIONS

#### 7.1. SUMMARY AND CONCLUSIONS

This work represents the successful culmination of the objectives outlined in Chapter 2. The research set out to accomplish the following objectives;

##### **1. Develop an AFM methodology for characterizing interfacial interactions**

The inorganic (zeolite and silica) colloidal probe AFM technique was successfully developed to measure inorganic-polymer adhesion and inorganic-inorganic interactions in various media. Together with surface tension analysis, AFM interfacial force measurements were used to discover the mechanisms governing adhesion and interactions between components in the dope solution used for mixed-matrix membrane spinning. The following conclusions can be made.

- a) Adhesion of bare MFI zeolite to imide-type polymer surfaces in air is determined by the Lewis basicity component of polymer surface energy, which is contributed primarily by carbonyl groups. Surface modification on the MFI zeolite by Grignard treatment enhanced zeolite-polymer interfacial adhesion significantly.
- b) Adhesion and interactions of silica materials depend strongly on the medium used in membrane spinning (air or NMP-water mixtures). Silica-silica adhesion is weaker in general than silica-polymer adhesion in solution, however, these relative magnitudes are the opposite in air. This suggests that a complex change in mechanisms driving adhesion between components occurs during the solvent-exchange and drying process that occurs during membrane spinning.

c) The role of non-DLVO forces in silica interactions in NMP-water mixtures was studied by using the AFM technique. The interactions between two hydrophilic silica surfaces in neat water or NMP were described qualitatively by the DLVO theory. However, the addition of NMP into water drastically altered the attractive and adhesive interactions. An unusually strong, long-range (60 – 80 nm), multi-stepped attraction appeared at 30 – 50 vol.% NMP, where the pull-off force was also maximized. The observed long-range force was hypothesized to rise from bridging of NMP macroclusters on the hydrophilic silica surfaces.

## **2. Characterize and correlate polymer composite properties**

We successfully determined the mechanical, structural and thermal properties of MFI/polymer dense films, and correlated them to AFM adhesion force data. The effect of MFI zeolite loading, size and surface treatment (Grignard or solvothermal method) on the composite properties was examined.

a) The creation of nanowhisker structures on MFI zeolite surface promoted compatibility between the zeolite and the polymer matrix (both Ultem and PVAc), resulting in nearly defect-free interfaces. The improved interfacial morphology imparted by surface roughening correlates well with adhesion forces determined by AFM. Thermodynamically-induced adsorption (reduced entropy loss) and increased contact area are suggested to be responsible for enhancement in polymer adhesion at the nanowhisker-covered zeolite interfaces.

b) Polymer characteristics affect on the mechanical enhancement of polymer-zeolite composites by zeolite surface modification. For glassy and strong Ultem composites, there was no significant improvement in mechanical properties imparted by the roughened zeolite. However, rubbery and flexible PVAc composites containing surface-modified zeolite particles exhibited increased



tensile strength and elongation at break relative to those containing unmodified zeolite.

c) The film annealing temperature had a strong influence on the morphological and mechanical properties of the MFI/PVAc composites. Surface modification of zeolite microparticles exhibited interfacial and mechanical enhancement over a wider range of annealing temperatures than zeolite nanoparticles. This robust effect of the nanostructured microparticles indicates the formation of strongly-adhered nanostructures on the larger microparticle surface. An optimal surface morphology and zeolite modification protocol (solvothral method with proper amount of  $\text{Mg}(\text{OH})_2$ ) was proposed for achieving the most enhanced mechanical and interfacial properties in composites

d) DSC revealed that surface-modified MFI resulted in broader glass transitions compared to PVAc composites containing unmodified MFI. This thermal characteristic is explained by enhanced interfacial adhesion and associated slower chain relaxation dynamics. Improved zeolite-polymer interfacial adhesion, due to surface modification, also induced a preferential orientation of the MFI particles within the PVAc matrix during the annealing process, confirmed by XRD analysis.

## **7.2. RECOMMENDATIONS FOR FUTURE WORK**

In light of the conclusions of this work, several key questions have been raised that remain unanswered. This section will seek to provide some of these questions, as well as possible strategies to answer these issues in a scientific manner.

### **7.2.1. Correlate AFM Interaction Results to the Final Membrane Morphology**

The colloidal probe AFM technique developed in this study is an excellent tool to probe the equilibrium interactions between dope components during membrane spinning.

However, the correlation of interfacial forces to phase separation kinetics, and hence membrane morphology, remains challenging. The main difficulty results from the fact that the final membrane morphology is determined by a complex and dynamic change in interactions between components during the membrane spinning process, where the medium is changing by solvent exchange, polymer phase separation, and evaporation, simultaneously. In addition, there is the potential influence of shear force. Nevertheless, it would be worthwhile to correlate interaction energies between components (zeolite-zeolite, zeolite-polymer and polymer-polymer) in various media (NMP-water mixtures) to the phase diagram. By comparison to a neat polymer system, the influence of zeolites on phase separation kinetics, and subsequently on the final membrane morphology, can be determined.

#### **7.2.2. Define Adhesion of Zeolite to Polymers**

The adhesion mechanism at MFI zeolite-imide type polymer interfaces in air was successfully determined by the zeolite colloidal probe technique. The acid-base interaction between the basicity of polymer and acidity of MFI was found to play a key role in the interfacial adhesion between zeolite and polymer phase. Zeolites are aluminosilicate materials whose solid acidity can be controlled by the Si/Al ratio, with higher ratios leading to decreased acidity [1]. For example, LTA zeolite with its Si/Al ratio of about 1.0 has higher acidity than pure-silica MFI zeolite with its Si/Al ratio of  $\infty$  [2-4]. Hence, it would be interesting to determine zeolite-polymer (imide-type) interfacial adhesion force as a function of the Si/Al ratio. In addition, adhesion forces between the zeolite and a series of acidic polymers (e.g. polysulfone-type) can be measured. These results might enable one to quantify a dominant factor affecting zeolite-polymer adhesive forces, and predict the adhesion based on the chemistry of zeolite and polymer.

### **7.2.3. Relate Composite Properties to Membrane Permselectivity and Evaluate Usefulness in Predicting Membrane Performance.**

Composite properties (mechanical, morphological and thermal) were correlated successfully with zeolite-polymer interfacial characteristics. However, an ultimate goal is to predict membrane separation performance based on knowledge of the particle, surface modification, polymer, and annealing. One might quantify the degree of defects by measuring deviation from permselectivity of mixed-matrix membranes predicted by the Maxwell model [5, 6]. In addition, one can determine the effect of film annealing conditions on membrane transport properties and correlate known mechanical and structural properties to membrane performance.

### **7.3. REFERENCES**

1. Sato, H., Catal. Rev.-Sci. Eng., 1997. **39**(4): p. 395-424.
2. Desbiens, N., I. Demachy, A.H. Fuchs, H. Kirsch-Rodeschini, M. Soulard, and J. Patarin, Angew. Chem. Int. Ed., 2005. **44**(33): p. 5310-5313.
3. Diaz, I., E. Kokkoli, O. Terasaki, and M. Tsapatsis, Chem. Mater., 2004. **16**(25): p. 5226-5232.
4. Sugiyama, S., S. Yamamoto, O. Matsuoka, H. Nozoye, J. Yu, G. Zhu, S. Qiu, and I. Terasaki, Microporous Mesoporous Mater., 1999. **28**(1): p. 1-7.
5. Mahajan, R. and W.J. Koros, Polym. Eng. Sci., 2002. **42**(7): p. 1420-1431.
6. Moore, T.T., R. Mahajan, D.Q. Vu, and W.J. Koros, AIChE J., 2004. **50**(2): p. 311-321.

# APPENDIX A

## METAL-POLYMER INTERFACES IN METAL-COATED POLYMER COMPOSITE MICROSPHERES

### A.1. INTRODUCTION

Many applications involving metal nanoparticles (NPs) require their impregnation into a carrier particle (CP), often a submicron to micrometer sized polymer bead. Polymer CPs serve as supports, to passivate or protect the particles from the environment, to prevent leaching of NPs, and to facilitate transport of heat and mass. The assembly of such NP-CP constructs requires control over NP loading and distribution within the CP.

These metal NP-CP composite materials have attracted intense interest in recent years due to applications in electronics [1, 2], photonics [3-6], medical imaging [7, 8], drug delivery [9, 10], immunoassays [9, 11-13], catalysis [14], and surface-enhanced Raman scattering (SERS) [15, 16]. Gold (Au) and silver (Ag) NPs have been used widely due to their desirable optical, electronic and biocompatibility properties. In particular, Au and Ag NPs are attractive for imaging applications because their resonance wavelengths can be tuned precisely over a broad range by controlling particle size and shape [17]. Metallic nanoshells, consisting of a dielectric core covered with a thin ( $< 20$  nm) shell of metal, exhibit a plasmon resonance that is a function of the core radius-to-shell thickness ratio [18-20]. Highly efficient and intense light scattering characteristics of noble metal particles of size  $\sim 140$  nm or less have enabled their use as fluorescent analogues [21]. By incorporating metal NPs exhibiting preferential scattering characteristics on a polymeric bead surface, the resulting composite microsphere can be

used as a scattering contrast agent for biomedical imaging and for labeling cells in flow cytometry [7, 13, 20, 22-27].

In addition, metal NP-coated polymer beads have been exploited as substrates for SERS [15, 16, 28, 29]. Raman spectroscopy yields an excellent fingerprint of molecules and biological materials, but it suffers from low signal response at concentrations typical of biological systems. The assembly of plasmonic metal (Au and Ag) NPs leads to enhancement of the plasmonic field between the NPs, which in turn leads to shifts in the wavelength and intensity of surface enhanced plasmon resonance as well as enhancement of the scattered light cross section [30]. Even though different chemistries and shapes of metal NPs, Au spheres [31] and rods [32], have been used to enhance the SERS, Ag NPs and aggregates have been regarded as the most suitable materials for SERS substrates. This is because Ag gives better enhancement as a result of intense surface plasmon resonance in the visible wavelength, compared with Au [15, 33, 34]. The SERS effect has broadened the spectrum of possible uses of metal-coated polymer beads for trace chemical analysis and biomedical labeling applications [35].

A number of recent efforts have focused on fabricating such metal-coated polymer composite beads with tailored structural, optical, and surface properties. Several interfaces, including metal nanoparticle-polymer, polymer-polymer and metal nanoparticle-metal nanoparticle, play key roles in the fabrication of composite microbeads. These lab-scale processes can be divided roughly into two classes: *in-situ* (NP grown within polymer) and *ex-situ* (NP added after formation to polymer) methods. *In-situ* metal reduction techniques on unmodified Polystyrene (PS) [1, 14, 28, 29, 36-38] or functionalized polymer beads [13, 20, 29, 39-45] have been reported. Unfortunately, irregular and low metal coverage on the beads was typically observed. Additional procedures such as metal ion presoaking [37], metal seeding [38] or surface modification [13, 20, 40, 42] are required for higher metal coverage. Nevertheless, it is hard to control

the size distribution and aggregation of the metal NPs in the coatings [1, 14, 26, 36, 44-46].

Alternatively, *ex-situ* techniques for attaching preformed metal NPs with well-defined shape and narrow size distribution to functionalized polymer microspheres have been proposed [11, 47-50]. Metal surface coverage less than 30 % is usually reported. Electroless plating has been combined with these seeding processes, which led to uniform and dense metallic shells on dielectric core materials [2, 19, 51-53]. Electrostatic interactions have been utilized in two additional methods: metal NP infiltration into polyelectrolyte-coated beads [18, 47, 54] and layer-by-layer (LbL) self-assembly [55-58]. In particular, the LbL technique allowed the preparation of a metal layer with uniform and controlled thickness on the polymer beads. However, time-consuming sequential polyelectrolyte deposition cycles and purification steps are required. The assembly may also become unstable in solutions with different pH or ionic-strength [59, 60]. These considerations fuel the demand for alternative methods for the robust incorporation of metal NPs onto polymeric substrates.

## **A.2. OVERVIEW**

In this chapter, we present a new method for the preparation of metal NP-coated polystyrene (PS) latex beads: combined swelling-heteroaggregation [61, 62]. CSH is a facile and relatively benign process that overcomes limitations in surface coverage, multistep processing, harsh treatments, and long-term stability concerns of alternative strategies. A range of NPs with different sizes (30, 60 and 80 nm), chemistries (gold and silver), and shapes (sphere and cube) were successfully coated on the PS beads by using a CSH procedure.

Homogenous and dense metal coatings on the PS beads were obtained by the addition of tetrahydrofuran (THF) to an aqueous cosuspension of polyvinyl pyrrolidone (PVP) capped-metal NPs and 10  $\mu\text{m}$  PS beads. Composite beads were stable with no loss

of the NP coating during long-term (15 months) DI water storage. The kinetics of homo- and heteroaggregation occurring during the CSH process was studied. The coating morphology, metal coverage, and optical properties of the composite beads were tunable by simple adjustments in THF and NP compositions as well as the NP chemistry, shape and size.

The optical properties of the resulting metal-coated microspheres were characterized by using dark field microscopy and UV-vis microabsorption spectrometry, and SERS characteristics were studied with Raman spectroscopy.

### **A.3. EXPERIMENTAL**

#### **A.3.1. Materials and Synthesis**

##### ***A.3.1.1. Materials***

Reagent-grade silver nitrate, hydrogen tetrachloroaurate, sodium citrate, sodium sulfide, poly(vinyl) pyrrolidone (PVP,  $M_n = 55,000$  g) and ethylene glycol (EG) were purchased from Aldrich and used as received. Tetrahydrofuran (THF,  $\geq 99.9\%$ ) was used as purchased from EMD Chemical Inc. Monodisperse PS microspheres ( $9.7\ \mu\text{m} \pm 0.3\ \mu\text{m}$ , 1.0 wt%) in water, cross-linked with 4-8 wt. % of divinylbenzene, were obtained from Duke Scientific Corp. Deionized (DI) water ( $18.2\ \text{M}\Omega\ \text{cm}$ ) was prepared in a Millipore Milli-Q Plus 185 purification system.

##### ***A.3.1.2. Nanoparticle Synthesis***

Spherical gold nanoparticles (AuNPs,  $32 \pm 3\ \text{nm}$  and  $79 \pm 5\ \text{nm}$ , by transmission electron microscopy (TEM)) were prepared by the method of Freund and Spiro [63] with some modification. First, 1 mL hydrogen tetrachloroaurate aqueous solution (0.1g/10 mL) was added to 100 mL of DI water. Then the solution was brought to  $100\ ^\circ\text{C}$ . To prepare 30 and 80 nm AuNPs 2 mL of sodium citrate aqueous solution with concentration of 0.35 and 0.2 g/100 mL were added, respectively, followed by the addition of 0.005 and

0.002 g of PVP, respectively. The resulting solution was stirred at 100 °C for 4 min. The concentrations of the resulting AuNP aqueous solutions were  $6.9 \times 10^{11}$  (30 nm) and  $2.9 \times 10^{10}$  (80 nm) particles  $\text{mL}^{-1}$ . Silver nanocubes (AgNCs,  $62 \text{ nm} \pm 3 \text{ nm}$ , by SEM) were prepared by heating 30 mL of EG at 150 °C for 1 h, followed by the addition of a solution of 0.25 g PVP dissolved in 10 mL EG. [64]. The resulting solution was heated to return the temperature to 150 °C. Then 0.4 mL sodium sulfide (3 mM) dissolved in EG was added followed by slow injection of 2.5 mL of 282 mM silver nitrate dissolved in EG. The silver ions were reduced completely after 15 min, producing AgNCs. For purification the solution was diluted with acetone and DI water, and then centrifuged at least four times. The particles were then re-dispersed in DI water at a concentration of  $9.7 \times 10^{15}$  particles  $\text{mL}^{-1}$ . TEM and SEM images of metal NPs used in this study are shown in Figure A.1.

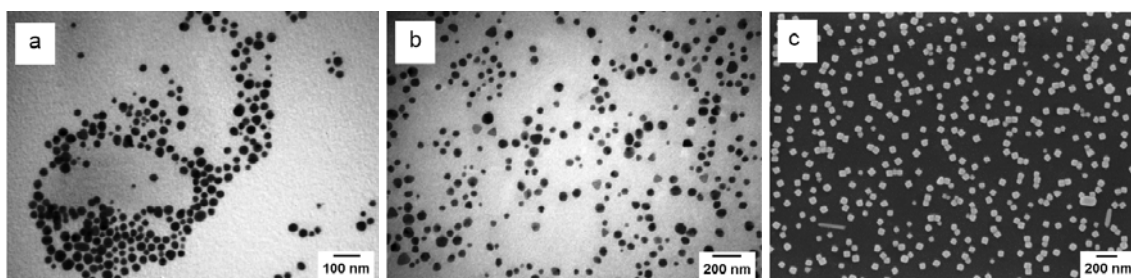


Figure A.1: (a and b) TEM images of AuNPs: a) 30 nm and b) 80 nm, and (c) SEM image of 60 nm AgNCs.

#### ***A.3.1.3. Metal NP Incorporation via CSH***

100  $\mu\text{L}$  of PS beads aqueous suspension, as-received, was put into a 1.7 mL tube and 650  $\mu\text{L}$  of the desired metal colloidal dispersion was added and stirred for 30 sec. THF was added dropwise to the suspension until the vol % of THF in water reached 50 vol %, and the mixture was agitated using a rotational shaker for 6 h. The mixture was then washed with DI water via at least four centrifugation cycles. The total mixture volume and amounts of PS and THF were kept constant for all samples. Metal surface



coverage was controlled by the ratio of the number of metal NPs to PS particles used in incorporation.

### **A.3.2. Experimental Methods**

UV-vis spectra of metal NPs and composite microbeads in solution were measured with an Ocean optics HR4000Cg-UV-NIR. UV-vis microabsorbance spectra of single metal-coated PS beads were measured using an SEE1100 micro-spectrometer under 50 X magnification. The spot size (3  $\mu\text{m}$  in diameter) was focused onto a single bead. The spectra measured from metal-coated PS beads were referenced to that of a bare PS bead. A Holoprobe Raman microscope (Kaiser Optical Systems) with 785 nm laser excitation was used for surface Raman measurement under 50 X magnification. Measurements were done from the 4 x 4  $\mu\text{m}^2$  spot area within a single bead at an accumulation time of 3 second with 15 scans. Dark field optical images were recorded using an inverted Olympus IX70 microscope with a high numerical aperture dark field condenser (U-DCW). SEM was performed with a LEO 1530 instrument for characterizing metal coated PS beads, and a Zeiss Ultra 60 was used for the AgNCs, respectively. Metal surface coverage on the PS beads was estimated from SEM images using ImageJ software. To measure AuNP size, TEM was performed with a JEOL 100C. AFM images of 30 nm AuNP-coated microbeads was obtained using a scanning probe microscope (PicoScan 5, Molecular Imaging) operated in tapping mode with a sharp tip (ACTA, Applied NanoStructures, Inc.).

## **A.4. RESULTS AND DISCUSSION**

### **A.4.1. CSH Mechanism**

Using the CSH process depicted in Figure A.2, NPs of different sizes (30, 60 and 80 nm), chemistries (Au and Ag), and shapes (sphere and cube) were successfully coated on unfunctionalized PS beads (10  $\mu\text{m}$  in diameter) [61, 62].

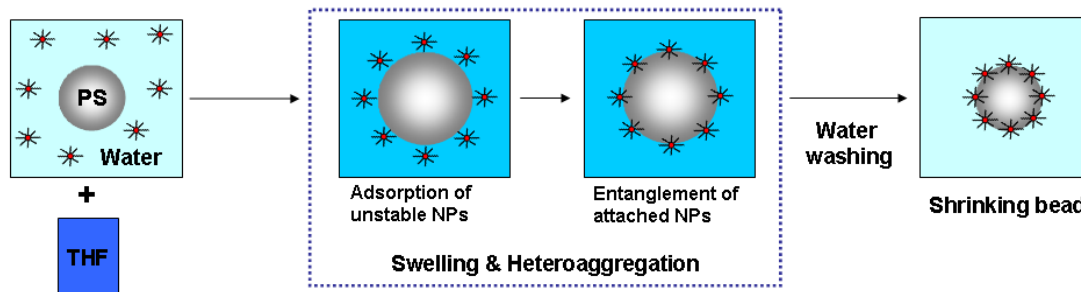


Figure A.2: Proposed combined swelling-heteroaggregation (CSH) process.

Starting with PVP-capped metal NPs and PS beads dispersed in water, homogenous and dense metal coatings were obtained by the addition and removal of 50 vol.% THF. The process is believed to occur in three steps; 1) THF induced swelling of the PS beads, 2) heteroaggregation of NPs and PS beads, and 3) deswelling of the beads by removal of THF. Based on detailed results below, THF appears to drive the swelling of PS beads and simultaneously induces heteroaggregation of the PVP-capped NPs and PS particles. The resulting composite consists of PS beads covered with metal NPs. The water-dispersed PS beads swell up to 1.5 times their original size, and deswell reversibly following the addition and removal, respectively, of 50 vol % THF, as shown in Figure A.3 [61]. Subsequent solvent deswelling likely densifies polymer chains to trap NPs in the polymer outer surface, resulting in dense metal coverage [61, 62].

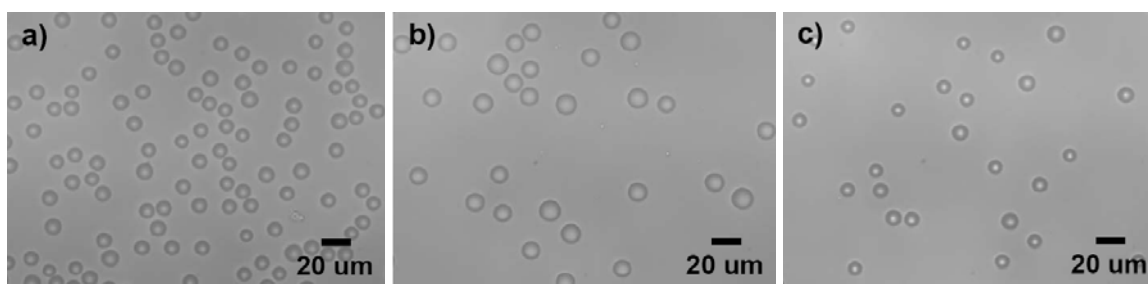


Figure A.3: Optical microscopy images of PS beads in a) DI water, b) 50 vol.% THF-water solution, and c) DI water after washing THF.

The integrity of the coatings was verified by UV-Vis measurements that showed no observable plasmon peak in supernatant solutions after at least 15 months in water, indicating excellent stability and resistance to metal loss. In addition no evidence of metal loss was observed after 10 min sonication at 50 kHz. These results suggest a strong anchoring of metal NPs on the bead surface that is probably mediated by entanglement of the PVP (from the AuNP surface treatment) with PS. This entanglement likely occurs while the bead is swollen with THF. As the bead is swollen by THF solvent, polymer matrix becomes liquefied and flexible, facilitating entanglement of the PVP with PS chains [62, 65, 66]. Once the THF is removed, the AuNPs are apparently trapped within the glassy PS. Kim *et al.* proposed a similar mechanism for ‘grafting’ functionalized polymers on PS beads via swelling with an organic solvent followed by shrinking during solvent removal [66].

Low metal surface coverage ( $< 30\%$ ) is a common finding for direct adsorption of metal NPs from aqueous media onto large polymer particles [47, 67]. Electrostatic repulsion of capped and charged metallic NPs has proven to be the major difficulty in producing dense coatings [54]. One possible explanation for the dense coating obtained by the CSH technique is an appropriate balance between heteroaggregation and homoaggregation of the PVP-AuNPs and PS particles induced by the addition of a non-solvent of PVP, THF.

In order to examine the role of THF in the heteroaggregation, UV-vis spectra of 30 nm AuNPs in 50 vol.% THF-water solution were measured at various times, shown in Figure A.4. The plasmon resonance of AuNPs in pure water was indicated by a sharp peak around 526 nm, nearly identical to the ‘0 min’ spectra in Figure A.4. After 50 vol.% THF was added, the plasmon peak became increasingly red-shifted, broadened,

and decreased in intensity with time after 1 h. These optical phenomena result from the plasmon resonance coupling effect caused by the formation of AuNP aggregates [68, 69], which indicated that the AuNPs were unstable in the 50 vol.% THF-water mixture. Significant AuNP aggregation was not observable until after 1 h in the 50 vol.% THF-water mixture. The capping polymer, PVP, is readily soluble in water, while it is nearly insoluble in THF [70-72]. Therefore, the effectiveness of PVP as a polymeric stabilizer was diminished and PVP-capped NPs became unstable and aggregated as the composition of THF increased.

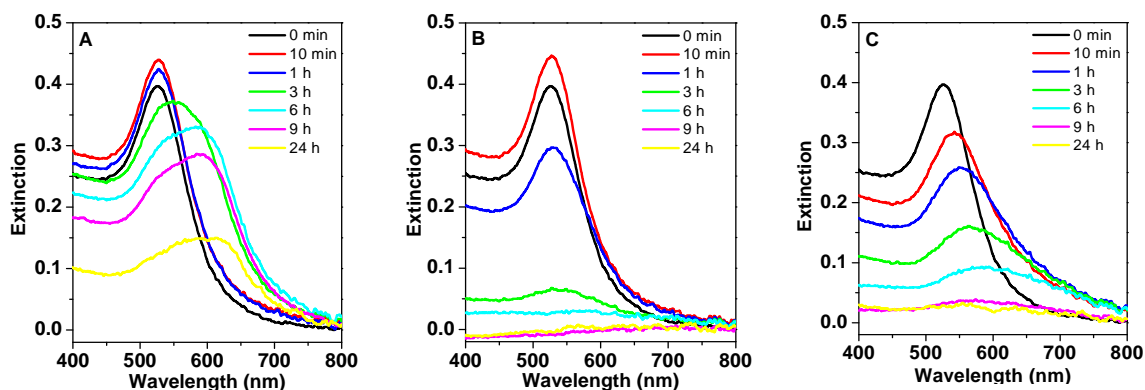


Figure A.4: UV-Vis spectra of 30 nm AuNPs in THF-water solutions at various times: (A) 50 vol.% THF-water solution in the absence of PS beads, (B) 50 vol.% THF-water solution in the presence of PS beads, (C) 70 vol.% THF-water solution in the absence of PS beads.

Figure A.4b shows UV-Vis spectra of supernatant solutions that were separated by centrifugation from AuNP-PS cosuspensions in a 50 vol.% THF-water mixture at various times. In contrast to Figure A.4a, in the presence of PS beads the AuNP plasmon peak showed no red-shifting and minimal broadening over the same time intervals. This result indicated that the homoaggregation of AuNPs in solution was inhibited when PS beads were present. Figure A.4b also shows a successive decrease in plasmon peak intensity after 1 and 3 h, indicating disappearance of suspended AuNPs. Together with

the SEM evidence (Figure A.5a), these results show that the AuNPs heteroaggregate with the swollen PS beads following addition of THF. A clear supernatant solution with no detectable plasmon peak was obtained after 6 h, indicating complete incorporation of AuNPs onto the PS beads.

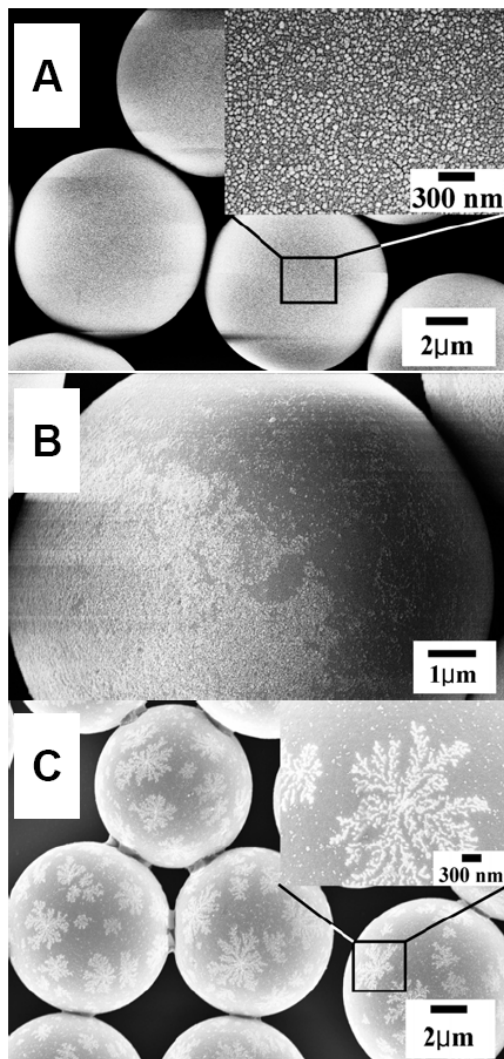


Figure A.5: SEM images of 30 nm AuNP-coated PS beads obtained from (A) 50 vol.% THF-water solution ( $n$  = the ratio of the number of metal NPs to PS particles =  $1.3 \times 10^5$ ), (B) 70 vol.% THF-water solution ( $n = 1.3 \times 10^5$ ), (C) 50 vol.% THF-water solution ( $n = 1.0 \times 10^5$ ).

AuNP homo- and heteroaggregation proceed simultaneously and heteroaggregate morphology can be controlled by the colloidal stability of the components [73]. We expect that THF concentration can be used to control the relative stability of the AuNPs, and hence influence the morphology and deposition speed of the metal coating. THF compositions above 50 vol.% led to highly irregular metal coatings, shown in Figure A.5b for 70 vol.% THF solution. This is thought to be due to homoaggregation of AuNPs occurring prior to heteroaggregation with the PS beads. This was confirmed in Figure A.4c, which shows UV-vis spectra of 30 nm AuNPs in 70 vol.% THF-water solution at various times. Comparing to the 50 vol.% THF solution (Figure A.4a), the rate of change (red-shifting, broadening and decreasing in intensity) of the plasmon peak became faster, and plasmon resonance peak disappeared entirely after 9 h. This result indicates that at 70 vol.% THF the rate of AuNP homoaggregation was apparently much faster than the heteroaggregation of AuNPs and PS beads, compared to 50 vol.% THF. Significant homoaggregation interferes with the formation of a continuous metal particle coating (Figure A.5b). In contrast, at THF compositions lower than 50 vol.%, AuNPs became stable, leading to PS beads with less metal coating. In fact, no deposition of AuNPs was observed for THF concentrations less than 25 vol.% even after 24 h, which was verified by the white color of the resulting beads.

UV-vis spectra of 80 nm AuNPs in THF-water solution showed results similar to those of 30 nm AuNPs, shown in Figures A.6a and 6b. In the absence of PS, the AuNPs homoaggregated upon addition of 50 vol.% THF with a broad plasmon resonance peak at long wavelength developing (Figure A.6a). A broad plasmon band at long wavelength originates from intensified interparticle plasmon field coupling due to the formation of AuNP homoaggregates. However, in the presence of PS beads the AuNPs heteroaggregated with the PS particles, resulting in no detectable broad peak at long wavelength in the supernatant solution over the same time intervals (Figure A.6b).

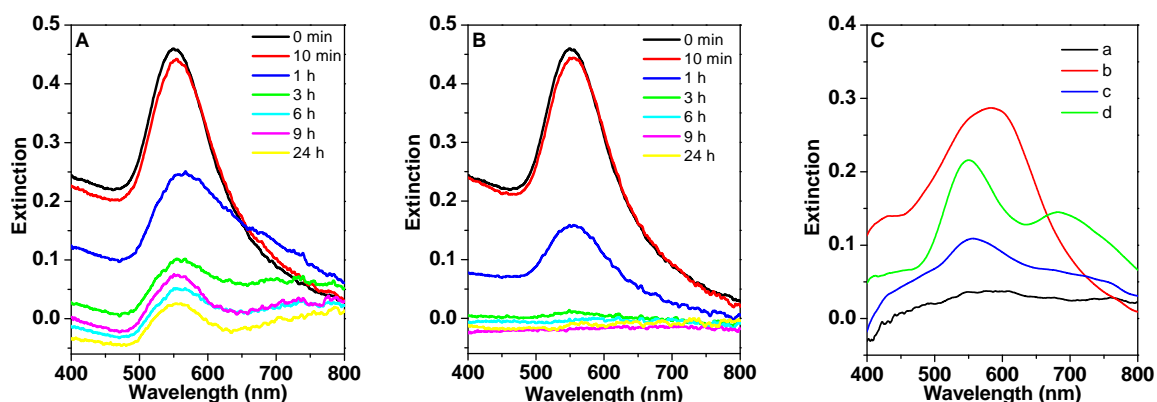


Figure A.6: (A and B) UV-Vis spectra of 80 nm AuNPs in 50 vol.% THF-water solutions at various times: (A) in the absence of PS beads, (B) in the presence of PS beads. (C) UV-vis spectra of AuNP-coated PS beads with different levels of metal coverage dispersed in DI water: (a) 30 nm AuNPs ( $n = \text{the ratio of the number of metal NPs to PS particles} = 1.3 \times 10^5$ ), (b) 30 nm AuNPs ( $n = 9.8 \times 10^5$ ), (c) 80 nm AuNPs ( $n = 1.0 \times 10^5$ ), (d) 80 nm AuNPs ( $n = 4.0 \times 10^5$ ) (The spectra measured from metal-coated PS beads were referenced to that of a plain PS bead.).

Bead shrinkage, induced by the removal of THF via water washing, resulted in a densification of the metal NP coating on the PS beads. The mechanism of deswelling and densification can alter significantly the morphology of NP assemblies on the PS beads. For example, a dendritic morphology of AuNPs was observed at the specific range of NP loading ( $0.7 \times 10^5 < n$  (the ratio of the number of metal NPs to PS particles)  $< 1.3 \times 10^5$ ), shown in Figure A.5c. Non-equilibrium dendritic patterns of metal NPs are known to form at flat interfaces under appropriate diffusion-controlled conditions [74-77]. NP dendrites have been observed to form in the presence of polymer stabilizers such as PVP, as well as small molecule promoters such as pyridine [74, 76]. Nonequilibrium dendritic structure formation is often observed to be sensitive to preparatory conditions, such as particle concentrations, which appears to be the case in the present study [75]. Under diffusion-limited aggregation, an optimum concentration is observed because high NP concentrations lead to particles being too closely compacted and low NP concentrations

supply insufficient numbers of NPs for building dendritic structures. The effect of substrate curvature on dendrite formation via diffusion-limited aggregation is not known. However, the large PS beads have relatively low curvature compared to the NPs and represent a close approximation to a flat surface.

The fraction of AuNPs should be useful as a parameter for adjusting surface coverage. Figure A.6c shows UV-vis spectra of 30 and 80 nm AuNP-coated PS beads with different NP concentrations dispersed in DI water. The plasmon resonance peak appeared around 560 nm at the lowest metal surface coverage for the 30 nm AuNP coated-PS beads (curve a of Figure A.6c). This peak was red-shifted by  $\sim 30$  nm, compared to that of the individual AuNPs dispersed in DI water. The red-shift of the peak can be related to (1) the change in the local dielectric of the surrounding medium that occurs after deposition of AuNPs on the PS bead surface and (2) interparticle plasmon field coupling resulting from densification of NPs on the PS surface [78]. The plasmon peak became further red-shifted to  $\sim 590$  nm and increased in intensity as NP concentration increased (curve b of Figure A.6c). This is due to increased interparticle plasmon field coupling associated with the increase of the metal coverage on the beads [78]. For the PS beads covered by 80 nm AuNPs, a single broad plasmon peak ( $\sim 555$  nm) was observed for the lowest NP concentration (curve c of Figure A.6c). However, another broad plasmon peak appeared at longer wavelengths ( $\sim 690$  nm) and increased in intensity with the higher NP fraction (curve d of Figure A.6c). The increase in intensity of the surface plasmon resonance peak at  $\sim 550$  nm, corresponding to isolated AuNPs, is due to increasing numbers of relatively isolated AuNPs on the bead surface. The appearance of an additional low energy resonance peak at 690 nm is attributed to the onset aggregation of AuNPs on the polymer bead with higher metal coverages. These results were consistent with SEM images and UV-vis microabsorption spectra of single beads, described below.



#### A.4.2. Optical Properties of Metal-Coated Polymer Beads

Figures A.7a-c show SEM and dark field optical microscope images of the 30 nm AuNP-coated PS beads at different metal coverages. Metal surface coverage increased (reaching a maximum total surface coverage of 89 %) as NP concentration increased, shown in Figure A.7c. Dark field images demonstrated that brightness increased as metal surface coverage increased (Figures A.7a-c). Detailed surface morphology of the metal coating on the bead was examined by AFM images. Overall, the metal coating was homogeneous and relatively smooth without any large clumps of NPs (Figure A.8a). AFM images also indicated that the 30 nm AuNP coating consisted of 1 to ~ 3 dense NP layers, shown in Figure A.8b.

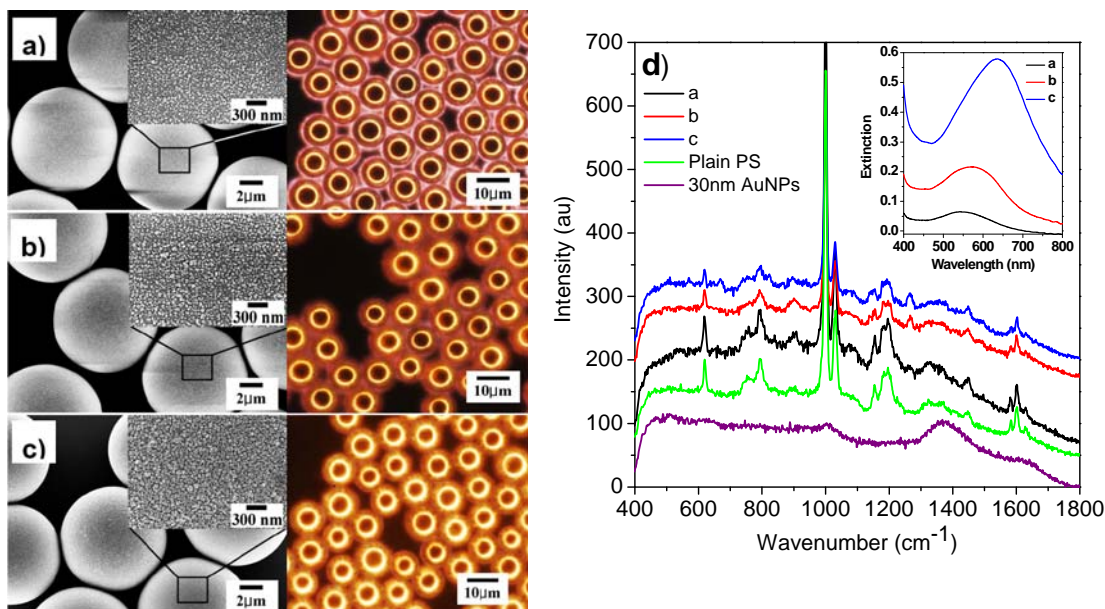


Figure A.7: SEM and dark field images (a-c) and Surface-enhanced Raman spectra (d) and the corresponding UV-vis spectra (d, inset) of 10 μm PS beads coated by 30 nm AuNPs with different levels of metal coverage: (a)  $n$  = the ratio of the number of metal NPs to PS particles =  $1.3 \times 10^5$ , (b)  $n = 2.5 \times 10^5$ , (c)  $n = 9.8 \times 10^5$ .

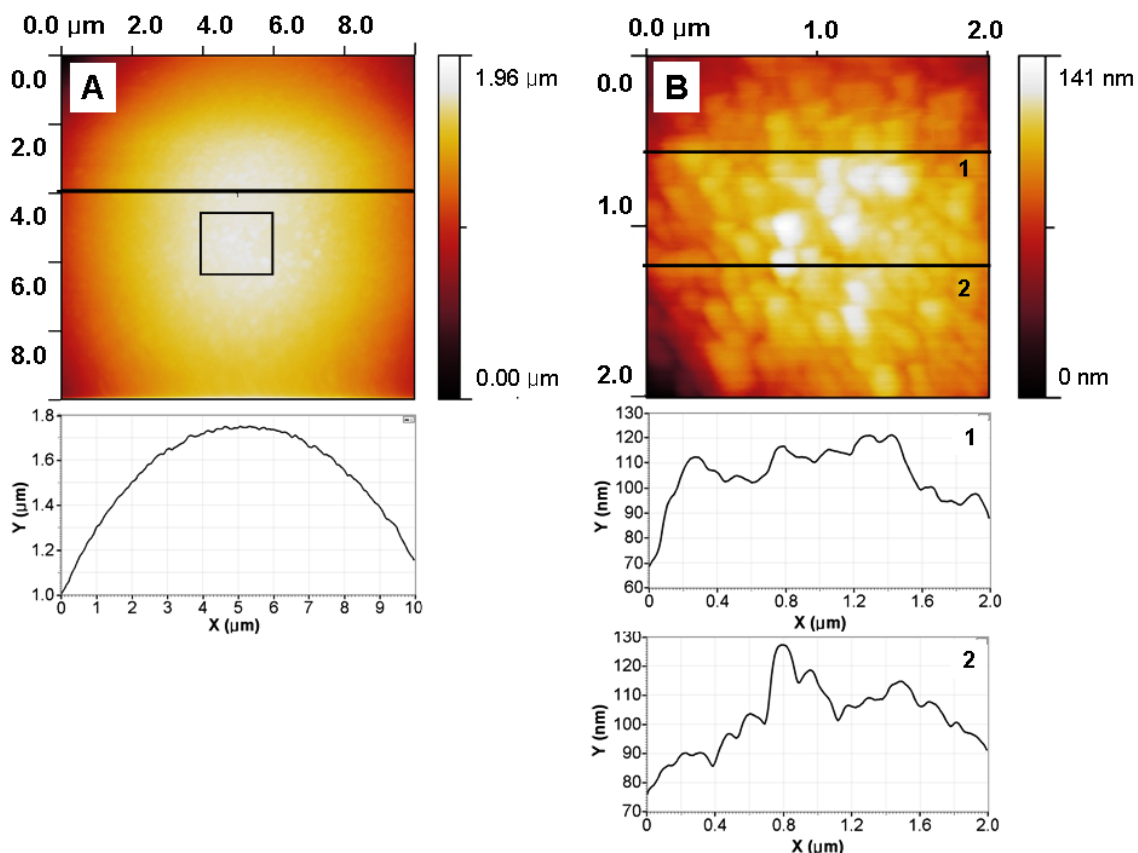


Figure A.8: AFM surface images (top) of a PS bead covered by 30 nm AuNPs (corresponding Figure A.7c) and line profiles along the line (bottom) on the AFM images: (a) a single bead ( $10 \times 10 \mu\text{m}^2$ ), (b) center area of a single bead ( $2 \times 2 \mu\text{m}^2$ ).

To characterize the optical properties of NP-coated PS beads, UV-vis spectra from single beads covered with 30 nm AuNPs were measured, shown in the inset of Figure A.7d. The plasmon resonance peak was red-shifted from 545 to 650 nm and significant increases in intensity and broadening of the plasmon resonance peak were observed as metal surface coverage increased (curves a-c of Figure A.7d, inset). The position, intensity, and broadening of the plasmon resonance of the metal NP assembly can be explained qualitatively by Mie scattering theory, which accounts for the dependence of the plasmon resonance on particle size and shape, the surrounding dielectric environment, and interparticle distance [78-82]. Closely packed metal NP assemblies have been achieved on planar [78, 80, 81, 83, 84] and spherical surfaces [18,

37, 38]. The overall plasmon resonance band of the highly packed metal NP assembly consists of concurrent individual and interparticle coupling plasmon resonance at long wavelength, which depends strongly on interparticle spacing [78, 80, 81]. Because of nonuniformity of interparticle separation distribution, a single broad resonance peak, resulting from a superimposition of both individual and interparticle collective surface plasmon resonance has been observed usually. The red-shift and increase in intensity of the plasmon peak is due predominantly to the interparticle collective resonance [78]. Hence, significant red-shifting and broadening of the surface plasmon resonance band with an increase of metal coverage on the PS bead surface is attributed to intensified interparticle coupling resonance due to AuNP crowding on the PS beads. This result is consistent with other work, where the red-shift of the plasmon peak position from 520 - 560 to 650 - 660 nm was observed as the AuNP density increased on planar surfaces [78, 81, 84]. As for AuNP assemblies on the spherical surface, a broad and red-shifted resonance at 660 nm was predicted for a nanoshell composed of 30 nm AuNPs by using a discrete dipole approximation model [37]. Other experimental works have shown that complete metal shells on PS beads showed a broad and red-shifted plasmon peak around 680 nm [18, 38]. The spectra (curve c of Figure A.7d, inset) of 30 nm Au coated beads with the highest coverage from this work showed a similar plasmon resonance wavelength as complete Au shells.

Figure A.7d shows the SERS spectra of 30 nm AuNPs and PS beads coated with different amounts of 30 nm AuNPs. For the AuNP-PS composite beads, all the expected Raman bands of PS appeared at 1014, 1210, and 633  $\text{cm}^{-1}$ , assigned to phenyl ring breathing and radial ring stretching modes. The bands at 1196 and 1170  $\text{cm}^{-1}$ , corresponding to CH in-plane bending modes [85], are less intense compared with those of plain PS beads, and their intensities were found to decrease as the amount of AuNP coating increased. This is due to a decrease in the exposed PS area, as the surface became more coated with metal. Since the NPs on the PS surface shield the surface from

the Raman laser, a minimal Raman band corresponding to the PS was detected when the surface was completely coated by NPs [35]. In contrast, the degree of enhancement in the vibration bands of the pyrrolidone ring of PVP increased as the metal coverage increased:  $571\text{ cm}^{-1}$  (C=O bending),  $667\text{ cm}^{-1}$  (N-C=O ring deformation),  $821\text{ cm}^{-1}$  (C-C bond vibration of the ring),  $895\text{ cm}^{-1}$  ( $\nu$ (C-C) ring breathing), and  $1265\text{ cm}^{-1}$  ( $\text{CH}_2$  ring wagging). The surface plasmon resonance field emanating from the metal NP assembly is responsible for the enhancement in PVP Raman signals, compared to the very weak Raman signal of bulk PVP [35, 86]. Raman signal intensities increase as the plasmon resonance intensity of the NPs at the Raman excitation wavelength increases, shown in Figure A.7d [79].

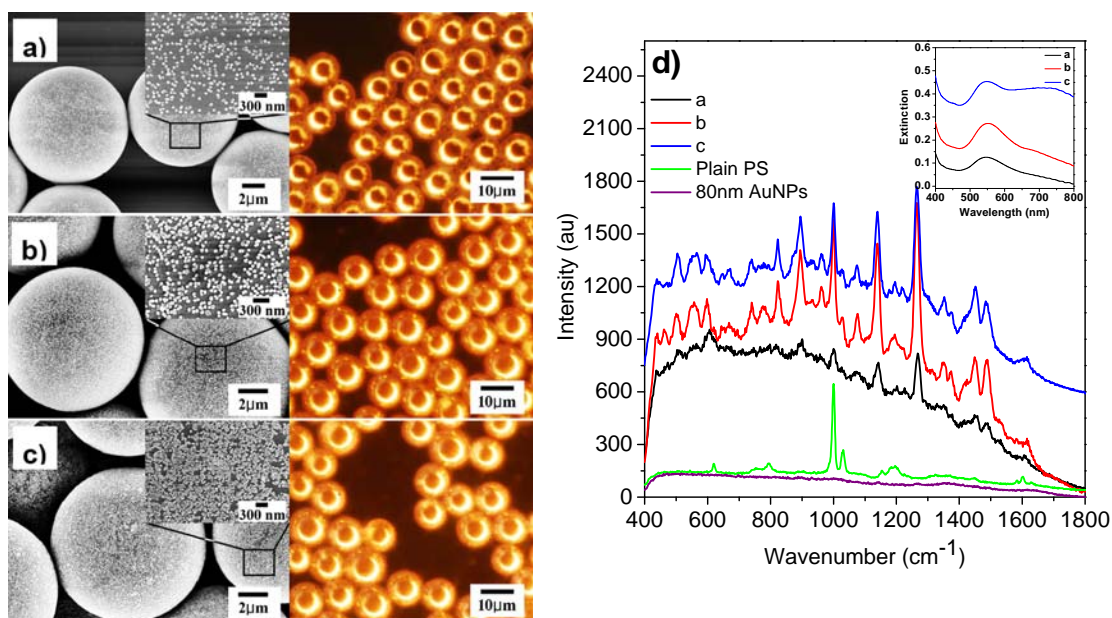


Figure A.9: SEM and dark field images (a-c) and Surface-enhanced Raman spectra (d) and the corresponding UV-vis spectra (d, inset) of  $10\text{ }\mu\text{m}$  PS beads coated by  $80\text{ nm}$  AuNPs with different levels of metal coverage: (a)  $n = 1.0 \times 10^5$ , (b)  $n = 2.0 \times 10^5$ , (c)  $n = 4.0 \times 10^5$ .

For the  $80\text{ nm}$  AuNP-coated PS beads, metal coverage on the bead was also proportional to the concentration of NPs used. From SEM images of  $80\text{ nm}$  AuNP-

coated PS beads, the surface coverage continued to increase from approximately 27 % to 63 % as AuNP concentration increased (Figures A.9a-c). At the lowest metal coverage, individual AuNPs were observed uniformly without any AuNP aggregation on the beads (Figure A.9a). As the metal coverage increased, interparticle distance decreased and AuNPs started to form aggregates on the surface, resulting an increase in surface roughness (Figure A.9b). The maximum number of AuNP aggregates on the PS beads, and the highest surface roughness, was observed at the highest metal coverage (Figure A.9c). Dark field images of the PS beads covered with 80 nm AuNPs were brighter than those of 30 nm AuNP-coated PS beads, in spite of lower metal coverage. This is due to the higher scattering power of the larger sized AuNPs. For all particle sizes, higher surface coverage resulted in brighter images in dark field microscopy.

A surface plasmon band with one peak around 545 nm was observed for the 80 nm AuNP-coated PS bead with the lowest metal coverage, illustrated in the inset of Figure A.9d (curve a). A strong and sharp extinction peak ( $\sim 545$  nm) is due to the plasmon resonance of individual AuNPs on the PS bead surface. At higher metal coverage, another broad peak appeared at longer wavelength around 680 nm, and it continued to become further intensified, broadened, and red-shifted to 740 nm (curves b and c of Figure A.9d, inset) as metal coverage increased. This low energy resonance peak is attributed to the interparticle coupling resonance which depends strongly on interparticle distance [78, 81]. Increasing metal coverage and the AuNP aggregation on the beads caused enhanced interparticle plasmon coupling and further red-shifting (from 680 to 740 nm), broadening, and intensification of the peak. On the other hand, the intensity of the individual plasmon peak ( $\sim 545$  nm) increased monotonically without red-shifting as the metal coverage increased. This result indicates the dominant effect of interparticle coupling resonance on the red-shift of the resonance band at higher metal density in the AuNP assembly [78]. UV-vis spectra were consistent with the morphology of the AuNP coating verified from SEM (Figures A.9a-c).

For slightly bigger nanoparticles ( $> 30$  nm), enhancement in the SERS spectra of PVP increases as the NP size increases, due to the increase of the surface plasmon field. Figure A.9d shows the SERS spectra of 80 nm AuNPs and PS beads coated with 80 nm AuNPs. As the large AuNPs scatter incident light away from the surface of PS, fewer photons are scattered from the surface of PS and less Raman photons corresponding to PS are generated as AuNP coverage increases. Therefore, most of the Raman bands corresponding to the PS disappeared or weakened. On the other hand, all Raman bands corresponding to the PVP are enhanced by the stronger plasmon field due to the increased metal coverage [35]. The composite bead with moderate metal coverage (Figure A.9b and curve b of Figure A.9d) showed more enhanced Raman signals than the bead with the lowest metal coverage (Figure A.9a and curve a of Figure A.9d), because the plasmon peak intensity of the denser metal coating is stronger at the excitation line (785 nm). Although the AuNP-coated bead with the highest metal coverage (curve c of Figure A.9d) has the strongest plasmon peak at the excitation frequency, the SERS bands are less intense than those of the moderate metal coverage (curve b of Figure A.9d). SEM images indicated the surface roughness of the metal-coated beads increased due to the formation of aggregates of AuNPs on the beads as the metal coverage increased. However, AuNP aggregates formed larger clusters on the bead surface at the highest metal coverage (Figure A.9c). Hence, a decrease in the intensity of SERS bands at the highest metal coverage might be due to destructive interference between the Raman photons generated in high aggregation areas [87].

Silver nanocubes (AgNCs) (60 nm, cube) were also successfully coated on the polymer beads using the CSH technique. Aqueous suspensions of the AgNC-coated beads exhibited various colors ranging from intense yellow, brown, and gray to black as the AgNC concentration increased. Figures A.10a-c show SEM and dark field images of the 60 nm AgNC-coated PS beads as a function of metal coverage.

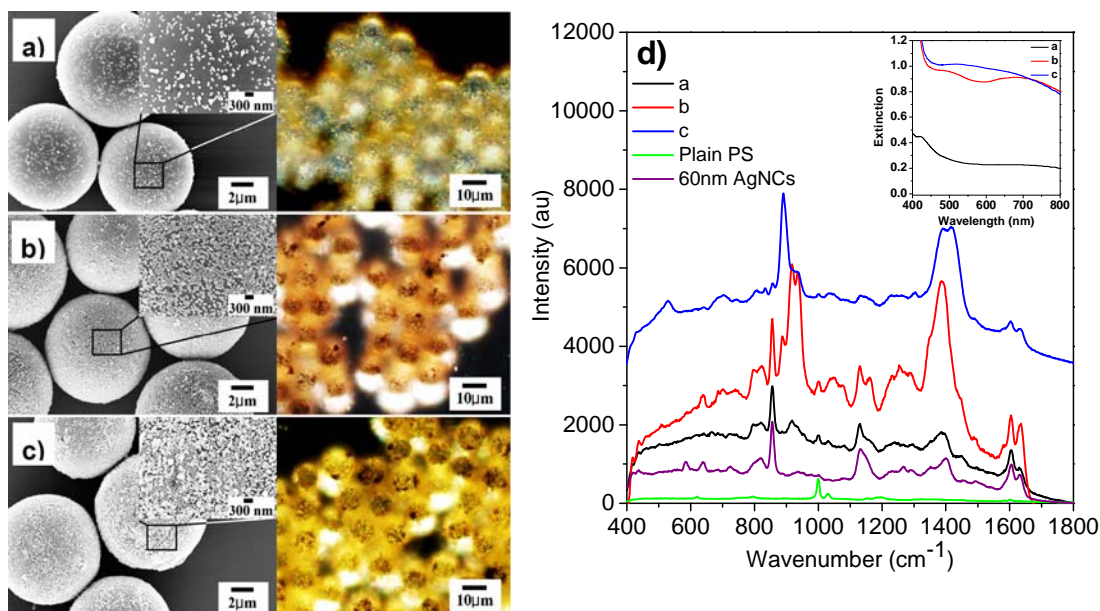


Figure A.10: SEM and dark field images (a-c) and Surface-enhanced Raman spectra (d) and the corresponding UV-vis spectra (d, inset) of 10  $\mu\text{m}$  PS beads coated by 60 nm AgNCs with different levels of metal coverage: (a)  $n = 1.0 \times 10^9$ , (b)  $n = 2.0 \times 10^9$ , (c)  $n = 3.5 \times 10^9$ .

Metal surface coverage ranged from 16 % to 82 % with some AgNC aggregations. Even with low surface coverage, bright images of AgNC-coated PS beads were observed in dark field microscopy due to the highly scattering nature of cubic AgNCs (Figure A.10a). Compared to the single AgNC plasmon bands that scatter blue light, the AgNC aggregate plasmon peak scatters red light [86]. Hence, as AgNC coverage on the beads increased, the amount of red light observed in the dark field image increased and the dominant scattered color changed from blue to red (Figures A.10a and 10b), indicating an increased number of aggregates. At the highest metal coverage, the dark field image of the composite beads showed yellow color (Figure A.10c), indicating a higher degree of aggregation into clusters that scatter yellow light. Corresponding SEM images (Figures A.10a-c) supported the results of dark field images well.



The morphology of the AgNC metal coatings corresponded well with single bead UV-vis microabsorption spectra. The plasmon resonance peak of the PS bead coated with 60 nm AgNCs appeared at about 420 nm (curve a of Figure A.10d, inset), which originates from individual plasmon resonance. For higher Ag coverage, the plasmon resonance peak became red-shifted to around 480 nm, with a broad peak at long wavelength ( $\sim 690$  nm) appearing (curve b of Figure A.10d, inset). A significant increase in the scattering intensity and the broadening of the plasmon resonance were observed at the highest metal coverage (curves c of Figure A.10d, inset), resulting in a single plasmon peak. The broadening, red-shifting, and development of long wavelengths of the plasmon spectrum with highly enhanced scattering is again explained by the intensified interparticle coupling effect due to crowded AgNCs and increased aggregation of AgNCs on the bead surface, shown in Figures A.10b and 10c.

Figure A.10d shows the SERS spectra of 60 nm AgNCs and AgNC-coated PS beads with different levels of metal coverage. The SERS bands of PVP in the case of pure AgNCs are more intense than spherical AuNPs. This could be due to a higher concentration of capping PVP molecules on the AgNCs as well as the more intense plasmon field of the Ag cubic shape relative to the spherical AuNPs. The degree of SERS enhancement of the bands corresponding to PVP of AgNC-coated beads with the lowest metal coverage is the smallest because the plasmon peak around the laser excitation line is weak (curve a of Figure A.10d). On the other hand, the composite bead with moderate Ag coverage has the highest SERS enhancement, because the gap distance decreases and the plasmon coupling between the particles becomes stronger (curve b of Figure A.10d). However, in the case of the highest surface coverage, a higher degree of aggregation into clusters with increased roughness was observed in the SEM and dark field images (Figure A.10c). Randomly arranged AgNC assemblies could cause destructive interference of Raman photons generated with different modes and, hence,



decrease the SERS intensity of the composite bead with the highest Ag coverage (curve c of Figure A.10d).

## A.5. CONCLUSIONS

In summary, noble metal (Au or Ag)-coated PS latex beads have been prepared by a solvent (THF)-controlled CSH technique. Different sizes (30, 60, and 80 nm), chemistries (Au and Ag), and shapes (sphere and cube) of NPs can be coated on commercially available, unfunctionalized PS beads, resulting in dense and uniform metal coatings on the beads. The resulting composite microspheres were stable and showed no loss of the metal coating during long-term (15 months) water storage.

THF appears to play two major roles in this technique: (1) as a solvent of PS, it plasticizes the PS surface during swelling, allowing entanglement with the PVP present on the metal NPs, and (2) as a non-solvent of PVP, it induces the heteroaggregation and adsorption of PVP-capped metal NPs on PS and allows control over the resulting morphology and surface coverage by driving instability of the NPs in the THF-water mixture.

To achieve a homogeneous metal coating, it was crucial to control the relative rate of homo- and heteroaggregation of particles by adjusting THF concentration, so that the PS beads and NPs heteroaggregate while avoiding their homoaggregation. The morphology and surface coverage of the metal coating on the beads, and thus the optical properties, were effectively controlled by adjusting the THF and NP concentrations as well as the NP chemistry, shape, and size. Continuous and close-packed metal coatings, with optical properties similar to complete shells, were obtained with smaller and spherical AuNPs. For the larger AuNPs or cubic AgNCs, less dense metal coatings were achieved, but they showed higher scattering properties due to the particles' inherent highly scattering nature.

The metal-coated beads were characterized as SERS substrates by using Raman spectroscopy. It was shown that the AgNC-coated polymer beads were the most effective SERS substrates, exhibiting highly enhanced Raman signals of PVP capping molecules. The resulting metal coated-polymer microspheres are of interest for applications in biomedical imaging, sensors, photonics, SERS, and electronics. In addition, the CSH technique is a facile and relatively benign single-step process.

#### **A.6. REFERENCES**

1. Lee, J.H., D.O. Kim, G.S. Song, Y. Lee, S.B. Jung, and J.D. Nam, *Macromol. Rapid Commun.*, 2007. **28**(5): p. 634-640.
2. Lee, J.H., J.S. Oh, P.C. Lee, D.O. Kim, Y. Lee, and J.D. Nam, *J. Electron. Mater.*, 2008. **37**(10): p. 1648-1652.
3. Kityk, I.V., J. Ebothe, I. Fuks-Janczarek, A.A. Umar, K. Kobayashi, M. Oyama, and B. Sahraoui, *Nanotechnology*, 2005. **16**(9): p. 1687-1692.
4. Kubo, S., Z.Z. Gu, D.A. Tryk, Y. Ohko, O. Sato, and A. Fujishima, *Langmuir*, 2002. **18**(13): p. 5043-5046.
5. Li, M.J., H. Zhang, J.H. Zhang, C.L. Wang, K. Han, and B. Yang, *J. Colloid Interface Sci.*, 2006. **300**(2): p. 564-568.
6. Rogach, A., A. Susa, F. Caruso, G. Sukhorukov, A. Kornowski, S. Kershaw, H. Mohwald, A. Eychmuller, and H. Weller, *Adv. Mater.*, 2000. **12**(5): p. 333-337.
7. Lee, T.M., A.L. Oldenburg, S. Sitafalwalla, D.L. Marks, W. Luo, F.J.J. Touban, K.S. Suslick, and S.A. Boppart, *Opt. Lett.*, 2003. **28**(17): p. 1546-1548.
8. West, J.L. and N.J. Halas, *Annu. Rev. Biomed. Eng.*, 2003. **5**: p. 285-292.
9. Hirsch, L.R., J.B. Jackson, A. Lee, N.J. Halas, and J. West, *Anal. Chem.*, 2003. **75**(10): p. 2377-2381.

10. Hirsch, L.R., R.J. Stafford, J.A. Bankson, S.R. Sershen, B. Rivera, R.E. Price, J.D. Hazle, N.J. Halas, and J.L. West, *Proc. Natl. Acad. Sci. U.S.A.*, 2003. **100**(23): p. 13549-13554.
11. Cao, Y.C., X.F. Hua, X.X. Zhu, Z. Wang, Z.L. Huang, Y.D. Zhao, H. Chen, and M.-X. Liu, *J. Immunol. Methods*, 2006. **317**: p. 163-170.
12. Han, M.Y., X.H. Gao, J.Z. Su, and S. Nie, *Nat. Biotechnol.*, 2001. **19**(7): p. 631-635.
13. Siiman, O., K. Gordon, A. Burshteyn, J.A. Maples, and J.K. Whitesell, *Cytometry*, 2000. **41**(4): p. 298-307.
14. Ishida, T., K. Kuroda, N. Kinoshita, W. Minagawa, and M. Haruta, *J. Colloid Interface Sci.*, 2008. **323**(1): p. 105-111.
15. Nath, S., S.K. Ghosh, S. Kundu, S. Praharaj, S. Panigrahi, S. Basu, and T. Pal, *Mater. Lett.*, 2005. **59**(29-30): p. 3986-3989.
16. Vo-Dinh, T., *Trac-Trends in Anal. Chem.*, 1998. **17**(8-9): p. 557-582.
17. Kelly, K.L., E. Coronado, L.L. Zhao, and G.C. Schatz, *J. Phys. Chem. B*, 2003. **107**(3): p. 668-677.
18. Ji, T.H., V.G. Lirtsman, Y. Avny, and D. Davidov, *Adv. Mater.*, 2001. **13**(16): p. 1253-1256.
19. Oldenburg, S.J., J.B. Jackson, S.L. Westcott, and N.J. Halas, *Appl. Phys. Lett.*, 1999. **75**(19): p. 2897-2899.
20. Siiman, O. and A. Burshteyn, *J. Phys. Chem. B*, 2000. **104**(42): p. 9795-9810.
21. Yguerabide, J. and E.E. Yguerabide, *Anal. Biochem.*, 1998. **262**(2): p. 137-156.
22. Bohmer, R.M. and N.J.C. King, *Cytometry*, 1984. **5**(5): p. 543-546.

23. Chen, J., F. Saeki, B.J. Wiley, H. Cang, M.J. Cobb, Z.Y. Li, L. Au, H. Zhang, M.B. Kimmey, X.D. Li, and Y. Xia, *Nano Lett.*, 2005. **5**(3): p. 473-477.
24. Festin, R., B. Bjorklund, and T.H. Totterman, *J. Immunol. Methods*, 1987. **101**(1): p. 23-28.
25. Huang, D., E.A. Swanson, C.P. Lin, J.S. Schuman, W.G. Stinson, W. Chang, M.R. Hee, T. Flotte, K. Gregory, C.A. Puliafito, and J.G. Fujimoto, *Science*, 1991. **254**(5035): p. 1178-1181.
26. Siiman, O., A. Jitianu, M. Bele, P. Grom, and E. Matijevic, *J. Colloid Interface Sci.*, 2007. **309**(1): p. 8-20.
27. Wang, R.K. and J.B. Elder, *Lasers Surg. Med.*, 2002. **30**(3): p. 201-208.
28. Barnickel, P. and A. Wokaun, *Mol. Phys.*, 1989. **67**(6): p. 1355-1372.
29. Mayer, A.B.R., W. Grebner, and R. Wannemacher, *J. Phys. Chem. B*, 2000. **104**(31): p. 7278-7285.
30. Michaels, A.M., M. Nirmal, and L.E. Brus, *J. Am. Chem. Soc.*, 1999. **121**(43): p. 9932-9939.
31. McLaughlin, C., D. Graham, and W.E. Smith, *J. Phys. Chem. B*, 2002. **106**(21): p. 5408-5412.
32. Nikoobakht, B., J.P. Wang, and M.A. El-Sayed, *Chem. Phys. Lett.*, 2002. **366**(1-2): p. 17-23.
33. Siiman, O., A. Lepp, and M. Kerker, *Chem. Phys. Lett.*, 1983. **100**(2): p. 163-168.
34. Tsai, D.P., J. Kovacs, Z.H. Wang, M. Moskovits, V.M. Shalae, J.S. Suh, and R. Botet, *Phys. Rev. Lett.*, 1994. **72**(26): p. 4149-4152.
35. Kim, K., H.B. Lee, H.K. Park, and K.S. Shin, *J. Colloid Interface Sci.*, 2008. **318**(2): p. 195-201.

36. Ou, J.L., C.P. Chang, Y. Sung, K.L. Ou, C.C. Tseng, H.W. Ling, and M.D. Ger, *Colloids Surf. A*, 2007. **305**(1-3): p. 36-41.
37. Peceros, K.E., X.D. Xu, S.R. Bulcock, and M.B. Cortie, *J. Phys. Chem. B*, 2005. **109**(46): p. 21516-21520.
38. Zhang, J.H., J.B. Liu, S.Z. Wang, P. Zhan, Z.L. Wang, and N.B. Ming, *Adv. Funct. Mater.*, 2004. **14**(11): p. 1089-1096.
39. Chen, C.W., M.Q. Chen, T. Serizawa, and M. Akashi, *Chem. Commun.*, 1998(7): p. 831-832.
40. Chen, C.W., T. Serizawa, and M. Akashi, *Chem. Mater.*, 1999. **11**(5): p. 1381-1389.
41. Jana, S., S.K. Ghosh, S. Nath, S. Pande, S. Praharaj, S. Panigrahi, S. Basu, T. Endo, and T. Pal, *Appl. Catal. A*, 2006. **313**(1): p. 41-48.
42. Jana, S., S. Pande, S. Panigrahi, S. Praharaj, S. Basu, A. Pal, and T. Pal, *Langmuir*, 2006. **22**(16): p. 7091-7095.
43. Li, S.N., X.L. Yang, and W.Q. Huang, *Macromol. Chem. Phys.*, 2005. **206**(19): p. 1967-1972.
44. Liu, W., X.L. Yang, and L. Xie, *J. Colloid Interface Sci.*, 2007. **313**(2): p. 494-502.
45. Tamai, H., H. Sakurai, Y. Hirota, F. Nishiyama, and H. Yasuda, *J. Appl. Polym. Sci.*, 1995. **56**(4): p. 441-449.
46. Liu, W., X.L. Yang, and W.Q. Huang, *J. Colloid Interface Sci.*, 2006. **304**(1): p. 160-165.
47. Dokoutchaev, A., J.T. James, S.C. Koene, S. Pathak, G.K.S. Prakash, and M.E. Thompson, *Chem. Mater.*, 1999. **11**(9): p. 2389-2399.
48. Phadtare, S., A. Kumar, V.P. Vinod, C. Dash, D.V. Palaskar, M. Rao, P.G. Shukla, S. Sivaram, and M. Sastry, *Chem. Mater.*, 2003. **15**(10): p. 1944-1949.

49. Shi, W.L., Y. Sahoo, and M.T. Swihart, *Colloids Surf. A*, 2004. **246**(1-3): p. 109-113.
50. Westcott, S.L., S.J. Oldenburg, T.R. Lee, and N.J. Halas, *Langmuir*, 1998. **14**(19): p. 5396-5401.
51. Kaltenpoth, G., M. Himmelhaus, L. Slansky, F. Caruso, and M. Grunze, *Adv. Mater.*, 2003. **15**(13): p. 1113-1118.
52. Shi, W.L., Y. Sahoo, M.T. Swihart, and P.N. Prasad, *Langmuir*, 2005. **21**(4): p. 1610-1617.
53. Yong, K.T., Y. Sahoo, M.T. Swihart, and P.N. Prasad, *Colloids Surf. A*, 2006. **290**(1-3): p. 89-105.
54. Gittins, D.I., A.S. Sussha, B. Schoeler, and F. Caruso, *Adv. Mater.*, 2002. **14**(7): p. 508-512.
55. Cassagneau, T. and F. Caruso, *Adv. Mater.*, 2002. **14**(10): p. 732-736.
56. Kato, N. and F. Caruso, *J. Phys. Chem. B*, 2005. **109**(42): p. 19604-19612.
57. Liang, Z.J., A. Sussha, and F. Caruso, *Chem. Mater.*, 2003. **15**(16): p. 3176-3183.
58. Liang, Z.J., A.S. Sussha, and F. Caruso, *Adv. Mater.*, 2002. **14**(16): p. 1160-1164.
59. Furusawa, K. and O.D. Velev, *Colloids Surf. A*, 1999. **159**(2-3): p. 359-371.
60. Radtchenko, I.L., G.B. Sukhorukov, N. Gaponik, A. Kornowski, A.L. Rogach, and H. Mohwald, *Adv. Mater.*, 2001. **13**(22): p. 1684-1687.
61. Lee, J.H., M.A. Mahmoud, V. Sitterle, J. Sitterle, and J.C. Meredith, *J. Am. Chem. Soc.*, 2009. **131**(14): p. 5048-5049.
62. Lee, J.H., M.A. Mahmoud, V.B. Sitterle, J.J. Sitterle, and J.C. Meredith, *Chem. Mater.*, 2009. **21**(23): p. 5654-5663.

63. Freund, P.L. and M. Spiro, J. Phys. Chem., 1985. **89**(7): p. 1074-1077.
64. Mahmoud, M.A. and M.A. El-Sayed, J. Phys. Chem. C, 2008. **112**(37): p. 14618-14625.
65. Bukowska, A., W. Bukowski, and J. Noworol, J. Appl. Polym. Sci., 2007. **106**(6): p. 3800-3807.
66. Kim, A.J., V.N. Manoharan, and J.C. Crocker, J. Am. Chem. Soc., 2005. **127**(6): p. 1592-1593.
67. Caruso, F., Adv. Mater., 2001. **13**(1): p. 11-22.
68. Lazarides, A.A., K.L. Kelly, T.R. Jensen, and G.C. Schatz, J. Mol. Struct.-Theochem, 2000. **529**: p. 59-63.
69. Lazarides, A.A. and G.C. Schatz, J. Phys. Chem. B, 2000. **104**(3): p. 460-467.
70. Graf, C., D.L.J. Vossen, A. Imhof, and A. van Blaaderen, Langmuir, 2003. **19**(17): p. 6693-6700.
71. Qian, W.X., R.B. Xing, X.H. Yu, X.J. Quan, and Y.C. Han, J. Chem. Phys., 2007. **126**(6): p. 064901.
72. Smith, J.N., J. Meadows, and P.A. Williams, Langmuir, 1996. **12**(16): p. 3773-3778.
73. Wang, G.H. and P.S. Nicholson, J. Am. Ceram. Soc., 2001. **84**(6): p. 1250-1256.
74. Agrawal, V.V., G.U. Kulkarni, and C.N.R. Rao, J. Colloid Interface Sci., 2008. **318**: p. 501-506.
75. Corno, J.A., J. Stout, R. Yang, and J.L. Gole, J. Phys. Chem. C, 2008. **112**: p. 5439-5446.
76. Jin, Y.D. and S.J. Dong, Angew. Chem. Int. Ed., 2002. **41**(6): p. 1040-1044.

- 77. Sander, L.M., *Nature*, 1986. **322**(6082): p. 789-793.
- 78. Jiang, C.Y., S. Markutsya, and V.V. Tsukruk, *Langmuir*, 2004. **20**(3): p. 882-890.
- 79. Averitt, R.D., D. Sarkar, and N.J. Halas, *Phys. Rev. Lett.*, 1997. **78**(22): p. 4217-4220.
- 80. Jiang, G.Q., A. Baba, H. Ikarashi, R.S. Xu, J. Locklin, K.R. Kashif, K. Shinbo, K. Kato, F. Kaneko, and R. Advincula, *J. Phys. Chem. C*, 2007. **111**(50): p. 18687-18694.
- 81. Malikova, N., I. Pastoriza-Santos, M. Schierhorn, N.A. Kotov, and L.M. Liz-Marzan, *Langmuir*, 2002. **18**(9): p. 3694-3697.
- 82. Mie, G., *Ann. Phys.*, 1908. **25**(3): p. 377-445.
- 83. Bhat, R.R., J. Genzer, B.N. Chaney, H.W. Sugg, and A. Liebmman-Vinson, *Nanotechnology*, 2003. **14**(10): p. 1145-1152.
- 84. Bhat, R.R., M.R. Tomlinson, and J. Genzer, *Macromol. Rapid Commun.*, 2004. **25**(1): p. 270-274.
- 85. Compagnini, G., B. Pignataro, and B. Pelligra, *Chem. Phys. Lett.*, 1997. **272**(5-6): p. 453-458.
- 86. Mahmoud, M.A., C.E. Tabor, and M.A. El-Sayed, *J. Phys. Chem. C*, 2009. **113**(14): p. 5493-5501.
- 87. Kim, K., H.S. Lee, and N.H. Kim, *Anal. Bioanal. Chem.*, 2007. **388**(1): p. 81-88.